

# On satellite observations of atmospheric composition and their interpretation

**Citation for published version (APA):**

Dirksen, R. J. (2011). *On satellite observations of atmospheric composition and their interpretation*. [Phd Thesis 2 (Research NOT TU/e / Graduation TU/e), Applied Physics and Science Education]. Technische Universiteit Eindhoven. <https://doi.org/10.6100/IR695334>

**DOI:**

[10.6100/IR695334](https://doi.org/10.6100/IR695334)

**Document status and date:**

Published: 01/01/2011

**Document Version:**

Publisher's PDF, also known as Version of Record (includes final page, issue and volume numbers)

**Please check the document version of this publication:**

- A submitted manuscript is the version of the article upon submission and before peer-review. There can be important differences between the submitted version and the official published version of record. People interested in the research are advised to contact the author for the final version of the publication, or visit the DOI to the publisher's website.
- The final author version and the galley proof are versions of the publication after peer review.
- The final published version features the final layout of the paper including the volume, issue and page numbers.

[Link to publication](#)

**General rights**

Copyright and moral rights for the publications made accessible in the public portal are retained by the authors and/or other copyright owners and it is a condition of accessing publications that users recognise and abide by the legal requirements associated with these rights.

- Users may download and print one copy of any publication from the public portal for the purpose of private study or research.
- You may not further distribute the material or use it for any profit-making activity or commercial gain
- You may freely distribute the URL identifying the publication in the public portal.

If the publication is distributed under the terms of Article 25fa of the Dutch Copyright Act, indicated by the "Taverne" license above, please follow below link for the End User Agreement:

[www.tue.nl/taverne](http://www.tue.nl/taverne)

**Take down policy**

If you believe that this document breaches copyright please contact us at:

[openaccess@tue.nl](mailto:openaccess@tue.nl)

providing details and we will investigate your claim.

# On satellite observations of atmospheric composition and their interpretation

Copyright ©2011 R.J. Dirksen  
Cover illustration by the author  
Cover design by Paul Verspaget  
Printed by Universiteitsdrukkerij TU Eindhoven, Eindhoven, The Netherlands

A catalogue record is available from the Eindhoven University of Technology Library

Dirksen, Ruud

OMI observations of atmospheric composition /  
by Ruud Dirksen. - Eindhoven: Technische Universiteit Eindhoven, 2011.  
-Proefschrift.  
ISBN: 978-90-386-2438-9  
NUR: 924

Trefwoorden: aerosolen / atmosferische chemie / atmosferische dynamica / satelliet-  
metingen / stikstofdioxide  
Subject headings: aerosols / atmospheric chemistry / atmospheric dynamics / nitro-  
gen dioxide / satellite observations

# On satellite observations of atmospheric composition and their interpretation

## PROEFSCHRIFT

ter verkrijging van de graad van doctor  
aan de Technische Universiteit Eindhoven,  
op gezag van de rector magnificus, prof.dr.ir. C.J. van Duijn,  
voor een commissie aangewezen door het College voor Promoties  
in het openbaar te verdedigen op  
maandag 28 februari 2011 om 16.00 uur

door

**Rudi Jeroen Dirksen**

geboren te Zaandam

Dit proefschrift is goedgekeurd door de promotoren:

prof.dr. H.M. Kelder

en

prof.dr. P.F. Levelt

Copromotor:

dr. K.F. Boersma

*Thank goodness for the atmosphere.*

Bill Bryson - A short history of nearly everything

Cover:

OMI observations of the around-the-world transport of an aerosol plume emitted by forest fires in southeastern Australia on 14 December 2006. The OMI Absorbing Aerosol Index observations are plotted on a MODIS monthly global image that is available at [http://earthobservatory.nasa.gov/Features/BlueMarble/BlueMarble\\_monthlies.php](http://earthobservatory.nasa.gov/Features/BlueMarble/BlueMarble_monthlies.php). The numbers represent the day of the observation (in December 2006).

# Contents

<b>1</b>	<b>Introduction</b>	<b>1</b>
1.1	OMI observations of atmospheric constituents . . . . .	1
1.2	NO <sub>2</sub> in the troposphere . . . . .	2
1.3	NO <sub>2</sub> in the stratosphere . . . . .	4
1.4	Forest fire aerosols . . . . .	5
1.5	OMI retrievals . . . . .	6
1.5.1	OMI retrieval of NO <sub>2</sub> . . . . .	6
1.5.2	OMI Absorbing Aerosol Index . . . . .	6
1.6	Aim and outline of this thesis . . . . .	7
<b>2</b>	<b>OMI spectral slitfunction</b>	<b>9</b>
2.1	Introduction . . . . .	9
2.2	The Ozone Monitoring Instrument (OMI) . . . . .	11
2.3	ITF characterization measurements and results . . . . .	12
2.3.1	Echelle grating ITF characterization setup and measurements	12
2.4	Echelle grating instrument transfer function results . . . . .	20
2.5	Conclusions . . . . .	28
<b>3</b>	<b>Dutch OMI NO<sub>2</sub> (DOMINO)</b>	<b>31</b>
3.1	Introduction . . . . .	31
3.2	Satellite retrieval of tropospheric NO <sub>2</sub> . . . . .	32
3.2.1	OMI data streams . . . . .	33
3.2.2	OMI slant column retrieval . . . . .	33
3.2.3	Stratosphere-troposphere separation . . . . .	34
3.2.4	Tropospheric air mass factor . . . . .	37
3.2.5	Features of the DOMINO product . . . . .	38
3.3	OMI data collection 3 . . . . .	39
3.4	OMI standard product . . . . .	40
3.5	Illustration of DOMINO tropospheric NO <sub>2</sub> monitoring capabilities	42
3.6	Recommendations from validation studies . . . . .	43
3.6.1	Results . . . . .	44
3.7	Summary . . . . .	46

<b>4</b>	<b>OMI stratospheric NO<sub>2</sub></b>	<b>49</b>
4.1	Introduction . . . . .	50
4.2	OMI stratospheric NO <sub>2</sub> data . . . . .	52
4.2.1	OMI . . . . .	52
4.2.2	Dutch OMI NO <sub>2</sub> (DOMINO) retrieval . . . . .	52
4.2.3	NASA GSFC (Standard product) retrieval . . . . .	59
4.3	Data sets . . . . .	61
4.3.1	SAOZ . . . . .	61
4.3.2	NDACC UV-Vis zenith sky data . . . . .	62
4.3.3	Ground-based FTIR stations . . . . .	62
4.4	Evaluation of OMI stratospheric NO <sub>2</sub> . . . . .	63
4.4.1	Evaluation of ground-based techniques . . . . .	63
4.4.2	Evaluation of OMI stratospheric NO <sub>2</sub> with ground-based measurements . . . . .	66
4.5	Detailed comparison of stratospheric NO <sub>2</sub> from DOMINO and SP . . . . .	66
4.6	Day-to-day dynamical effects . . . . .	69
4.7	OMI observations of the diurnal variation of stratospheric NO <sub>2</sub> . . . . .	73
4.8	OMI observed trends stratospheric NO <sub>2</sub> . . . . .	77
4.8.1	Seasonal variation and QBO . . . . .	77
4.8.2	Long-term trends in stratospheric NO <sub>2</sub> . . . . .	82
4.9	Summary and Conclusions . . . . .	84
<b>5</b>	<b>Aerosol boomerang</b>	<b>87</b>
5.1	Introduction . . . . .	88
5.2	Satellite observations and Transport Model . . . . .	90
5.2.1	OMI . . . . .	90
5.2.2	OMI AAI . . . . .	90
5.2.3	OMI RGB images . . . . .	91
5.2.4	OMI O <sub>2</sub> -O <sub>2</sub> data products . . . . .	91
5.2.5	CALIOP/CALIPSO . . . . .	92
5.2.6	TM4 . . . . .	92
5.3	Origin and Vertical Transport of the Australian Biomass Burning Event . . . . .	93
5.4	Evaluation of OMI O <sub>2</sub> -O <sub>2</sub> pressures for aerosol vertical distribution . . . . .	96
5.4.1	Comparison with CALIOP results . . . . .	96
5.4.2	Radiative transfer results . . . . .	98
5.5	Injection Height and Long-Range Transport of the Australian Biomass Burning Event . . . . .	101
5.6	Conclusions and Outlook . . . . .	105



*Contents*

<b>6</b>	<b>Summary and outlook</b>	<b>109</b>
6.1	Overview . . . . .	109
6.2	Outlook . . . . .	111
	<b>Bibliography</b>	<b>113</b>
	<b>Summary</b>	<b>129</b>
	<b>List of publications</b>	<b>131</b>
	<b>Nawoord</b>	<b>133</b>
	<b>Curriculum vitae</b>	<b>135</b>

## Introduction

### 1.1 OMI observations of atmospheric constituents

The main scope of this thesis concerns measurements of the NO<sub>2</sub> and aerosol distribution from space by the Ozone Monitoring Instrument (OMI), and how we can interpret these observations in terms of atmospheric chemistry and transport. This thesis is based on my 10-year involvement with OMI starting with the performance testing and calibration of the instrument, the latter being essential to the retrieval of high quality data from OMI measurements. I continued with work on OMI flight data with a focus on nitrogen dioxide (NO<sub>2</sub>), taking care of the maintenance, off-line reprocessing and the near real time (NRT) service of the DOMINO (Dutch OMI NO<sub>2</sub>) product [see *Boersma et al.* [2007] and the DOMINO product specification document (PSD) that is available at [http://www.temis.nl/docs/OMI\\_NO2\\_HE5\\_1.0.2.pdf](http://www.temis.nl/docs/OMI_NO2_HE5_1.0.2.pdf)].

NO<sub>2</sub> plays an important role in the chemistry of the atmosphere; therefore detecting NO<sub>2</sub> from space is crucial to understand its global distribution and monitoring trends in its sources. NO<sub>2</sub> is one of the main data products of the OMI mission, whose purpose it is to monitor atmospheric constituents that are relevant to atmospheric chemistry, air quality and climate change [*Levelt et al.*, 2006a]. Doing so, OMI extends the data record of global observations of relevant trace species in the troposphere and stratosphere that was started in 1978 by the Total Ozone Mapping Spectrometer (TOMS) [*McPeters et al.*, 1998], and followed upon by the Global Ozone Monitoring Experiment (GOME) [*Burrows et al.*, 1999] and its successor SCIAMACHY in 2002 [*Bovensmann et al.*, 1999]. Owing to its high spatial resolution (24x13km<sup>2</sup> at nadir) and wide swath (2600 km), OMI allows for global daily monitoring of sources of tropospheric NO<sub>2</sub> on a near-urban scale [*Wang et al.*, 2007, *Boersma et al.*, 2009].

OMI is part of the scientific payload of NASA's EOS-AURA satellite that was launched in July 2004 into a sun-synchronous orbit at 705 km altitude with a local equator crossing time of 13h40m in the ascending node. Atmospheric columns of NO<sub>2</sub>, together with ozone [*Veeffkind et al.*, 2006], BrO [*Kurosu et al.*, 2004], OClO,

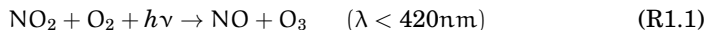
HCHO [Kurosu *et al.*, 2004], SO<sub>2</sub> [Krotkov *et al.*, 2006], and CHO-CHO [Kurosu *et al.*, 2005, Wittrock *et al.*, 2006], as well as clouds [Acarreta *et al.*, 2004], aerosols [Torres *et al.*, 2007] and the surface albedo [Kleipool *et al.*, 2008] are derived from the Earth reflectance spectrum that is recorded by OMI between 270-500 nm at an average spectral resolution of 0.5 nm and a spatial resolution of 24x13 km<sup>2</sup> at nadir.

The DOMINO tropospheric NO<sub>2</sub> data product is widely used within the scientific and air quality community. Examples of DOMINO data in air quality applications are the EU-funded GMES (Global Monitoring for Environment and Security) MACC (Monitoring Atmospheric Composition and Climate) project (see <http://www.gmes-atmosphere.eu/services/gac/reanalysis/>) and the use of NRT data by the THOR air quality forecast model (<http://thor.dmu.dk>, Hvidberg and Brandt [2009]). Scientific studies using DOMINO tropospheric NO<sub>2</sub> columns have detected the emissions of new power plants in Mongolia [Zhang *et al.*, 2009], the reduced NO<sub>x</sub> (NO + NO<sub>2</sub>) emissions in the Gulf of Mexico in the aftermath of hurricane Katrina [Yoshida *et al.*, 2010], and the reduction of NO<sub>x</sub> emissions resulting from the traffic ban during the Sino-African summit in November 2006 [Wang *et al.*, 2007].

## 1.2 NO<sub>2</sub> in the troposphere

Tropospheric NO<sub>x</sub> is a precursor of ozone, which directly links NO<sub>2</sub> to air quality and climate change. High concentrations of tropospheric ozone are toxic, having a detrimental effect on human health and crops [The Royal Society, 2008]. On the other hand, ozone increases the oxidizing power of the atmosphere by being the primary source of the hydroxyl radical (OH), which breaks down most atmospheric pollutants as well as several greenhouse gases [The Royal Society, 2008]. Furthermore, in the free troposphere ozone is an important greenhouse gas because of its strong absorption in the atmospheric window at 9.6 μm [Fishman *et al.*, 1979]. The contribution of tropospheric ozone to the anthropogenic radiative forcing (RF) relative to the year 1750 is considerably less certain and less well understood than those of carbon dioxide (CO<sub>2</sub>) and methane (CH<sub>4</sub>). Estimates of the RF of tropospheric ozone range from +0.25 to +0.65 W/m<sup>2</sup>, and it is currently assessed at +0.35 W/m<sup>2</sup> [IPCC, 2007].

The main reaction to produce tropospheric ozone is through the photolysis of NO<sub>2</sub>

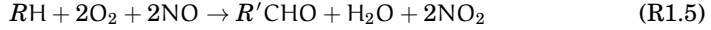
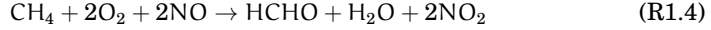
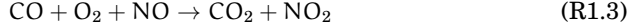


However, this production is counteracted by the destruction of ozone by NO



which leads to a dynamic equilibrium that determines the NO<sub>2</sub>/NO partitioning, but without a net production of ozone. In the presence of CO, methane or nonmethane

hydrocarbons (NMHC, abbreviated in R1.5 as  $R$ ), NO is converted into NO<sub>2</sub> via an alternative pathway, without destroying ozone.



Where  $R'$  denotes an organic fragment having one fewer carbon atom than  $R$ . In this case NO<sub>x</sub> acts as a catalyst for the production of ozone from the chemical fuel provided by CO, CH<sub>4</sub> or NMHC. In the free troposphere, ozone is produced from the ubiquitous CO and CH<sub>4</sub> [Crutzen, 1973], but in polluted areas the ozone production is dominated by NMHCs via the photochemical mechanism that was proposed by Haagen-Smit and Fox [1954].

Tropospheric NO<sub>x</sub> is produced by natural (e.g., lightning and forest fires) and anthropogenic (combustion of fossil fuels and biomass burning) sources. Based on model simulations, Jacob *et al.* [1999] predicted that the growing anthropogenic emissions in eastern Asia would lead to an increase of tropospheric ozone in the USA, which was confirmed with observations by Zhang *et al.* [2008] and Cooper *et al.* [2010].

The lifetime of tropospheric NO<sub>x</sub> and its atmospheric reservoirs ranges from less than one day in the boundary layer to several days in the upper troposphere, where it is less prone to scavenging and sedimentation [Brasseur *et al.*, 1999]. The major sink for NO<sub>x</sub> in the troposphere is conversion to HNO<sub>3</sub>, via R1.6, which due to its high solubility is readily scavenged by water droplets and aerosols, and subsequently removed by deposition.

In the presence of ammonia (NH<sub>3</sub>), HNO<sub>3</sub> reacts to form nitrate aerosol, which contributes significantly to the aerosol budget for northern Europe [Schaap *et al.*, 2002]. This links tropospheric NO<sub>x</sub> to aerosol formation via R1.6 and R1.7, which is particularly relevant for the Netherlands due to the high ammonia emissions from cattle breeding and agricultural practices.



Except for the urban atmosphere, NO<sub>x</sub> is the rate limiting factor in the production of tropospheric ozone [Brasseur *et al.*, 1999], which underlines the importance of accurate estimates of NO<sub>x</sub> emissions and distribution for the ozone budget. Due to the eminent suitability of satellite observations to monitor the global distribution of NO<sub>2</sub>, and estimating changes in emissions of NO<sub>x</sub>, these make a valuable contribution to assessing the ozone budget.

### 1.3 NO<sub>2</sub> in the stratosphere

NO<sub>2</sub> has a dual role in the processes that govern the destruction of stratospheric ozone. On the one hand, NO<sub>x</sub> catalytically destroys ozone, following the reaction cycle discovered by *Crutzen* [1970].



On the other hand, NO<sub>x</sub> suppresses ozone depletion by sequestering reactive chlorine and hydrogen species in unreactive gas phase reservoirs such as ClONO<sub>2</sub> and HNO<sub>3</sub>. Chlorine destroys ozone in a similar way as NO<sub>x</sub>, with Cl and ClO (ClO<sub>x</sub>) taking the place of NO, respectively NO<sub>2</sub>, in R1.2 and R1.8 [*Molina and Rowland*, 1974, *Stolarski and Cicerone*, 1974]. When temperatures inside the polar vortex drop below 197 K during the polar night, the formation of polar stratospheric clouds (PSCs) is possible. Heterogeneous reactions on the surface of these PSCs convert the HCl and ClONO<sub>2</sub> reservoirs into Cl<sub>2</sub> and HOCl, a process known as chlorine activation. With the return of sunlight in spring, the activated chlorine readily photolyzes to form ClO<sub>x</sub>, which efficiently destroys ozone according to the mechanism described by *Molina and Molina* [1987] and by the coupling of chlorine with bromine chemistry [*Solomon* [1999] and references therein]. Due to denitrification by the trapping (freezing) and subsequent sedimentation of the HNO<sub>3</sub> that is formed in the activation reactions, little NO<sub>x</sub> remains available to return active chlorine and bromine to a less reactive reservoir [e.g., *Brasseur et al.* [1999]].

In view of the above described effect of NO<sub>x</sub> on stratospheric ozone, monitoring of stratospheric NO<sub>2</sub> concentrations provides important support to monitoring of the ozone layer. The main source of stratospheric NO<sub>x</sub> is oxidation of nitrous oxide (N<sub>2</sub>O) in the middle stratosphere [e.g., *Wayne* [2000] and references therein]. N<sub>2</sub>O is emitted at the surface by natural and anthropogenic sources, and it enters the stratosphere in the tropics from where it is transported poleward by the Brewer-Dobson circulation. The timescale of the chemical conversion of N<sub>2</sub>O into NO<sub>x</sub> is comparable or slower than the timescale of its transport, so that the concentration of N<sub>2</sub>O decreases, and the NO<sub>2</sub> concentration increases, from equator to the pole.

Because of its indirect effect on the stratospheric ozone layer, *Ravishankara et al.* [2009] proposed N<sub>2</sub>O as an ozone depleting substance (ODS), with an ozone depleting potential (ODP) of 0.017. ODP is a measure of the destructive potential of a particular substance relative to depletion caused by an equal amount of CFC-11 (CFCl<sub>3</sub>). N<sub>2</sub>O's relatively small ODP is more than compensated by its large anthropogenic emission, making it the single most important of the anthropogenic ODS emissions today [*Ravishankara et al.*, 2009].

N<sub>2</sub>O is controlled under the Kyoto protocol and its current increase rate is estimated at 2.5% per decade [*WMO (World Meteorological Organisation)*, 2007]. However,

there is controversy whether this trend is reflected in stratospheric NO<sub>2</sub> concentrations. For instance, a long term trend estimate based on ground-based observations indicates that stratospheric NO<sub>2</sub> increased at twice that rate (5% per decade) between 1981 and 2000 [Liley *et al.*, 2000]. Satellite observations by instruments like SAGE-II/III (Stratospheric Gas and Aerosol Experiment) [Chu and McCormick, 1986], and more recently the Microwave Limb Sounder [Waters *et al.*, 1999], have made important contributions to the monitoring and understanding of the chemical state of the stratosphere. In this thesis I will investigate how OMI measurements of stratospheric NO<sub>2</sub> can contribute to the research of stratospheric chemistry, and the global trending of NO<sub>2</sub>.

#### 1.4 Forest fire aerosols

From its UV-channel, OMI detects aerosols equally well over land and over sea. This is due to the low surface albedo of both land and ocean in this wavelength range, and because the relative contribution of the surface reflection to the Earth radiance is smaller in the UV than at longer wavelengths [Torres *et al.*, 2007, Veihelmann *et al.*, 2007]. This is a major advantage compared to instruments like MODIS (Moderate resolution imaging spectroradiometer) that detect aerosols at visible wavelengths.

Aerosols of natural and anthropogenic origin are important to climate research because of their impact on Earth's radiation balance, either by absorption or reflection (direct effect), or because aerosols act as cloud condensation nuclei and change the albedo of clouds (indirect effect). The radiative forcing of the direct and indirect aerosol effect combined is estimated at  $-1.2 \text{ W/m}^2$  with, at best, a medium level of scientific understanding [IPCC, 2007]. As mentioned in Section 1.3, aerosols are relevant to atmospheric chemistry by providing a reaction surface for heterogeneous catalysis. Finally, aerosols are also relevant to air quality and health issues, as prolonged exposure to high aerosol loads can cause cardio-pulmonary disorders [Brook *et al.*, 2010].

Biomass burning and forest fires are important natural sources of aerosol, and these fire emissions contribute significantly to atmospheric composition on regional and global scales. Spaceborne observations assist in understanding relevant transport mechanisms and contribute to quantifying the impact of aerosol emissions in remote regions. An important parameter in the transport of aerosols is their altitude, where high altitudes in general prolong the aerosols' lifetime as the prevailing low humidity and low temperatures suppress scavenging, thereby augmenting the horizontal range over which they are transported. However, the altitude of aerosols is difficult to determine by passive remote sensing from space.

## 1.5 OMI retrievals

### 1.5.1 OMI retrieval of NO<sub>2</sub>

The DOMINO retrieval of tropospheric NO<sub>2</sub> from OMI involves three consecutive steps: slant column retrieval, stratosphere-troposphere separation and conversion into a vertical column. Slant columns of NO<sub>2</sub> are retrieved by a spectral fit to the Earth reflectance spectrum in the 405-465 nm spectral window [Boersma *et al.*, 2004] based on the DOAS method [Platt and Stutz, 2008] and using the OMI-measured solar spectrum as an NO<sub>2</sub>-free reference. These slant columns contain the integrated amount of NO<sub>2</sub> along the traversed light path. Separating the stratospheric and tropospheric contributions is a challenge for retrieval algorithms, and because uncertainties in the stratospheric column directly translate into errors in the tropospheric column an accurate retrieval of the stratospheric column is important. After subtracting the estimated stratospheric column, the remaining tropospheric slant column is converted into a vertical column by applying the tropospheric air mass factor that accounts for the average traversed path in the troposphere of the photons detected by OMI. Uncertainties in the NO<sub>2</sub> profile shape, surface albedo and cloud parameters, which are needed in the evaluation of the air mass factor, limit the accuracy of tropospheric NO<sub>2</sub> columns to 35-60% [Boersma *et al.*, 2004]. DOMINO uses cloud parameters from the OMI O<sub>2</sub>-O<sub>2</sub> algorithm [Acarreta *et al.*, 2004] and daily updated NO<sub>2</sub> profiles from simulations by the TM4 chemistry transport model (CTM) to calculate the tropospheric air mass factor. The results of various validation studies involving the DOMINO tropospheric NO<sub>2</sub> product are reviewed in Chapter 3, together with a discussion of possible improvements of the retrieval, based on these findings.

Several approaches to estimate the stratospheric contribution rely on the assumption that the stratospheric NO<sub>2</sub> field is smooth in the zonal direction, such as the reference sector method [Martin *et al.*, 2002a], or a wave-2 fit [Bucsela *et al.*, 2008]. DOMINO estimates the stratospheric contribution by assimilating OMI NO<sub>2</sub> columns in TM4, where observations over known polluted areas are assigned less weight. Up to now the quality of the DOMINO stratospheric NO<sub>2</sub> columns has not been properly evaluated. To address this issue, I will present in Chapter 4 an extensive comparison of DOMINO stratospheric NO<sub>2</sub> with independent ground-based observations. In that Chapter I will also show DOMINO captures spatial and temporal variations in stratospheric NO<sub>2</sub> on an hourly, daily and seasonal timescale.

### 1.5.2 OMI Absorbing Aerosol Index

The Absorbing Aerosol Index (AAI) is a parameter that represents the amount of UV absorption in the observed spectrum as compared to a pure molecular atmosphere

described by Rayleigh scattering over a Lambertian surface [Herman *et al.*, 1997]. The AAI is calculated from the ratio of the measured and predicted Earth reflectance at a certain UV wavelength, where the predicted reflectance is given by a radiative transfer model calculation using a surface albedo that is inferred from the measured reflectance at a second UV wavelength. In this work I will use the AAI that is included in the OMI TOMS Ozone product [Bhartia and Wellemeyer, 2002], where the AAI is calculated using the 331/360 nm pair.

Enhanced AAI values indicate the presence of UV-absorbing aerosols, whereas clouds yield zero or negative AAI values. The major advantage of AAI is that it can detect aerosols over a wide variety of scenes, including bright surfaces and clouds. This makes the AAI a powerful method for tracking aerosol plumes with satellite measurements, and it has been employed in various studies for that purpose [Herman *et al.*, 1997], [Fromm *et al.*, 2005], [de Graaf *et al.*, 2005]. However, the AAI does not represent one single aerosol property as it depends on parameters like altitude, single scattering albedo and optical depth [de Graaf *et al.*, 2005]. In Chapter 5, the OMI AAI is used to track and interpret the rapid around the world transport of an aerosol plume released by exceptionally intense forest fires in Australia in December 2006.

## 1.6 Aim and outline of this thesis

The work described in this thesis uses data from OMI to further the understanding of tropospheric and stratospheric nitrogen dioxide, and tropospheric aerosols. Essential to high quality data from the satellite is a rigorous and accurate calibration and characterization of the instrument prior to flight; this is something that the OMI team devoted considerable effort to. Discussed below are the results of significant efforts I contributed to the calibration of these important instrument parameters, especially the spatially dependent spectral slitfunction (Chapter 2) so critical to the retrieval of tracegas columns from OMI.

Additionally discussed are the retrieval algorithm and the interpretation of the OMI NO<sub>2</sub> data itself. Thus, my work on the retrieval and validation of tropospheric and stratospheric NO<sub>2</sub> by the DOMINO algorithm, and the interpretation of OMI observations is motivated by the following questions:

1. How to determine the spectral slitfunction of OMI?
2. How to set up, maintain and validate a near real time and offline retrieval of tropospheric NO<sub>2</sub> from OMI?



3. What is the quality of stratospheric NO<sub>2</sub> retrievals from OMI and what can we learn about the photochemical behavior and trends of stratospheric NO<sub>2</sub>?
4. How to use satellite data to monitor and characterize transport phenomena in the atmosphere?

The first question is answered in Chapter 2, where I report how OMI's spectral slitfunction is accurately characterized using a novel method based on an echelle grating to probe OMI's spectral resolution over its complete wavelength range with sub-resolution sampling. The second question is addressed in Chapter 3, which describes the retrieval of tropospheric NO<sub>2</sub> by the operational DOMINO system. I discuss the results of several validation and model studies where DOMINO data were involved, and based on these findings improvements to the retrieval of tropospheric NO<sub>2</sub> are proposed. The third question is the subject of Chapter 4, that presents a detailed discussion of the data assimilation approach used to derive the stratospheric NO<sub>2</sub> column from OMI. The accuracy of the OMI stratospheric NO<sub>2</sub> columns is investigated in a validation study involving ground-based observations. The second part of Chapter 4 deals with the scientific interpretation of OMI's 5+ year data set of global stratospheric NO<sub>2</sub> observations. The fourth question is answered in Chapter 5, describing how satellite observations from OMI and the CALIOP (Cloud-Aerosol Lidar with Orthogonal Polarization) spaceborne lidar, together with transport model simulations were used to characterize the circumnavigation of the globe by a smoke plume released by the exceptionally intense Australian bushfires of December 2006.

## Prelaunch characterization of the Ozone Monitoring Instrument transfer function in the spectral domain

### Abstract

A new method and an experimental measurement setup to accurately characterize the instrument transfer function in the spectral domain for hyperspectral spectrometers in the ultraviolet–visible wavelength range are described. The application to the on-ground calibration of the Ozone Monitoring Instrument on board the Earth Observing System Aura satellite is presented and discussed. With this method and setup, based on an echelle grating to severely limit transmitted wavelength bandpass to the instrument under test, the sampling of the instrument transfer function in the spectral domain can be selected and is not limited by the spectral resolution and sampling of the spectrometer that is being characterized. The importance of accurately knowing the OMI instrument transfer functions in the spectral domain for in-flight differential optical absorption spectroscopy retrievals and wavelength calibration is discussed. The analysis of the OMI measurement data is presented and shows that the instrument transfer functions in the spectral domain as a function of wavelength and viewing angle can be determined with high accuracy.

### 2.1 Introduction

The Dutch-Finnish Ozone Monitoring Instrument (OMI) was launched on board of the NASA Earth Observing System (EOS) Aura satellite on 15 July 2004. OMI is a hyperspectral instrument that passively probes the backscattered sunlight from the Earth's atmosphere in nadir in the spectral range of 270-500 nm. The instrument is equipped with two two-dimensional CCD detectors to obtain daily global coverage at

---

The contents of this chapter have been adopted from the paper by *Dirksen et al.* [2006], with minor modifications.

the equator with high spatial resolution. The telescope provides a cross-track field of view of  $115^\circ$ . The mission objectives of the OMI concern the recovery of the ozone layer, the depletion of ozone at the poles, tropospheric air pollution, and climate change. The Earth atmospheric retrieval techniques applied to OMI measurement data include algorithms developed for the NASA TOMS (Total Ozone Mapping Spectrometer) instrument [McPeters *et al.*, 1998] and DOAS (Differential Optical Absorption Spectroscopy [Platt, 1994, Plane and Smith, 1994, Veeffkind *et al.*, 2006]) algorithms developed for the OMI at KNMI.

Total column measurements of ozone, nitrogen dioxide and other trace gases are routinely made. The vertical distribution of ozone is determined by a method that makes use of the rapid increase in the ozone absorption cross section towards shorter wavelengths (Hartley bands) [Gotz *et al.*, 1934, Mateer and Deluise, 1992]. The OMI follows in the footsteps of predecessor instruments such as the Global Ozone Monitoring Experiment (GOME), the Scanning Imaging Absorption Spectrometer for Atmospheric Cartography (SCIAMACHY), the TOMS and the Solar Backscatter UltraViolet (SBUV) instrument.

For the OMI various of the Earth's atmospheric constituents and trace gases are retrieved using DOAS [Platt, 1994, Plane and Smith, 1994, Veeffkind *et al.*, 2006], for which an accurate characterization of the spectral instrument transfer function is essential. These gases include ozone (331.6–336.6 nm), nitrogen dioxide (405–465 nm), formaldehyde (324–357 nm), BrO (323–347 nm) and OCIO (363–402 nm). The retrieval techniques for these constituents are based on comparing the measured Sun-normalized Earth radiances (also called Earth reflectances) to high-resolution absorption cross section spectra from the literature convolved with the OMI instrument transfer function (ITF) in the spectral domain. The absorption cross section data from the literature have been obtained with dedicated experimental equipment under closely monitored experimental conditions (i.e., temperature and pressure) at higher spectral resolution than the OMI exhibits. Early in the OMI project the choice was made to follow this approach for DOAS-type retrievals. In an earlier publication the validity of the retrieval approach was discussed and demonstrated [Dobber *et al.*, 2005]. The alternative approach of using reference absorption spectra obtained with the instrument itself at various temperatures and pressures is not employed within the OMI project, although tests were made with both  $\text{NO}_2$  and  $\text{O}_3$  gases with the flight instrument.

An accurate characterization of the ITF in the spectral domain is essential for the retrieval of Earth's atmosphere constituents from the OMI measurement data. The ITF in the spectral domain is the instrument response to a monochromatic input signal. It is the monochromatic image of the entrance slit of the spectrometer on the CCD detector convolved with the response function of the detector. Furthermore, the OMI in-flight spectral calibration is done with the solar Fraunhofer lines (both Earth and Sun spectra) and atmospheric absorption lines (Earth spectra). The measured spectra are spectrally compared to a high-resolution solar spectrum and to

trace gas absorption spectra from the literature convolved with the ITFs. Hence an accurate characterization of the ITF is also important for accurate in-flight spectral calibration of the measured Earth and Sun spectra. For the OMI the ITF depends on wavelength (column or horizontal dimension on the CCD detectors) and viewing direction (row or vertical dimension on the CCD detectors) due to optical anomalies in the OMI spectrograph systems. Both dependencies must be characterized accurately to correctly interpret the instrument flight data. It is also important, given the applications for the OMI, to know the ITF accurately up to wavelengths  $3\sigma$  from the wavelength corresponding to the maximum of the ITF, where the instrument response typically becomes lower than 1% of the maximum. In this study  $\sigma$  is the Full Width at Half Maximum (FWHM), or simply width, of the profile. Given the above applications in the OMI project, the required scientific accuracy for the ITF has been set to 2% within  $\pm 2\sigma$  of the ITF maximum and to 10% between  $\pm 2\sigma$  and  $\pm 3\sigma$ . This is the accuracy with which the ITF needs to be characterized.

For the OMI a dedicated method and an experimental setup based on an echelle grating high resolution wavelength pre-sorter were developed to characterize the ITF accurately as a function of wavelength and viewing direction on the ground. This is the subject of this study. The OMI optical design will be described briefly in Section 2.2. Subsequently, the experimental setup for characterizing the ITF and the analysis of the measurement data will be described. It will be shown that with this equipment and these analysis methods the ITF in the spectral domain can be characterized with the required high accuracy.

## 2.2 *The Ozone Monitoring Instrument (OMI)*

The OMI is equipped with a telescope system that enables the observation of the Earth at an altitude of approximately 705 km with an instantaneous cross-track field of view of  $115^\circ$  to provide daily global coverage at the equator. The telescope, consisting of a primary convex telescope mirror, a polarization scrambler and a secondary convex telescope mirror, images the Earth's light onto the spectrometer's entrance slit (44 mm long, 0.3 mm wide). The instrument has separate UV and visible (VIS) optical channels each equipped with a 780 pixel  $\times$  576 pixel CCD detector that is operated in binned mode with a binning factor of 8 (global mode) to provide spectra of 780 pixels in the spectral dimension and 60 pixels in the viewing direction dimension. The resulting ground pixel sizes per channel are listed in Table 2.1, along with a number of other OMI parameters. The UV channel is optically divided into a wavelength range below 311 nm (UV1) and one above 307 nm (UV2), which are imaged on different regions of the same CCD detector. This has been done to suppress spectral stray light and to optimize the instrument's optical and electronic settings for the wavelength range below 311 nm separately, because in that wavelength range the Earth's fluxes decrease by three to four orders of magnitude

as a result of absorption by ozone in the Hartley-Huggins bands. In addition to the Earth view optical path, the OMI also has a separate Sun measurement port that can be closed when not looking at the Sun. Sunlight illuminates one of three reflectance diffusers that are mounted on a carousel mechanism. A folding mirror located on another mechanism reflects the sunlight to the polarization scrambler and the remainder of the optical system while blocking the Earth's light. The remainder of the optical system, including the secondary telescope mirror and the entrance slit of the spectrometer, is exactly the same for the Sun and Earth viewing modes. The OMI is also equipped with a white-light source that illuminates the entire entrance slit by means of a transmission diffuser. The white-light source is used mainly for detector calibration purposes. For on-ground measurements there also was a possibility of illuminating the transmission diffuser via the white-light source path using external light sources. This optical path is called the calibration port. The Sun port, white-light source port, and the calibration port have in common that they can all illuminate the entire entrance slit of the spectrometer with more or less parallel beams. To achieve this in the Earth mode the complete  $115^\circ$  field of view needs to be illuminated. The calibration port of the OMI was used on the ground for the ITF characterization measurements described in this Chapter. In this way all viewing directions could be investigated simultaneously. Further details on the optical and electronic design of the OMI can be found elsewhere [Dobber *et al.*, 2006, Levelt *et al.*, 2006a,b, van den Oord *et al.*, 2006, Dirksen *et al.*, 2004, Dobber *et al.*, 2004, de Vries *et al.*, 2002, Laan *et al.*, 2001].

## 2.3 ITF characterization measurements and results

### 2.3.1 Echelle grating ITF characterization setup and measurements

The optical configuration of the echelle ITF characterization optical stimulus is schematically shown in Figure 2.1 [Smorenburg *et al.*, 2003]. A 150 W high-pressure xenon arc discharge lamp is imaged by a Schwarzschild mirror configuration on the entrance slit of an echelle monochromator. The light passing through the input slit is imaged as a parallel beam on the echelle grating by the concave mirror to the left in Figure 2.1. Due to the high blaze angle, the echelle grating is illuminated at near grazing incidence, and the diffracted beam travels back almost in the same direction as the initial white-light beam. The output slit transmits only a small part of the echelle spectrum resulting in an extremely small spectral bandpass. A system of two convex lenses, not shown in Figure 2.1, parallelizes the beam toward the OMI, which is located in the thermal-vacuum chamber at flight representative temperature (optical bench, 264 K; detectors, 265 K) and pressure ( $<10^{-5}$  mbar) environmental conditions. The echelle optical stimulus beam with a diameter of approximately 50 mm illuminated the OMI calibration port homogeneously, which

**Table 2.1** OMI properties.

Property	Value
Spectral range	UV1: 264-311 nm UV2: 307-383 nm VIS: 349 - 504 nm
Spectral sampling	UV1: 0.33 nm / px UV2: 0.14 nm / px VIS: 0.21 nm / px
Spectral resolution (FWHM)	UV1: 1.9 px = 0.63 nm UV2: 3.0 px = 0.42 nm VIS: 3.0 px = 0.63 nm
Telescope cross-track swath field of view	115° (2600 km on the ground)
Telescope along track flight instantaneous field of view	1.0° (13 km on the ground)
Ground pixel size at nadir, global mode (electronic binning factor 8)	UV1: 13 km x 48 km, 30 binned pixels UV2: 13 km x 24 km, 60 binned pixels VIS: 13 km x 24 km, 60 binned pixels
Silicon CCD detectors	780 x 576 (spectral x spatial) pixels
Operational CCD temperature	UV: 265.07 K VIS: 264.99 K
In-orbit CCD temperature excursion	UV and VIS: $\pm 10$ mK (stabilized)
Operational optical bench temperature	264 K
In-orbit optical bench temperature excursion	$\pm 300$ mK
Duty cycle	60 minutes on daylight side (Earth and Sun measurements) 10-30 minutes on eclipse side (calibration measurements)
Average data rate	0.8 Mbps
Power	66 W
Mass	65 kg
Size	50 cm x 40 cm x 35 cm
Orbit	Polar, Sun-synchronous Average altitude: 705 km Orbit period: 98 minutes 53 seconds Ascending node local time: 1:42 PM

enables accurate ITF characterization measurements of all pertinent viewing angles simultaneously.

It is of *crucial* importance for accurate characterization of the ITF in the spectral domain that the 0.3 mm width of the OMI entrance slit be illuminated homogeneously or unrepresentative ITF's will be obtained. The exit beam of the echelle

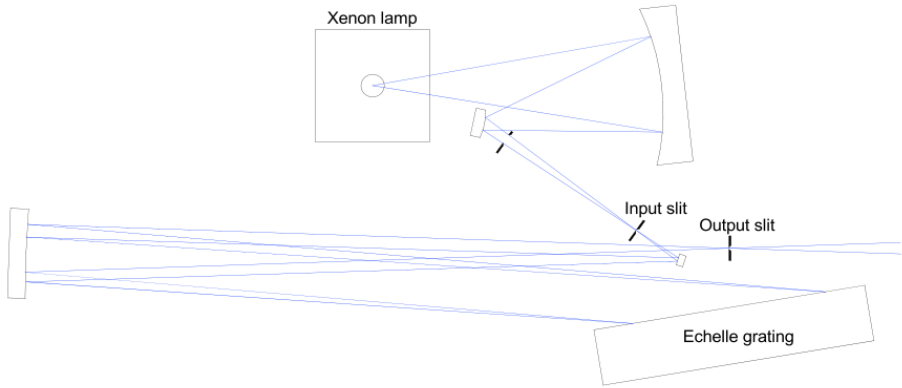


**Figure 2.1** *Schematic optical layout of the echelle grating optical stimulus to characterize the instrument transfer function in the spectral domain.*

grating optical stimulus is sufficiently spatially uniform for all wavelengths in the range of 270-500 nm. The transmission diffuser inside the OMI in the calibration port optical path improves this uniformity further, thus ensuring that the width of the OMI entrance slit is illuminated homogeneously. The echelle grating, which is made from zerodur with an aluminum coating, is the most critical component of the experimental setup. The grating surface is 50x220 mm<sup>2</sup> and the blaze angle is 76°. The grating is ruled with 72 lines/mm, resulting in a grating constant  $d$  of  $1.39 \times 10^{-5}$  m. The incidence angle and the angle of diffraction on the grating are approximately 74.5° and 75.5°, respectively. The wavelengths of the grating orders in the exit beam can be calculated from the grating equation

$$d(\sin \theta_i + \sin \theta_d) = m\lambda \quad (2.1)$$

where  $d$  the grating constant of  $1.39 \times 10^{-5}$  m,  $\lambda$  is the air wavelength,  $\theta_i$  is the angle of incidence of approximately 74.5°,  $\theta_d$  is the angle of diffraction of approximately 75.5°, and  $m$  is the grating diffraction order. These echelle grating properties result in an exit beam that contains many spectrally narrow orders: in the OMI UV1 channel approximately 15 orders (from  $m=87$  to 101 at an incidence angle of approximately 74.5°), in the UV2 channel approximately 18 (from  $m=70$  to 87 at an incidence angle of approximately 74.5°), and in the VIS channel approximately 23 (from  $m=54$  to 76 at an incidence angle of approximately 74.5°). An example of a measured spectrum is shown in Figure 2.2 for the central nadir row. The peak separation between adjacent orders is smaller for lower wavelengths in the UV1 channel (approximately 2.7 nm at 266 nm between  $m=100$  and 101) and larger for higher wavelengths in the VIS channel (approximately 9.0 nm at 496 nm between  $m=54$  and 55).

The entrance and exit slits of the echelle grating optical stimulus can be chosen

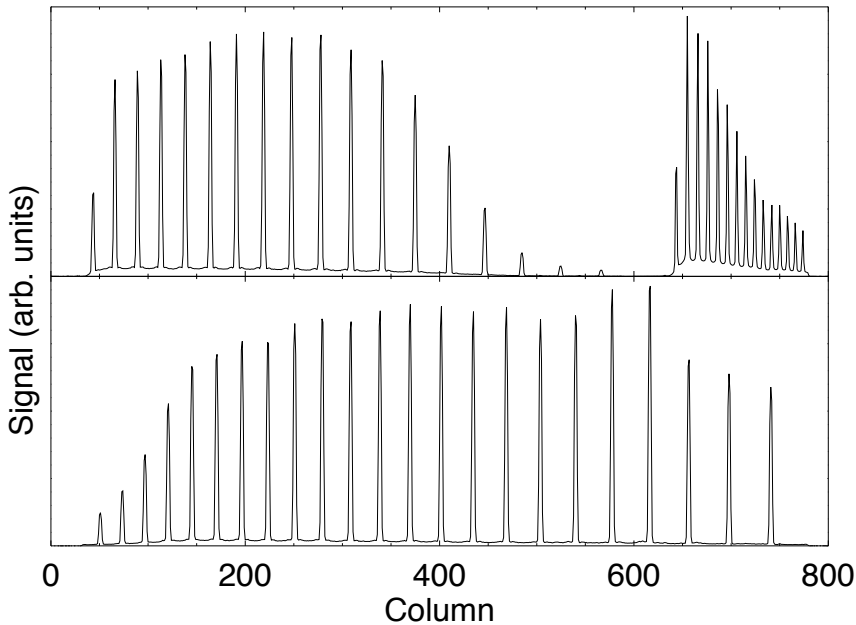


**Figure 2.2** Echelle spectrum measured by the OMI: top panel, UV1 channel (right) and UV2 channel (left); lower panel, VIS channel. The column dimension is the spectral dimension. The stimulus stray light shows up as a background, most notably in the UV1 channel (columns 600-800 in the UV channel).

from three sets: nominal resolution ( $0.5 \times 8.0 \text{ mm}^2$ ), medium resolution ( $1.0 \times 8.0 \text{ mm}^2$ ) or low resolution ( $2.0 \times 8.0 \text{ mm}^2$ ). The entrance and exit slits are the same size. In these ranges of slit widths the spectral widths of the output grating orders scale linearly with the widths of the slits, whereas the output flux scales quadratically with the widths of the slits. For the OMI measurements slits with a width of 0.5 mm were used. For these slits the FWHM  $\Delta\lambda$  of the spectral grating orders in the exit beam was calculated. The results are shown in Table 2.2. Over the spectral range of the OMI,  $\Delta\lambda$  varies from 0.028 nm at 270 nm to 0.053 nm at 500 nm, which is at least an order of magnitude lower than the spectral resolution of the OMI at these wavelengths (see Table 2.1). This is an important prerequisite for accurate ITF characterization measurements, because otherwise the width of the echelle grating order lines cannot be neglected in the ITF measurement analysis.

The echelle grating is mounted on a computer-controlled rotational stage, which enables accurate and reproducible angular movement of the grating. During the OMI measurements an angular step size of  $0.02^\circ$  was employed, corresponding to a



**Table 2.2** *Calculated spectral resolution for various grating orders<sup>a</sup>.*

Echelle-grating order $m$	$\lambda_{\text{air}}$ (nm)	$\Delta\lambda$ (nm) FWHM
54	496.9	0.053
55	487.9	0.051
60	447.2	0.047
65	412.8	0.043
70	383.3	0.041
75	357.8	0.038
80	335.4	0.036
85	315.7	0.033
90	298.1	0.031
95	282.5	0.030
99	271.0	0.028
100	268.3	0.028

<sup>a</sup>The grating orders are given for a nominal slit width of 0.5 mm. The value of  $\Delta\lambda$  is the Full Width at Half Maximum (FWHM) of the spectral grating order peaks in the exit beam.

wavelength shift of approximately 0.04 nm for an order near 490 nm. This feature of the echelle grating ITF characterization optical stimulus is one of the more essential ones. An echelle stimulus spectrum at a fixed grating position as measured by the OMI shows the ITF profiles of all grating orders present in the stimulus exit beam with at most five measurement points (CCD pixels) per line at a the viewing direction under consideration, as shown in the top panel of Figure 2.3. However, if we focus on the response of a single CCD detector pixel as a function of echelle grating rotation angle, the number of sampling points in the measured ITF is determined by the step size of the grating rotation, as shown in the lower panel of Figure 2.3, rather than by the spectral sampling and resolution of the OMI, as would be the case for conventional methods of determining the ITF. This measurement principle enables a characterization of the ITF using typically 10 times more sampling points to fit the ITF response shape accurately. For the OMI measurements the echelle grating was scanned over a 5° angular range centered around the blaze angle of 76°. At the blaze angle the reflection efficiency of the grating is at a maximum, so, by scanning around this angle, the highest stimulus output is obtained. With the 5° scanning range every detector pixel sees the complete passage of at least one grating order. The measurements were performed with the OMI in a thermal-vacuum chamber at flight-representative thermal-vacuum conditions (with an optical bench temperature of 264 K). This is important, because the ITFs are expected to change slightly with the temperature of the optical bench. By illuminating the instrument by means of the calibration port transmission diffuser, all CCD rows are illuminated instantaneously. The ITFs for all viewing directions and wavelengths are measured

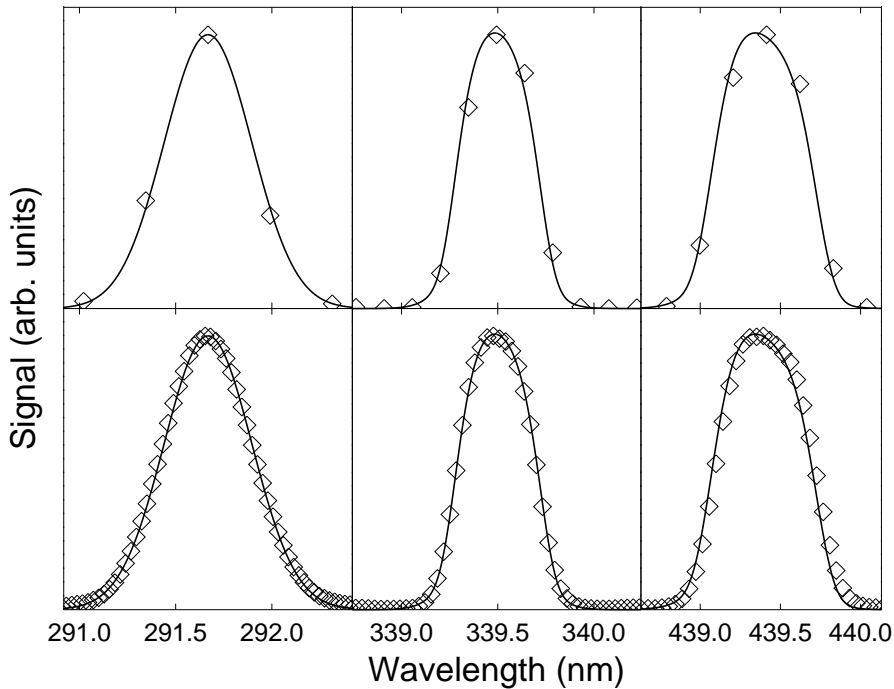


**Figure 2.3** *The ITF in the spectral domain of the OMI is typically sampled by 4–5 detector pixels. By using the dedicated echelle grating ITF characterization optical stimulus a sampling of the ITF that is ten times higher is obtained. The plots to the left compare a spectral peak registered by the OMI CCD in the UV1 channel (upper plot) to the same peak sampled using the ITF characterization optical stimulus (lower plot). The same for the UV2 (middle) and VIS channels (right).*

in one measurement run, which takes approximately 24 hours. It is important to correct for the echelle grating efficiency variation as a function of rotation angle and for the stray light originating from the grating in the optical stimulus. Both corrections are discussed in detail in Section 2.4.

The echelle grating ITF characterization optical stimulus has also been used to derive the on-ground spectral calibration of the OMI. Whereas accurate knowledge of the wavelengths of the grating order peaks is not important for characterization of the ITFs, it is important for performing the wavelength calibration of the OMI. The actual optical stimulus parameters are known with insufficient accuracy for this purpose, and for this reason the stimulus has to be commissioned with respect to external sources. The OMI wavelength calibration is described by polynomial expressions in the column dimension (wavelength dimension) for each row (viewing direction) and for each optical channel (UV1, UV2, VIS). By use of the echelle grating

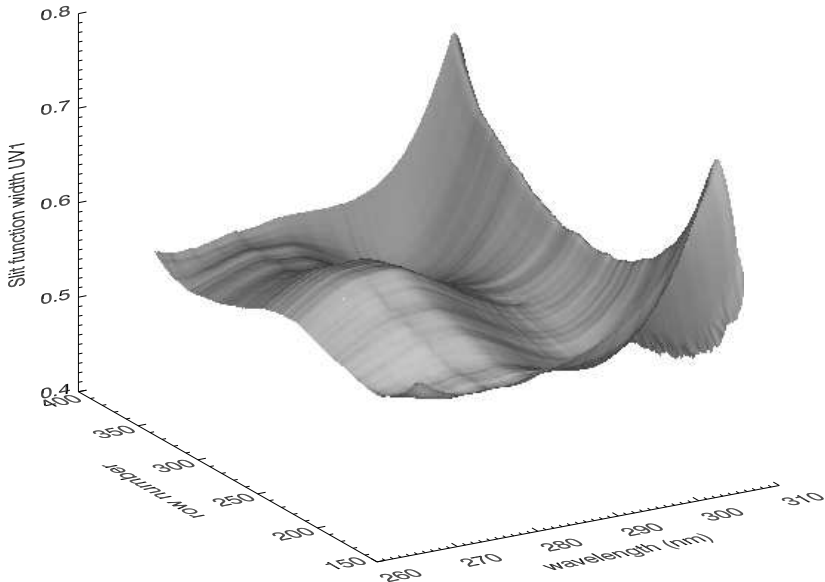


**Figure 2.4** Width of the ITF in the spectral domain as function of wavelength and row number for the UV1 channel.

optical stimulus all polynomial coefficients but the zero-order term (independent of column) can be calibrated accurately. The zero-order coefficient was determined by comparing the echelle stimulus measurements to measurements with a hollow-cathode low-pressure PtCrNeAr discharge lamp, see e.g., *Mount et al.* [1977], for which the emission line wavelengths are known with high accuracy. This enabled a pre-launch wavelength calibration to an accuracy of approximately 0.1 pixel, which is the requirement for the pre-launch spectral calibration accuracy. The in-flight wavelength scale is obtained by fitting the solar Fraunhofer absorption lines and the absorption lines from the Earth's atmospheric constituents and trace gases in the measured spectra to a high resolution solar spectrum [*Kurucz et al.*, 1984] and to the absorption cross section literature reference spectra for the Earth's atmospheric constituents and trace gases until an optimal match is found at all pertinent wavelengths. This calibration, which will not be discussed in further detail here, has an accuracy of approximately 0.01 pixels, which equals the scientific requirement for the in-flight spectral calibration accuracy. The in-flight requirement for spectral calibration accuracy is determined by the application of the DOAS retrieval technique to obtain the concentrations of the Earth's various atmospheric

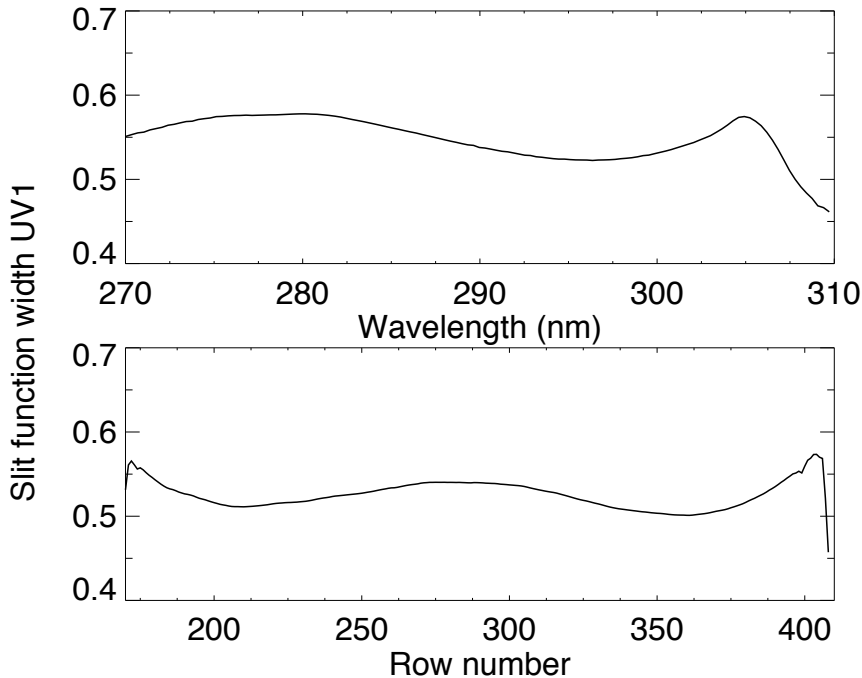


**Figure 2.5** Cross sections of the spectral width of the ITF as function of wavelength for row 300 (top panel) and row number for a wavelength of 290 nm (bottom panel) for the UV1 channel.

constituents and trace gases.

The possibilities of the echelle grating ITF characterization optical stimulus can be compared to the possibilities of the traditional method of using a hollow-cathode low-pressure discharge lamp (e.g., PtCrNeAr) and to the possibilities of using a wavelength-tunable laser. The echelle grating optical stimulus has a large number of spectrally narrow (compared to the OMI sampling and resolution) and well-separated lines, whereas the discharge lamp has a large number of narrow lines, which are often blended and not always optimally distributed over the wavelength range. A wavelength-tunable laser emits only one nearly monochromatic spectral line, and to cover a large wavelength range from ultraviolet to visible or even near-infrared, a specialized and complex laser setup is required. Both the echelle grating and laser setups are tunable over very small wavelength changes. This is not the case for the spectral lamp. A laser has significantly higher output flux than the echelle grating stimulus or the spectral lamp, but the advantage in measurement time is lost by the fact that laser emits only one line, whereas the other two sources can measure different wavelength regions at the same time. Thus the total measurement time

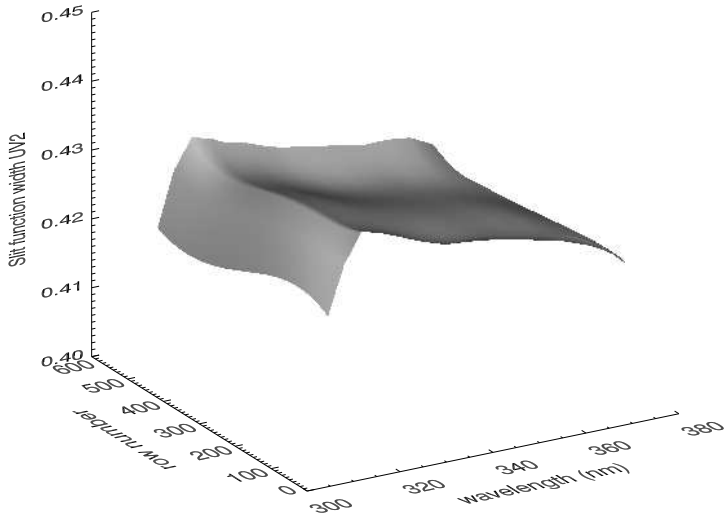


**Figure 2.6** *Spectral width of the ITF as a function of wavelength and row number for the UV2 channel.*

will be comparable. A narrow laser beam will need to be expanded to fill the entrance slit of the instrument homogeneously, which further reduces the flux. A tunable laser is optimally suited for characterizing the ITF outside  $2\text{--}3\sigma$  from the spectral peak maximum. This is more difficult for the spectral lamp, given the line blending and pressure broadening often present, and for the echelle grating stimulus, which has to be corrected for the spectral stray light in between the grating order peaks (see Section 2.4).

#### 2.4 Echelle grating instrument transfer function results

During the OMI on-ground calibration-phase ITF measurements, five unbinned CCD images (576 rows) were recorded for every echelle grating position. These images were averaged to improve the signal-to-noise ratio (SNR) of the measurements. The CCD dark current signal was corrected for by subtracting a dedicated measurement performed with the stimulus switched off. Furthermore, the measurement data were corrected for all OMI detector and electronic settings. The OMI ITF is determined

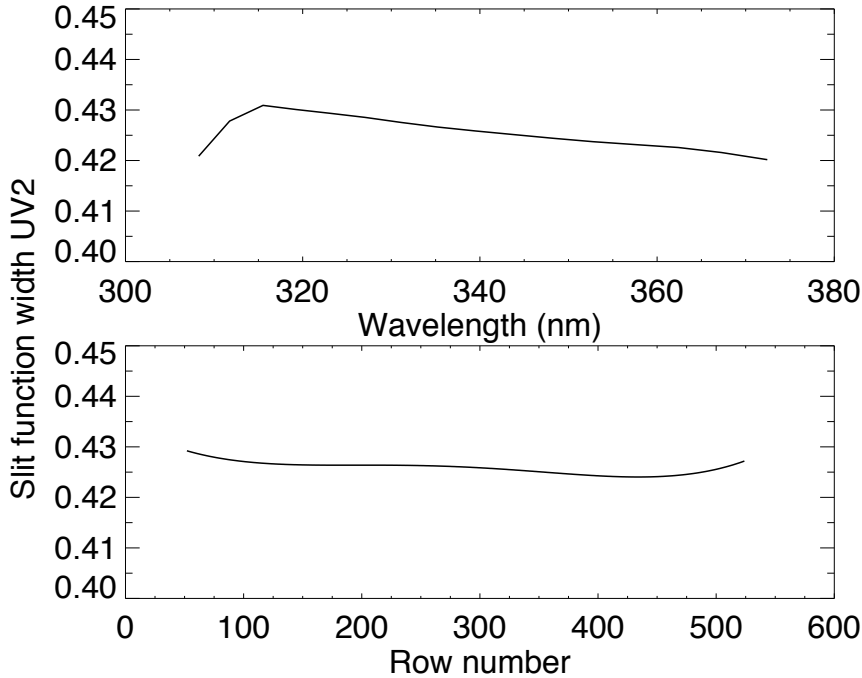


**Figure 2.7** Cross sections of the spectral width of the ITF as a function of wavelength for row 300 (top panel) and row number for a wavelength of 343 nm (bottom panel) for the UV2 channel.

by measuring the response of a CCD pixel to a passing echelle peak of the optical stimulus. This is measured simultaneously for all CCD pixels, i.e., all wavelengths and viewing angles. The rotation of the echelle grating changes the incidence and diffraction angles on the echelle grating. This changes the wavelengths of the diffraction orders according to Equation 2.1. The rotation of the echelle grating also influences the intensity of the peaks in the output beam, as the grating efficiency depends on  $\theta_i$  and  $\theta_d$ . As a consequence the measured signal in each CCD pixel consists of the combined effect of the ITF response to a passing echelle peak and the more slowly varying intensity of that peak. For an accurate characterization of the ITF there must be a correction for the latter effect. The intensity variations as a function of echelle grating angle have to be corrected for each grating order individually, because the grating efficiency change as a function of illumination geometry is wavelength dependent. The use of a broad-band detector to monitor the output of the stimulus for this purpose is not sufficient because this detector records the integrated reflectivity of the echelle grating over all wavelengths rather than the wavelength-dependent intensity as a function of grating rotation angle. This would

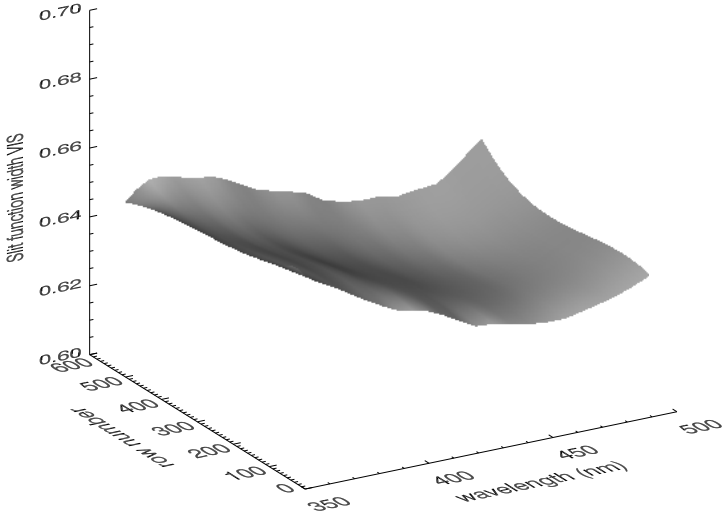


**Figure 2.8** Spectral width of the ITF as a function of wavelength and row number for the VIS channel.

make the grating efficiency correction far less accurate and reduce the accuracy of the ITF characterization. The relation between the peak intensities and the grating angles was determined by fitting the position and amplitude of each grating order peak within the OMI wavelength range as it moves over the CCD detector. By using the known radiometric sensitivity of the OMI as a function of wavelength and viewing angle, the relative output flux of each peak in the optical stimulus output beam as function of the grating position is calibrated. The radiometrically calibrated OMI is thus used to calibrate the wavelength-dependent output flux of the echelle grating ITF characterization optical stimulus. The stimulus output flux correction is accurate to approximately 1.5%.

The images recorded by the OMI also need to be corrected for the spectral stray light originating from the echelle optical stimulus itself. This spectral stray light originates mainly from the echelle grating and shows up as a more or less wavelength-independent background, as can be seen in Figure 2.2. At low signal levels, i.e., at wavelength separations of more than  $3\sigma$  from the maximum of the ITF response, it becomes increasingly difficult to distinguish between spectral stray light from the optical stimulus and the wings of the ITF itself. This is a disadvantage of the

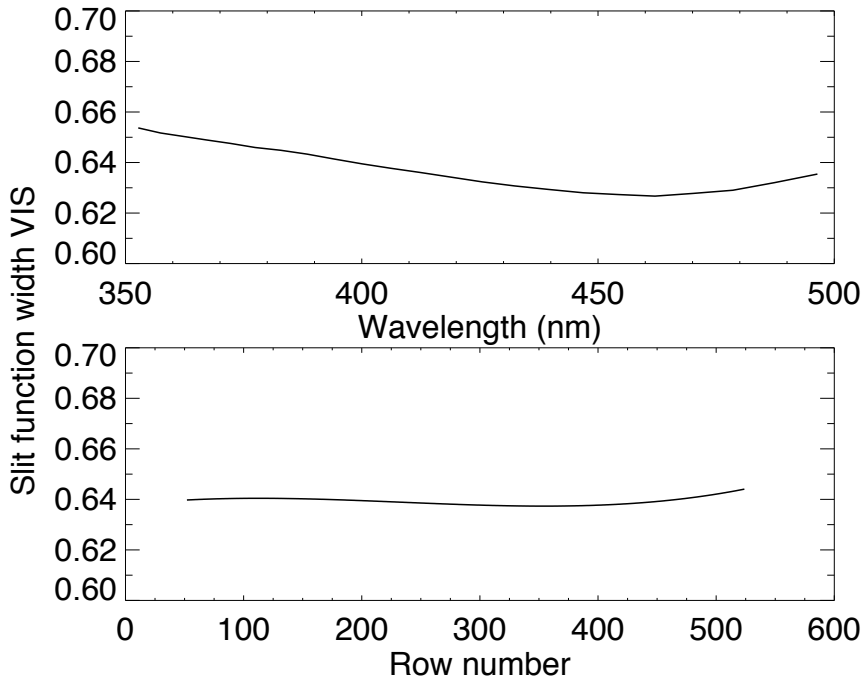


**Figure 2.9** Cross sections of the spectral width of the ITF as a function of wavelength for row 300 (top panel) and row number for a wavelength of 406 nm (bottom panel) for the VIS channel.

echelle grating ITF characterization optical stimulus as compared to a wavelength tunable laser, for example, for which the spectral stray light at wavelengths  $3\sigma$  from the maximum of the ITF response can be made negligible. For the echelle grating optical stimulus the spectral stray light was minimized in the design by the use of baffles and the entrance and exit slits; however, most of the stray light comes from the grating itself, and so the stray light cannot be neglected in the data analysis.

Both the spectral distribution and the intensity of the spectral stray light originating from the optical stimulus depend on the echelle grating position. This necessitates determining the shape of the stray light background for measurements at each grating position before applying the stray light correction. The shape of the stray light background as a function of wavelength is determined by interpolating between the signal levels in between the grating order peaks. The magnitude of the optical stimulus spectral stray light increases from approximately 2% in the VIS channel to approximately 10% in the UV1 channel. Independent spectral stray light measurements on the OMI using different optical stimuli have confirmed that the stray light observed in the echelle grating optical stimulus measurements originates



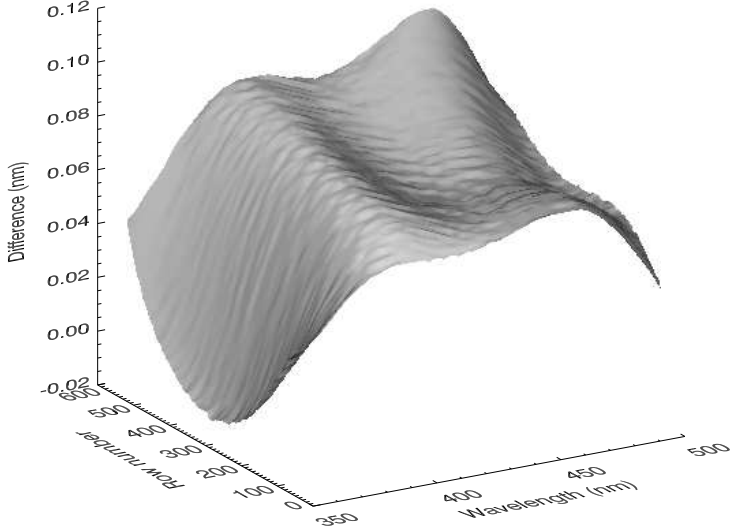


**Figure 2.10** Surface plot of the asymmetry of the ITF in the spectral domain in the VIS channel. Asymmetry is given as the difference between the wavelength distance  $\lambda_p$ -left 50% point and  $\lambda_p$ -right 50% point, with  $\lambda_p$  being the wavelength of the profile maximum.

from the stimulus itself rather than from the OMI for which the spectral stray light is much smaller [Dobber *et al.*, 2006]. With the method described above the accuracy of the stray light correction from the optical stimulus is approximately 1% within  $\pm 2\sigma$  from the maximum of the ITF profile and approximately 10% between  $\pm 2\sigma$  and  $\pm 3\sigma$ , where the useful signals of the ITF profile are much smaller. Given the SNR (uncertainty smaller than 0.5%), reproducibility, and accuracy of the radiometric (1.5%) and stimulus stray light corrections (see above), the accuracy of the measured OMI ITFs as a function of wavelength and viewing angle is 1.9% within  $\pm 2\sigma$  of the profile maximum and approximately 10% between  $\pm 2\sigma$  and  $\pm 3\sigma$  of the profile maximum, which is within the required numbers of 2% and 10%, respectively. The individual uncertainties are independent of each other.

It was found that the measured ITF profiles can be fitted adequately by the following analytical function:

$$A_0 e^{-\left(\frac{x-x_0}{w_0}\right)^2} + A_1 e^{-\left(\frac{x-x_1}{w_1}\right)^4} \quad (2.2)$$

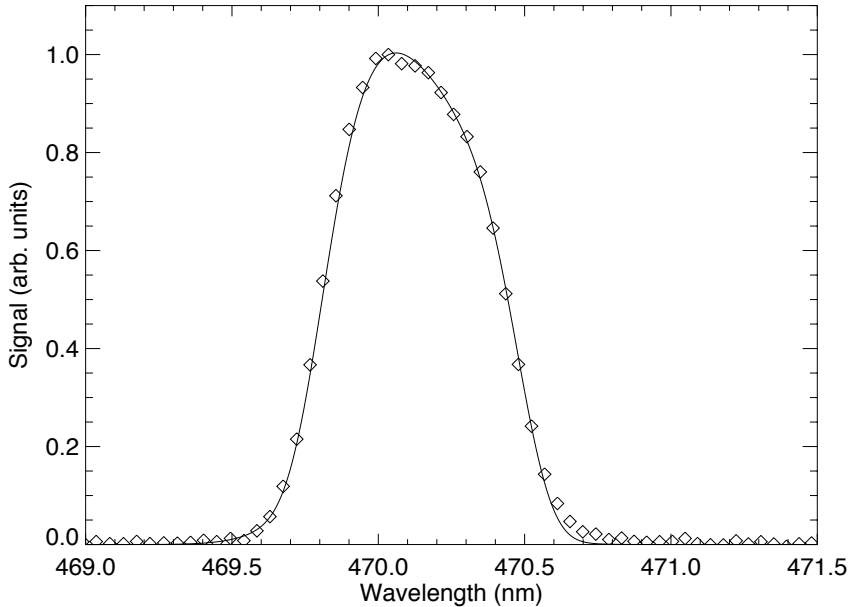


**Figure 2.11** Example of an asymmetric ITF in the spectral domain in the VIS channel at row 499 and wavelength 470 nm.

where  $A_0$  represents the amplitude;  $x_0$  is the central position;  $w_0$  is the width of the Gauss term; and  $A_1$ ,  $x_1$  and  $w_1$  represent the same parameters for the second term. This function combines a standard Gauss function and a term that yields a profile that has steeper flanks and a flatter top than the regular Gauss function. This function is well suited to describe symmetrical Gaussian-shaped profiles, as well as broadened and asymmetrical profiles as measured for the OMI ITF. Figure 2.3 shows that the ITF in the UV1 optical channel can be described adequately by a simple Gaussian, whereas the ITF's in the UV2 and VIS channels are shaped differently, which necessitates the use of both terms in Equation 2.2.

The FWHM of the ITF directly relates to the spectral resolution of the OMI and is in case of the UV1 channel calculated directly from the fitted Gauss parameter  $w_0$ . For the UV2 and VIS channels there is no simple analytical expression for the ITF FWHM and it is therefore calculated numerically. The measured and analyzed ITF profiles are fitted for all rows (viewing directions) and for all columns (wavelengths) in all spectral channels with the analytical function described in Equation 2.2. The variation of the ITF spectral width as a function of channel, wavelength, and row number (viewing angle) is shown in Figures 2.4–2.9. Figures 2.4, 2.6, and 2.8 show

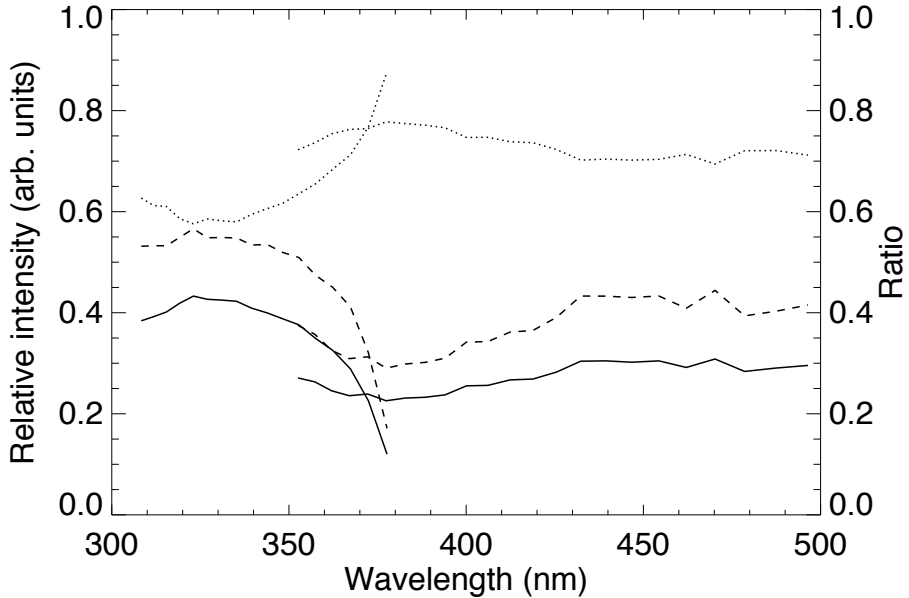


**Figure 2.12** Wavelength dependence of the ITF parameters  $A_0$  and  $A_1$  for row 300 in the UV2 and VIS channels. Solid curve and left scale:  $A_0$ , dotted curve and left scale:  $A_1$ , dashed curve and right scale:  $A_0/A_1$ .

surface plots of all variables, and Figures 2.5, 2.7, and 2.9 show the cross section plots of the ITF spectral width for all three spectral channels. As can be seen from the figures, the ITF width depends on both wavelength and row number. For the UV2 and the VIS channels the width of the ITF varies approximately 5% with wavelength, whereas the variation with row number is considerably smaller. In the UV1 channel these variations are larger with up to 10% variation in width in the row direction and as much as 20% variation in the spectral direction. Furthermore, a discontinuous behavior of the ITF width is observed at approximately 305 nm. From 295 to 305 nm the width increases with wavelength and then suddenly decreases from 305 to 310 nm. The onset of the observed discontinuous behavior coincides with the beginning of the UV1/UV2 overlap region. This behavior is caused by the segmented mirror that is used to separate the UV1 and UV2 channels in the OMI [Dobber *et al.*, 2006]. In the UV channel an intermediate spectrum is imaged on a segmented mirror that reflects the part of the spectrum below 310 nm into the UV1 channel and the wavelengths above 310 nm into the UV2 channel. Wavelengths in the overlap region of 305–310 nm end up in both channels, which effectively causes

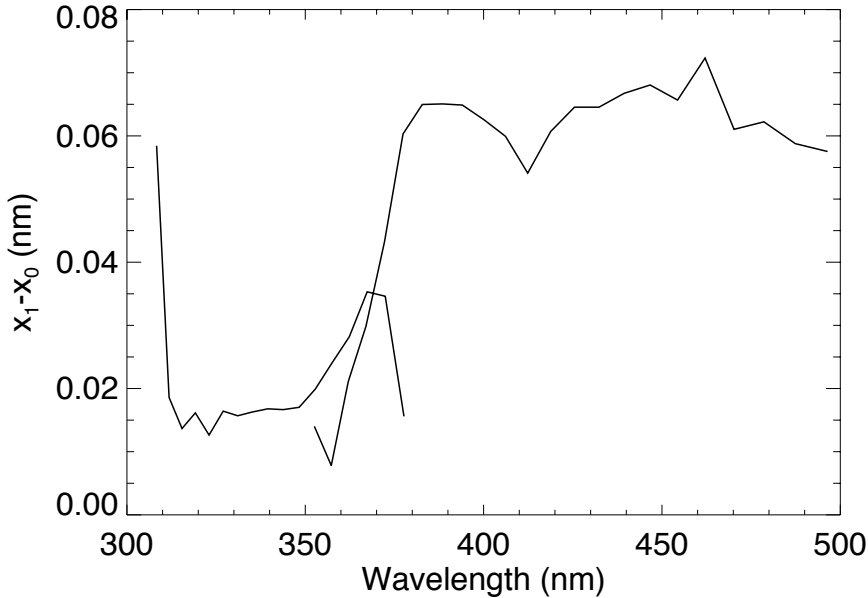


**Figure 2.13** Wavelength dependence of the difference between ITF parameters  $x_1$  and  $x_0$  for row 300 in the UV2 and VIS channels. This is the difference between the central wavelengths of the Gaussian and the  $\exp(-x^4)$  terms in Equation 2.2.

vignetting of the beam, resulting in a narrower ITF for the wavelengths involved.

Figure 2.10 illustrates the asymmetry in the VIS channel. The difference in the absolute wavelength differences between the wavelengths at the profile maximum and at half-maximum is shown as a function of wavelength and row number (viewing angle). For nearly all viewing angles and wavelengths the measured IFT is asymmetric, except for the cases where the vertical axis value equals zero. Figure 2.11 shows the measured and fitted profile at row 499 and wavelength 470 nm in the VIS channel. This profile is asymmetric, in agreement with the results shown in Figure 2.10. Figure 2.12 shows the amplitudes and ratio of the amplitudes of the two terms in Equation 2.2 for row 300 in the UV2 and VIS channels. In the UV2 channel the Gaussian term contribution decreases with increasing wavelength while the contribution of the already dominant second term increases with increasing wavelength. In the VIS channel the second term in Equation 2.2 is equally dominant over the first Gaussian term for all wavelengths. Figure 2.13 shows a similar plot for the wavelength difference  $x_1 - x_0$ . This plot also shows that the measured ITF profile is asymmetric in the VIS channel and more symmetric in the UV2 channel.

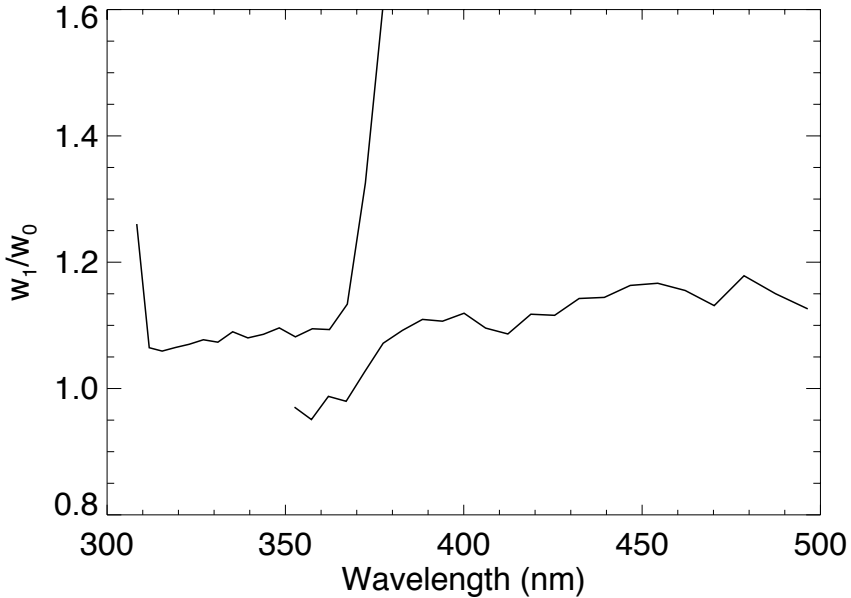


**Figure 2.14** Wavelength dependence of the ratio of the ITF parameters  $w_0/w_1$  for row 300 in the UV2 and VIS channels. This is the ratio of the width of the Gaussian and the  $\exp(-x^4)$  terms in Equation 2.2.

Figure 2.14 shows the ratio of the widths of the two terms in Equation 2.2 for row 300 in the UV2 and VIS channels.

## 2.5 Conclusions

A new measurement method and an echelle-grating-based experimental technique to accurately characterize the wavelength-dependent ITFs in the spectral domain of hyperspectral spectrometers have been presented. The application of this method in the on-ground calibration of the Earth Observing System OMI has been shown. The most important feature of this new method is that the sampling of the measured ITFs in the spectral domain can be chosen from the measurement setup and is not limited by the resolution or sampling rate of the spectrometer that is being characterized. Additionally, the presence of many spectral orders in the narrow spectral bandpass results in considerable time savings over other methods. The OMI spectral ITFs in the spectral domain have been characterized with high accuracy and within the

requirements as a function of wavelength and viewing angle. The necessary steps to correct and analyze the data have been described. An accurate knowledge of the OMI ITF in the spectral domain is essential for the Earth's atmospheric constituent retrieval algorithms and in the in-flight wavelength calibration.

### *Acknowledgements*

This research was funded by the Netherlands Agency for Aerospace Programmes (NIVR) within the framework of the Ozone Monitoring Instrument (OMI) project. We thank TNO TPD for designing (in particular Huib Visser), building and commissioning the echelle grating optical stimulus.



## Retrieval of tropospheric NO<sub>2</sub> from OMI with the Dutch OMI NO<sub>2</sub> system (DOMINO)

### 3.1 Introduction

This chapter describes the operational DOMINO (Dutch OMI NO<sub>2</sub>) system to retrieve tropospheric NO<sub>2</sub> columns from OMI measurements. The DOMINO product provides daily global measurements of tropospheric NO<sub>2</sub> columns at unprecedented spatial resolution (24x13 km<sup>2</sup> ground pixel size at nadir), which allows for the observation of sources of near-urban size. One of the novelties of DOMINO concerns the availability of a near-real time (NRT) product that is provided within 3-4 hours after measurement.

DOMINO data are widely used, for example in air quality forecast models such as the THOR project (<http://thor.dmu.dk>, *Hvidberg and Brandt [2009]*), and in the EU-funded GMES (Global Monitoring for Environment and Security) MACC (Monitoring Atmospheric Composition and Climate) project (see <http://www.gmes-atmosphere.eu/services/gac/reanalysis/>). Scientific applications involve using DOMINO observations to compare to the output of the AIRPACT air quality forecast model in the US Pacific north-west [*Herron-Thorpe et al., 2010*], to detect the emissions of new power plants in Mongolia [*Zhang et al., 2009*], the reduction of NO<sub>x</sub> emissions resulting from the traffic ban during the Sino-African summit in November 2006 [*Wang et al., 2007*], which was a dry-run for reducing the tropospheric NO<sub>2</sub> burden during the Olympic Games of 2008 [*Mijling et al., 2009*], and, in combination with SCIAMACHY measurements, to detect the diurnal variation of NO<sub>2</sub> in the troposphere [*Boersma et al., 2008, 2009*].

My responsibilities in the DOMINO project included maintenance of the system, ensuring the continuity of the processing of the near-real time and the offline data streams, algorithm updates and a major reprocessing operation which resulted in a consistent data set, version 1.0.2, for the entire OMI mission (2004-present). Furthermore, I included the averaging kernel, temperature and a priori NO<sub>2</sub> profiles in the DOMINO product which provides critical data to enable users to test improvements



to the retrieval algorithm themselves.

The accuracy of the retrieval of tropospheric NO<sub>2</sub> from space relies on the knowledge of the state of the atmosphere at the moment of observation, where the primary source of error for the retrieval of tropospheric NO<sub>2</sub> from satellite measurements is the tropospheric air mass factor. *Boersma et al.* [2004] identified uncertainties in the a priori profile, cloud parameters, and the surface albedo as the major contributors to the error in the tropospheric air mass factor. In the last part of this chapter improvements to the DOMINO algorithm are discussed based on the findings of several validation studies involving DOMINO data.

### 3.2 Satellite retrieval of tropospheric NO<sub>2</sub>

Since the launch of GOME in 1995 considerable effort has been invested in the development of algorithms to retrieve tropospheric NO<sub>2</sub> from spaceborne nadir observations, which resulted in the parallel development of retrieval algorithms by various research groups [*Leue et al.*, 2001, *Richter and Burrows*, 2002, *Martin et al.*, 2002a, *Boersma et al.*, 2004]. These algorithms share a common 3-step approach to retrieve tropospheric NO<sub>2</sub>, which is also followed by the DOMINO algorithm. In the first step NO<sub>2</sub> slant columns are determined by a spectral fit to the Earth reflectance spectrum by means of the DOAS method [*Platt and Stutz*, 2008]. The second step involves estimating the stratospheric contribution to the slant column, and in the final step the tropospheric slant column is converted into a vertical column by the tropospheric air mass factor. Different wavelength regions and spectroscopic data are used in the spectral fitting procedure, resulting in differences of approximately 5% in the retrieved slant columns [*Boersma et al.*, 2004]. Larger differences occur in the determination of the stratospheric contribution to the observed slant column, where several retrievals rely on the inadequate assumption that the stratospheric NO<sub>2</sub> field has small variation in the zonal direction. Examples of this are the reference sector method [*Martin et al.*, 2002a], and the wave-2 filtering of satellite data employed by *Bucsela et al.* [2006], *Celarier et al.* [2008]. *Richter et al.* [2005] use daily stratospheric NO<sub>2</sub> columns from simulations of the SLIMCAT CTM [*Chipperfield*, 1999] in the retrieval of tropospheric NO<sub>2</sub> from SCIAMACHY. Recently, a new approach has been proposed to retrieve stratospheric NO<sub>2</sub> from SCIAMACHY limb measurements [*Beirle et al.*, 2010]. The SCIAMACHY limb measurements show considerable longitudinal variation in the retrieved stratospheric NO<sub>2</sub> field, but further development of this approach is necessary as the limb retrievals overestimate the stratospheric NO<sub>2</sub>, resulting in negative tropospheric NO<sub>2</sub> columns over unpolluted regions. The DOMINO algorithm estimates the stratospheric slant column from the modeled NO<sub>2</sub> field that is based on the assimilation of OMI data in the TM4 chemistry transport model (CTM).

The calculation of the tropospheric air mass factor is another step where retrieval algorithms differ, and various approaches exist to estimate the critical parameters for the tropospheric air mass factor, such as clouds, surface albedo, NO<sub>2</sub> and temperature profile, and aerosol. The estimated contribution of clouds to the precision of the tropospheric column is 15-30% in polluted areas [Martin *et al.*, 2002a, Boersma *et al.*, 2004], whereas uncertainties in the surface albedo account for a 15-35% error in polluted areas [Martin *et al.*, 2002a, Boersma *et al.*, 2004], and the estimated error due to the profile shape is less than 15% [Martin *et al.*, 2002a, Boersma *et al.*, 2004]. Tropospheric NO<sub>2</sub> profiles are derived from CTM simulations, using either daily updates [Martin *et al.*, 2002a, Boersma *et al.*, 2007] or monthly [Richter *et al.*, 2005] and annual [Bucsela *et al.*, 2006] averages. Cloud parameters generally are retrieved from the observed radiance spectrum, using e.g., the FRESCO [Koelemeijer *et al.*, 2001] or the OMI O<sub>2</sub>-O<sub>2</sub> [Acarreta *et al.*, 2004] algorithm. Clouds are typically accounted for in the evaluation of the air mass factor, except for Richter *et al.* [2005] who discard scenes with cloud fractions exceeding 0.2. Surface reflectivities used in the retrievals are derived from GOME [Koelemeijer *et al.*, 2003], TOMS [Herman and Celarier, 1997] or OMI [Kleipool *et al.*, 2008].

### 3.2.1 OMI data streams

OMI data are distributed in two parallel streams: the regular production data stream that is available 1-2 days after measurement (hereafter called the offline data-stream), and the near-real time data stream that is already available within 3-4 hours after measurement. NRT data are downlinked once per orbit to one of the ground stations (Alaska, Svalbard, or Wallops Island) and are made available with the highest priority at the expense of data integrity. The NRT stream is processed with predicted altitude and ephemeris data, which can cause errors in the geolocation parameters, although in practice these errors appear to be small. Occasionally, it occurs that a NRT orbit is delayed or missing. The offline data stream is processed with definitive altitude and ephemeris data, and constitutes a contiguous data set without missing orbits. The DOMINO system treats the two data-streams differently, as will be discussed in Section 3.2.3.1.

### 3.2.2 OMI slant column retrieval

NO<sub>2</sub> slant columns are retrieved with the DOAS (Differential Optical Absorption Spectroscopy [Platt and Stutz, 2008]) method, by fitting a modeled spectrum to the OMI-observed Earth reflectance spectrum between 405-465 nm. This wide fitting window, as compared to GOME and SCIAMACHY (425-450 nm), was chosen to compensate for OMI's lower signal to noise (1400). The modeled spectrum accounts

for spectral structures resulting from absorption by NO<sub>2</sub>, O<sub>3</sub>, and water vapor, and for a slowly varying background to account for broadband features introduced by molecular (Rayleigh) and Mie (aerosol) scattering and absorption. The high-resolution NO<sub>2</sub> cross section spectrum for 220 K is taken from *Vandaele et al.* [1998], the ozone spectrum is taken from *Bass and Johnston* [1975], and the water vapor spectrum is taken from [*Coheur et al.*, 2002, *Fally et al.*, 2003]. The cross section spectra of O<sub>3</sub>, NO<sub>2</sub>, and water vapor are converted to OMI's spectral resolution by convolution with the OMI spectral slitfunction [*Dirksen et al.*, 2006] that is described in Chapter 2 of this thesis.

The modeled spectrum is described by a modified Lambert-Beer law:

$$\ln[R(\lambda)] = - \sum_i \sigma_i(\lambda) \cdot N_{s,i} - P_3(\lambda) \quad (3.1)$$

With  $R(\lambda)$  the modeled reflectance spectrum,  $\sigma_i$  the wavelength dependent absorption cross section of species  $i$ ,  $N_{s,i}$  the number of molecules of species  $i$  in the observed slant column, and  $P_3(\lambda)$  a 3rd order polynomial that describes the spectrally smooth background resulting from multiple scattering, absorption and surface albedo. Based on measurement data the estimated accuracy of OMI NO<sub>2</sub> slant columns is  $0.7 \times 10^{15}$  molecules/cm<sup>2</sup> [*Boersma et al.*, 2007]. Earth reflectance spectra follow from dividing the Earth radiance measurements by the OMI-measured solar irradiance. Because of signal-to-noise considerations a fixed solar irradiance spectrum has been constructed from daily irradiance measurements taken in 2005 (see the OMI NO<sub>2</sub> README file [http://www.knmi.nl/omi/research/product/NO2/OMNO2\\_readme\\_2009-02.pdf](http://www.knmi.nl/omi/research/product/NO2/OMNO2_readme_2009-02.pdf)). The slant NO<sub>2</sub> columns are retrieved assuming a fixed atmospheric temperature of 220 K, however not accounting for the temperature sensitivity of the NO<sub>2</sub> absorption cross section spectrum can result in underestimating the tropospheric slant column by 20% in polluted areas because of warmer NO<sub>2</sub> in the boundary layer [*Boersma et al.*, 2004]. In the DOMINO retrieval, the temperature sensitivity of the NO<sub>2</sub> cross section spectrum is accounted for by the tropospheric air mass factor as will be discussed in Section 3.2.4.

### 3.2.3 Stratosphere-troposphere separation

Separation between the troposphere and the stratosphere is achieved by assimilating OMI NO<sub>2</sub> slant columns in the TM4 chemical transport model (CTM), and by subsequently subtracting the forecast stratospheric slant column from the observed slant column. TM4 [*Dentener et al.*, 2003] operates at a 3°x2° (longitude x latitude) spatial resolution and with 35 layers in the vertical direction, extending up to 0.38 hPa. TM4 is driven by forecast and analyzed meteorological fields from the European Centre for Medium Range Weather Forecast (ECMWF). A detailed overview of the

processing of the meteorological input by TM4, and of the chemical schemes applied by TM4 is given in Chapter 4.

In the assimilation approach, the forecast TM4 model state is updated using OMI NO<sub>2</sub> observations, yielding the analyzed model state (analysis). The model forcing, which is based on the Kalman filter technique, attributes less weight to measurements over (known) polluted areas so that tropospheric sources do not contribute to the modeled stratospheric NO<sub>2</sub> field. In Chapter 4 a more detailed description of the assimilation approach is given.

The advantage of the assimilation approach employed by DOMINO, is that due to the application of current meteorological data by TM4, the modeled 3-D stratospheric NO<sub>2</sub> field contains synoptic-scale structures that result from variations in temperature and wind fields. This is an improvement with respect to retrieval algorithms that assume a zonally smooth NO<sub>2</sub> distribution in the stratosphere. In Chapter 4 I will demonstrate that over areas with high dynamic variability the error in the estimated stratospheric NO<sub>2</sub> column can be as large as  $1 \times 10^{15}$  molecules/cm<sup>2</sup> when a smooth stratospheric NO<sub>2</sub> field is assumed instead, whereas the DOMINO algorithm is able to capture these variations in the stratospheric NO<sub>2</sub> field.

Based on a statistical analysis of the difference between observation and forecast, the uncertainty in the stratospheric slant column is estimated at  $0.2 \times 10^{15}$  molecules/cm<sup>2</sup> [Boersma *et al.*, 2007], which is considerably smaller than the error in the observed slant column.

*3.2.3.1 Data assimilation for NRT and offline stream* The DOMINO system processes all offline OMI data of an entire day in a single TM4 assimilation run, using analyzed meteorological fields as input. The offline processing is performed two days after the orbits were measured, when all offline OMI data are available. The DOMINO offline data are added to the publicly accessible archive at <http://www.temis.nl/>.

Because of time considerations, a different set up was chosen for the NRT stream. The DOMINO NRT retrieval consists of two sub-systems, as indicated in Figure 3.1. The first is the TM4 forecast subsystem that runs once per day (at midnight UTC), and the second is the NRT subsystem that is executed each time a new OMI NRT orbit arrives at KNMI. The forecast subsystem (top panel in Figure 3.1) updates the analysis and forecast starting from the analysis of the previous day. In the forecast run, TM4 runs forward in time with the forecast ECWMF meteorological data and the assimilation of all available OMI NO<sub>2</sub> measurements of the past days. The updated analysis is stored as input for the subsequent run of the forecast system. As indicated in Figure 3.1, the forecast stratospheric slant column, tropospheric NO<sub>2</sub> profile, surface pressure and temperature profile, which are needed to retrieve the tropospheric NO<sub>2</sub> column are passed on to the NRT subsystem (bottom panel in Figure 3.1). The NRT subsystem subtracts the forecast stratospheric NO<sub>2</sub> from the OMI observed slant column and converts the remaining tropospheric slant column

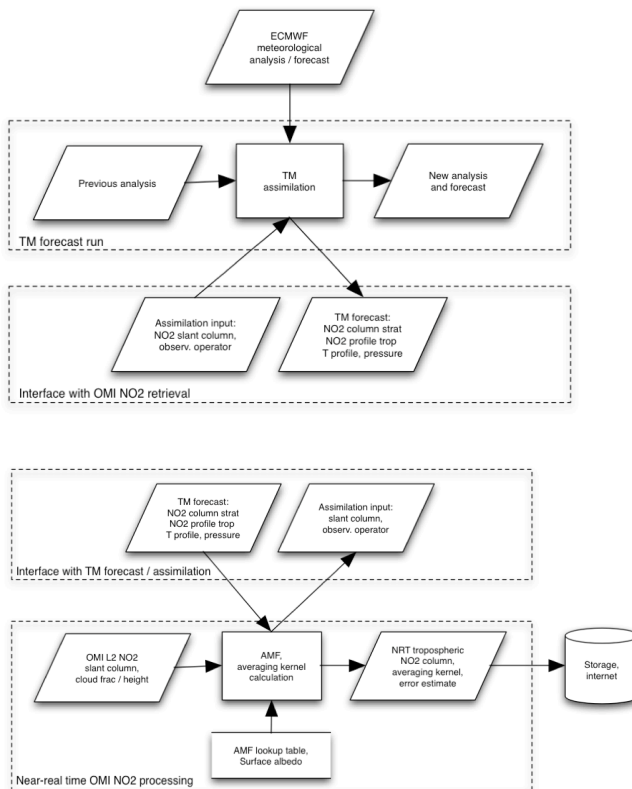


**Figure 3.1** Flowchart for the DOMINO retrieval-assimilation system, the lower part of the forecast / assimilation subsystem (top) interfaces with the top part of the NRT subsystem (bottom). Figure adopted from Boersma et al. [2007].

into a vertical column using the tropospheric air mass factor that is further discussed in Section 3.2.4.

The execution of the forecast subsystem takes approximately 2 hours to complete using 8 parallel threads on a SGI altix 3000 mainframe, this involves calculating the forecast for two days in advance, which makes the system more robust to interruptions in the input data. The processing of an OMI orbit by the NRT subsystem (calculation and application of the tropospheric air mass factor) is accomplished in less than 2 minutes on the same computer system.

## 3.2.4 Tropospheric air mass factor

The tropospheric slant columns are converted into vertical columns by dividing by the tropospheric air mass factor  $\text{AMF}_{\text{trop}}$ , that accounts for the average light path traversed by the photons that enter OMI.

$$\text{VCD}_{\text{trop}} = \text{SCD}_{\text{trop}} / \text{AMF}_{\text{trop}} \quad (3.2)$$

$\text{AMF}_{\text{trop}}$  is described by a forward model that includes model parameters  $\hat{\mathbf{b}}$  such as viewing geometry, the absorber's vertical profile shape, terrain height, surface albedo, cloud fraction and cloud pressure, and (multiple) Rayleigh scattering. For optically thin absorbers like NO<sub>2</sub>, the altitude dependence of the measurement sensitivity can be decoupled from the actual profile shape so that the air mass factor can be written as [Palmer *et al.*, 2001, Eskes and Boersma, 2003]:

$$\text{AMF}_{\text{trop}} = \frac{\sum_l m_l(\hat{\mathbf{b}}) x_{a,l} c_l}{\sum_l x_{a,l}} \quad (3.3)$$

Here  $l$  denotes the atmospheric layer,  $m_l$  represents the air mass factor for layer  $l$ ,  $x_a$  represents the a priori NO<sub>2</sub> profile, and  $c_l$  is a layer-specific correction term that accounts for the temperature dependence of the absorption cross section spectrum.

The a priori NO<sub>2</sub> profile  $x_a$  is taken from the TM4 model field, where the 3°x2° modeled profiles are sampled at the model time closest to the OMI overpass, and interpolated to the footprint of the OMI pixels. The temperature profile that is needed to calculate the temperature dependent correction to the absorption cross section ( $c_l$  in Equation 3.3) is derived from the ECMWF meteorological input. The air mass factors  $m_l$  were pre-calculated with the pseudo-spherical DAK radiative transfer model [de Haan *et al.*, 1987, Stammes, 2001] that includes polarization [Stammes *et al.*, 1989], and stored in a multi-dimensional look-up table to reduce computational effort.

$\text{AMF}_{\text{trop}}$  accounts for the vertical sensitivity of OMI for NO<sub>2</sub>, which decreases towards the surface due to enhanced scatter in the increasingly dense lower troposphere and the low surface albedo for snow-free scenes (typically 5% at 440 nm). Clouds increase the effective albedo of the scene, thereby increasing OMI's sensitivity to NO<sub>2</sub> above it. On the other hand, OMI is insensitive for below-cloud NO<sub>2</sub>, yielding a lower  $\text{AMF}_{\text{trop}}$  for cloudy scenes because the air mass factors  $m_l$  in Equation 3.3 below the cloud level are zero. As a result, a ghost column is added to the retrieved NO<sub>2</sub> column to compensate for below cloud NO<sub>2</sub> [Burrows *et al.*, 1999], where the ghost column is derived from the a priori profile below the cloud.

The air mass factor for a partly clouded scene is determined with the independent pixel approximation [Boersma *et al.*, 2004], where the effective air mass factor is a combination of the air mass factor for a cloudy and a cloud-free scene. For increasing

cloud fractions the tropospheric NO<sub>2</sub> column becomes unreliable, because of the growing contribution of the modeled ghost column to the retrieved tropospheric column. Therefore, it is good practice to ignore tropospheric NO<sub>2</sub> columns for pixels where the cloud radiance fraction exceeds 0.5 (this corresponds to a cloud fraction of approximately 0.2).

The cloud parameters used by DOMINO are retrieved from OMI's VIS channel by a DOAS fit to the O<sub>2</sub>-O<sub>2</sub> absorption feature at 477nm [Acarreta *et al.*, 2004]. The effective cloud fraction is determined from the continuum reflectance of the scene, and the O<sub>2</sub>-O<sub>2</sub> slant column, together with the viewing and solar geometry, is used to find the effective scattering pressure by means of a lookup table. The lookup table was produced using DAK with clouds approximated as Lambertian reflectors with albedo 0.8. OMI O<sub>2</sub>-O<sub>2</sub> cloud fractions have been validated successfully against MODIS-Aqua cloud observations [Stammes *et al.*, 2008], and OMI cloud pressures were generally within 100 hPa of PARASOL cloud pressures.

Until February 2009 the surface albedo was taken from 1°x1.25° climatological monthly mean maps based on combined TOMS and GOME Lambert-equivalent reflectivity (LER) measurements [Koelemeijer *et al.*, 2003, Boersma *et al.*, 2004]. After this date the newly available OMI-derived albedo database with improved spatial resolution (0.5°x0.5° Kleipool *et al.* [2008]) is used in the processing. Due to OMI's smaller ground pixels as compared to GOME, the new albedo data base is less sensitive to cloud contamination. Furthermore, the OMI-based albedo climatology represents the surface albedo at approximately 13h40 local time, which is consistent with the OMI observations.

The DOMINO data product version 1.0.2. is available for the entire OMI mission (October 2004-present) at <http://www.temis.nl>, the product description document can be found at [http://www.temis.nl/docs/OMI\\_NO2\\_HE5\\_1.0.2.pdf](http://www.temis.nl/docs/OMI_NO2_HE5_1.0.2.pdf).

### 3.2.5 Features of the DOMINO product

The DOMINO algorithm and data product version 1.0.2 incorporate the following features:

**Averaging kernels** For every pixel the corresponding averaging kernel vector for each model layer  $l$  is provided. The averaging kernel represents the height-dependent sensitivity of OMI to NO<sub>2</sub>, and is essential when comparing DOMINO columns to independent data such as model output, observed profiles or columns, whose (a priori) profile shapes differ from the TM4 a priori profile [Eskes and Boersma, 2003]. The DOMINO averaging kernel has been used several studies [e.g., Mijling *et al.* [2009], Huijnen *et al.* [2010], Lamsal *et al.* [2010], Herron-Thorpe *et al.* [2010]]. More information on the use of the averaging kernel is given in the DOMINO product description ([http://www.temis.nl/docs/OMI\\_NO2\\_HE5\\_1.0.2.pdf](http://www.temis.nl/docs/OMI_NO2_HE5_1.0.2.pdf)).

**Error estimates** The DOMINO data product includes for each pixel a realistic tropospheric column error based on errors in the DOAS spectral fit, cloud algorithm, the albedo map, the profile shape, and the estimate of the stratospheric column [Boersma *et al.*, 2004].

**NO<sub>2</sub> profile shape** DOMINO obtains daily updated a priori profile shapes from TM4, which explicitly models the effect of emissions, chemistry and meteorological conditions (wind, convection, deposition) on the vertical distribution of NO<sub>2</sub>. As a unique feature of the DOMINO data product, the TM4 profiles for each pixel are provided, which, together with the temperature profile, allows users to perform their own tropospheric air mass factor calculations.

**Stratospheric column** The meteorological state of the atmosphere causes the stratospheric column to vary in space and time. This variability is accounted for by the transport model TM4. Data assimilation is used to make the model stratosphere consistent with the OMI observations. In Chapter 4 I will show that the assimilated stratospheric NO<sub>2</sub> column is a useful product in itself.

**Temperature profiles** The temperature dependence of the cross section of NO<sub>2</sub> is accounted for based on the daily updated temperature profiles of the ECMWF meteorological analyses. Furthermore, the DOMINO product provides the users an interpolated temperature profile for each OMI pixel.

### 3.3 OMI data collection 3

The OMI data collections (versions) 1 and 2 were affected by inadequate calibration of the dark current of the CCD detector and by the limited signal-to-noise of the daily solar irradiance measurements. This caused systematic biases (upwards and downward) of NO<sub>2</sub> slant columns at specific viewing angles, that show up as stripes along the orbit [Boersma *et al.*, 2007]. This striping is not limited to NO<sub>2</sub> but affects nearly all OMI data products, each having another striping pattern owing to the different fitting windows of the products. For DOMINO version 0.8 a de-striping algorithm was developed, based on high pass filtering of observations over the remote (unpolluted) areas to characterize the high frequency features [Boersma *et al.*, 2007].

For OMI data collection 3 an improved calibration approach was implemented; a better correction of the CCD detector's dark current significantly reduced these stripes [Dobber *et al.*, 2008]. Simultaneously, the signal to noise of the irradiance spectrum was improved by replacing the daily solar irradiance spectra with the yearly averaged spectrum for 2005. The re-processing of level 1b data for collection 3 was started in 2007, and after a major reprocessing operation in the first half of 2008 the entire OMI mission is available as DOMINO collection 3, version 1.0.2. The DOMINO system typically processes one month of OMI data in 24 hours, so that the entire reprocessing of collection 3 lasted approximately 2 months.



In the processing of collection 3 the de-stripping algorithm was deactivated because the amplitude of the stripes was considerably reduced due to the new calibration approach, and because the de-stripping algorithm introduced offsets at the swath edges. An improved de-stripping algorithm is being developed and will be applied in a future reprocessing of the OMI data set.

Since June 2007 OMI is plagued by the so-called row anomaly effect. The exact cause of the effect is not known, but the available evidence suggests a partial blocking of OMI's nadir port by the isolation blanket in which the instrument is wrapped. This leads to a severe reduction of the radiance signal for the affected viewing angles and to sunlight being reflected into the nadir port. Furthermore, inhomogeneous illumination of the spectrograph's entrance slit affects the shape of the slitfunction resulting a shift of the recorded spectrum.

As shown in Table 3.1 the number of rows affected by the anomaly has increased step-wise, and the current status is that a considerable part of the OMI field of view near the center of the swath is affected. Considerable effort has been invested in investigating the row anomaly and in developing corrections for its effect on the radiance and spectral calibration, which will be implemented in the upcoming OMI data collection 4. Due to its spectral effect, the row anomaly affects DOAS-based products, including the retrieval of NO<sub>2</sub> slant columns and cloud parameters, which both are essential for the DOMINO algorithm. Therefore, it is recommended to avoid using the rows affected by the row anomaly. Nevertheless, even when discarding the rows listed in Table 3.1, the daily OMI observations still cover more than 70% of the Earth's atmosphere. More information on the OMI row anomaly and on the development of corrections can be found at [http://www.temis.nl/docs/omi\\_warning.html](http://www.temis.nl/docs/omi_warning.html).

**Table 3.1** *Evolution of the OMI row anomaly*

Label	Since	Affected rows (0-based)
Anomaly 1	25 June 2007	53-54
Anomaly 2	11 May 2008	37-44
Anomaly 3	24 January 2009	27-44

### 3.4 OMI standard product

Parallel to the DOMINO algorithm, the GSFC-developed Standard Product (SP) algorithm retrieves tropospheric NO<sub>2</sub> from OMI measurements on an operational basis. The DOMINO and the Standard Product algorithms have the same starting point, the DOAS-retrieved slant columns, but they differ with regard to the stratosphere-troposphere separation, the calculation of the tropospheric air mass factor and assumed reflectivities. The properties of the DOMINO and the Standard

Product NO<sub>2</sub> algorithms are compared in Table 3.2. The Standard Product identifies the stratospheric NO<sub>2</sub> columns as the slowly varying part of the total column NO<sub>2</sub> field, which implies that medium-scale variations in the observed NO<sub>2</sub> field of up to several 100 km in size are attributed to tropospheric signals [Bucsela *et al.*, 2006, Celarier *et al.*, 2008]. NO<sub>2</sub> slant columns are converted into initial vertical columns (VCD<sub>init,SP</sub>) by applying an (unpolluted) air mass factor (AMF<sub>init,SP</sub>). AMF<sub>init,SP</sub> is derived with TOMRAD [Dave, 1965] radiative transfer calculations using annually averaged simulated NO<sub>2</sub> profiles that are constructed from merging stratospheric profiles from GSFC CTM [Douglass *et al.*, 2003] with tropospheric profiles from GEOS-Chem [Martin *et al.*, 2002b]. The Standard Product applies a second order Fourier (wave-2) fit in 1°-wide latitude bands in the zonal direction to all data collected within ±12 hours of the target orbit [Bucsela *et al.*, 2008]. Prior to the wave-2 fit, regions with known high tropospheric NO<sub>2</sub> abundances (identified using GEOS-Chem) are masked and a 9°-wide boxcar running average is applied in the meridional direction. Areas with strong deviations from the wave-2 fit are identified as contaminated by tropospheric NO<sub>2</sub> pollution and also masked. Then, the wave-2 fit is performed for the second time to produce the stratospheric NO<sub>2</sub> field.

**Table 3.2** Overview of the OMI DOMINO and OMI Standard Product NO<sub>2</sub> algorithms.

Parameter	DOMINO	Standard Product
Slant column	DOAS (405-465 nm)	DOAS (405-465 nm)
Stratospheric column	Data assimilation in TM4 (3°x2°)	wave-2 fit in zonal band
Tropospheric a priori profile	Daily updates from TM4 (3°x2°)	Annual mean from GEOS-Chem (2.5°x2°) <sup>a</sup>
Temperature profile	ECMWF analysis and forecast (3°x2°)	Monthly mean from NCEP
Radiative transfer model	DAK	TOMRAD
Clouds	OMI O <sub>2</sub> -O <sub>2</sub> <sup>b</sup>	OMI O <sub>2</sub> -O <sub>2</sub> <sup>b</sup>
Surface albedo	TOMS-GOME & OMI <sup>c</sup>	GOME
Stripe correction	–	based on 24-h data <sup>d</sup>
Ghostcolumn	Implicit in AMF <sub>trop</sub>	–

<sup>a</sup> Applied when retrieved slant column exceeds stratospheric slant column.

<sup>b</sup> Acarreta *et al.* [2004]

<sup>c</sup> TOMS/GOME based on combining Herman *et al.* [1997] and Koелеmeijer *et al.* [2003] as described in Boersma *et al.* [2004]. After Februari 2009 the OMI-derived surface albedo by Kleipool *et al.* [2008] is used.

<sup>d</sup> See Bucsela *et al.* [2008].

Pixels where VCD<sub>init,SP</sub> exceeds the stratospheric column are marked polluted and the tropospheric air mass factor is applied to retrieve the tropospheric NO<sub>2</sub> column. The a priori profile used in the tropospheric air mass factor calculation is taken from a geographically gridded set of annually averaged tropospheric NO<sub>2</sub> profiles from

GEOS-Chem simulations. Temperature profiles are derived from monthly mean values of the NCEP climatology [Kalnay *et al.*, 1996], cloud parameters are taken from the OMI O<sub>2</sub>-O<sub>2</sub> algorithm [Acarreta *et al.*, 2004], and the surface reflectivity is given by the GOME albedo climatology at 440 nm [Koelemeijer *et al.*, 2003]. The tropospheric air mass factor for the standard product is calculated with the TOMRAD [Dave, 1965] radiative transfer model. For cloudy scenes, the below-cloud amount (ghostcolumn) is derived by scaling the polluted NO<sub>2</sub> profile to the retrieved tropospheric NO<sub>2</sub> column and is stored in a separate data field which can be added to the tropospheric column at the users discretion [Celarier *et al.* [2008] and OMI NO<sub>2</sub> README file at [http://www.knmi.nl/omi/research/product/NO2/OMNO2\\_readme\\_2009-02.pdf](http://www.knmi.nl/omi/research/product/NO2/OMNO2_readme_2009-02.pdf)].

### 3.5 Illustration of DOMINO tropospheric NO<sub>2</sub> monitoring capabilities

In August 2007 Greece suffered from severe forest fires on the Peloponnesus and in the area near its capital, Athens. Although forest fires are common in the Mediterranean region, the 2007 burning events were exceptionally intense due to favorable conditions such as heat waves, extended droughts and strong winds. Provisional data indicate that more than 1700 km<sup>2</sup> was burned [Turquety *et al.*, 2009], with an estimated emission of 8.8x10<sup>9</sup>g NO<sub>2</sub> between 21-28 August 2007, according to the 8-day average GFED-2 database. GFED emission estimates are based on a combination of burned area and the vegetation index [van der Werf *et al.*, 2006]. As shown in Figure 3.2, OMI detects increased tropospheric NO<sub>2</sub> columns caused by emissions by the fires, and due to OMI's high spatial resolution the fire locations are clearly distinguishable from the regular urban pollution sources in the region around Athens. The daily OMI observations show how the fire emissions gradually intensify between 23-25 August, to reach their full strength on 26 August. Owing to the strong north easterly winds that fanned the fires, on 25 and 26 August the NO<sub>2</sub> plumes extend as far as the coast of north Africa.

These daily observations of the 2007 Greek forest fires clearly demonstrate OMI's capability to monitor variable emission sources. This fire event is a good model case for a top-down estimate of NO<sub>x</sub> emissions from OMI observations, as the event occurred under cloud-free conditions and the fires are well-separated from other pollution sources in the region. Furthermore, the effect of forest fire aerosols on the DOMINO retrieval of tropospheric NO<sub>2</sub> can be investigated, where observations from the spaceborne lidar CALIOP, MODIS and OMI are used to characterize (altitude, optical depth and single scattering albedo) of the aerosols emitted by the fires.

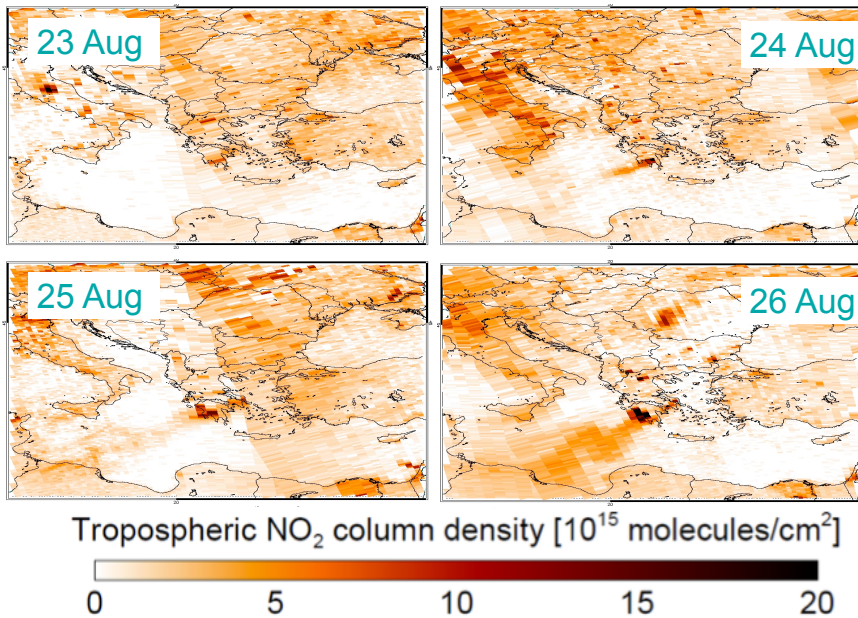


**Figure 3.2** Time series of DOMINO observations of tropospheric  $\text{NO}_2$  emitted by the forest fires that raged in Greece in August 2007. Image was part of a KNMI press-release about the Greek forest fires ([http://www.knmi.nl/cms/content/16029/nederlands\\_satellietinstrument\\_omi\\_volgt\\_griekse\\_rook](http://www.knmi.nl/cms/content/16029/nederlands_satellietinstrument_omi_volgt_griekse_rook)).

### 3.6 Recommendations from validation studies

During the ongoing OMI mission several validation campaigns have been organized to compare OMI tropospheric  $\text{NO}_2$  observations to independent measurements by ground-based and airborne instruments. In the following I present an overview of the findings of the DANDELIONS and INTEX-B validation campaigns, together with the results of separate validation and sensitivity studies that all involved tropospheric  $\text{NO}_2$  columns from the DOMINO version 1.0.2 data set. The conclusions of these studies are used for improvements of the DOMINO retrieval algorithm that are discussed by *Boersma et al.* (to be published).

DANDELIONS 2006 (Dutch Aerosol and Nitrogen Dioxide Experiments for Validation of OMI and SCIAMACHY) took place in September 2006 at the Cabauw measurement site in The Netherlands [*Brinksma et al.*, 2008], during which column and profile observations of tropospheric  $\text{NO}_2$  were performed with various ground-based instruments. Total columns of tropospheric  $\text{NO}_2$  were measured with MAX-DOAS instruments from different research groups [*Wagner et al.*, 2004, *Wittrock et al.*, 2004, *Pinardi et al.*, 2008], while the RIVM  $\text{NO}_2$  lidar [*Volten et al.*, 2009] and

in-situ observations with molybdenum oxide converters [Volten *et al.*, 2009] provided information on the vertical profile of NO<sub>2</sub> in the troposphere. Cabauw (51.97°N, 4.92°E) is a suburban site located in the vicinity of major pollution sources such as the industrialized Rotterdam port area (30 km to the west) the Ruhr area (100 km to the East), as well as the traffic of busy nearby highways in the Netherlands.

The INTEX-B (Intercontinental Chemical Transport Experiment) campaign [Singh *et al.*, 2009] comprises a series of airplane flights with the NASA DC-8 research aircraft in March 2006 over the Gulf of Mexico, Mexico City, the southeastern United States, and the Pacific. During INTEX-B vertical profiles of NO<sub>2</sub> were obtained under a range of conditions, including flights over source and outflow regions, as well as over remote areas. The profiles were measured between 300 m and 12 km altitude with a laser induced fluorescence instrument [Thornton *et al.*, 2000].

Other studies discussed here involve the comparison of DOMINO tropospheric NO<sub>2</sub> columns with model output [Huijnen *et al.*, 2010], with ground-based in situ measurements in the rural southeastern USA [Lamsal *et al.*, 2010], and an analysis of the sensitivity of the DOMINO retrieval to orography [Zhou *et al.*, 2009] and the anisotropy of the surface albedo [Zhou *et al.*, 2010].

### 3.6.1 Results

Table 3.3 lists the studies in which DOMINO tropospheric NO<sub>2</sub> columns, version 1.0.2, were compared to independent measurements, or where retrieval improvements were investigated. In the following I will briefly summarize the results each study and its consequent recommendation for improving the DOMINO retrieval of tropospheric NO<sub>2</sub>.

Volten *et al.* [2009] found that under polluted conditions DOMINO tropospheric NO<sub>2</sub> columns systematically exceed the lidar columns. Further investigation of this effect was performed by Hains *et al.*, [2010], who evaluated DOMINO NO<sub>2</sub> with measurements from the DANDELIONS and INTEX-B campaigns. The ensemble of tropospheric NO<sub>2</sub> columns derived from the MAXDOAS, lidar, in-situ and aircraft measurements show good agreement with the DOMINO columns ( $r > 0.74$ , without significant bias). On average the TM4 a priori profiles agree reasonably well with observations, but for a suburban site like Cabauw that is surrounded by several sources of NO<sub>x</sub>, the lidar profile constitutes a point measurement that is difficult to reproduce by TM4, which operates at 3°x2° spatial resolution. Additionally, the lidar measurements indicate that the vertical mixing of NO<sub>2</sub> by TM4 is too weak in the boundary layer. The study by Hains *et al.* [2010] shows that when the a priori profiles are replaced by observed profiles in the calculation of AMF<sub>trop</sub>, the DOMINO NO<sub>2</sub> columns change on average by 15%. Replacing the surface albedo by the OMI-derived albedo from Kleipool *et al.* [2008], changes the retrieved NO<sub>2</sub> columns by up to 13%, with the strongest effect in polluted situations over dark

**Table 3.3** Overview of validation and modeling studies involving DOMINO.

Study	Reference	Result
DOMINO, TM4 and various (regional) air quality models.	<i>Huijnen et al.</i> [2010]	Insufficient mixing by TM4 of NO <sub>2</sub> in the boundary layer. DOMINO overestimates model ensemble column factor 2 in summer, good agreement in winter.
NO <sub>2</sub> lidar (DANDELIONS 2006).	<i>Volten et al.</i> [2009]	DOMINO columns exceed lidar columns by approximately 50%.
DOMINO versus lidar, MAX-DOAS, in-situ surface and aircraft (DANDELIONS 2006 & INTEX-B).	<i>Hains et al.</i> [2010]	NO <sub>2</sub> columns agree well. Replacement of TM4 profile and surface albedo improves agreement with validation data by 23%.
DOMINO versus in-situ surface measurements.	<i>Lamsal et al.</i> [2010]	Replacing TM4 profiles by GEOS-Chem profiles reduces bias with surface observations to 5%.
Orography and representativity error in effective pixel height.	<i>Zhou et al.</i> [2009]	Coarse (3°x2°) TM4 resolution causes modeled column errors up to 5-15%.
Anisotropy of surface reflectivity.	<i>Zhou et al.</i> [2010]	Column errors up to 20% for extreme viewing geometries.

terrain. The combined effect of replacing profile and albedo results in an average change of 23% in the retrieved column, while the agreement with the validation measurements improves. This underlines the conclusions of *Boersma et al.* [2004] that uncertainties in the a priori profile and the surface albedo are major error sources for the tropospheric air mass factor. The importance of the surface albedo is further illustrated by the study of *Zhou et al.* [2010] who show that ignoring the anisotropy (viewing angle dependence) of the surface albedo can result in an error of up to 20% in the retrieved NO<sub>2</sub> columns.

*Lamsal et al.* [2010] compared DOMINO NO<sub>2</sub> columns to surface in-situ observations with photolytic converter analyzers for rural sites in the southeastern USA. Photolytic converter analyzers [*Ryerson et al.*, 2000] are specific to NO<sub>x</sub> and do not detect NO<sub>y</sub> that commonly interferes with measurements by molybdenum based detectors in photochemically aged air [*Steinbacher et al.*, 2007]. In comparison with the surface measurements, DOMINO NO<sub>2</sub> columns are high biased by 21%, with some seasonal dependence. This high-bias is related to the aforementioned insufficient mixing of TM4 NO<sub>2</sub> profiles in the boundary layer [*Huijnen et al.*, 2010]: when the NO<sub>2</sub> columns are adjusted using (well-mixed) GEOS-Chem profiles together with the averaging kernel, the average high-bias reduces to 5%, and the size of

the adjustment to the NO<sub>2</sub> column as a result of replacing the a priori profile is comparable to the changes found in the DANDELIONS campaign. Since *Lamsal et al.* [2010] use simulated profiles from GEOS-Chem to convert DOMINO NO<sub>2</sub> columns into NO<sub>2</sub> surface mixing ratios, the comparison with surface measurements constitutes an indirect validation of the DOMINO NO<sub>2</sub> columns.

*Huijnen et al.* [2010] compared DOMINO NO<sub>2</sub> to the output of an ensemble of global and regional air quality models over Europe, which showed a good spatial correlation between the models and DOMINO NO<sub>2</sub>. In winter there is good agreement between DOMINO and the models, but in summer DOMINO NO<sub>2</sub> columns are almost twice as high as the modeled NO<sub>2</sub> columns. This discrepancy in summer between OMI and modeled NO<sub>2</sub> columns can partly be explained by missing emission sources from biomass burning and lightning in the regional air quality models, but it is also linked to TM4's insufficient vertical mixing of NO<sub>2</sub> in the boundary layer which causes a higher surface NO<sub>2</sub> concentration in comparison with other models. However, in winter the modeled NO<sub>2</sub> profile shapes are more similar to that of TM4. As indicated by *Huijnen et al.* [2010], the insufficient mixing of boundary layer NO<sub>2</sub> by TM4 is not caused by a faulty mixing scheme but rather the consequence of sampling the tracer NO<sub>2</sub> field after the emission step but before the advection and convection steps are applied.

*Zhou et al.* [2009] investigated the effect of representativity errors in the surface pressure of OMI pixels in mountainous regions (making use of the DOMINO-provided TM4 NO<sub>2</sub> profiles). Due to TM4's coarse spatial resolution (3°x2°) differences between the modeled and effective terrain height introduce errors in the surface pressure of OMI pixels. This leads to a vertical shift of the lower part of the NO<sub>2</sub> profile, affecting the tropospheric air mass factor. Consequently, NO<sub>2</sub> over elevated areas with too low modeled altitude is overestimated, while NO<sub>2</sub> in valleys with too high modeled altitude is underestimated. In the polluted Po valley in the foothills of the Alps the altitude mismatch can be as much as 700 m, and when the TM4 profiles are replaced by improved profiles based on high resolution surface elevation data, the NO<sub>2</sub> column, dependent on season, increase by 5-15%.

### 3.7 Summary

This chapter described the operational DOMINO processing system that retrieves tropospheric NO<sub>2</sub> columns from OMI. The DOMINO algorithm incorporates various improvements with respect to other NO<sub>2</sub> retrieval algorithms, which includes a data assimilation approach (using the TM4 CTM) to estimate stratospheric columns, daily updated temperature and a priori profiles in the calculation of the tropospheric air mass factor. In addition to the tropospheric and stratospheric NO<sub>2</sub> columns, the DOMINO product provides for each OMI pixel the averaging kernel together with temperature and a priori NO<sub>2</sub> profiles. The DOMINO product is distributed in an

offline stream that is available 2 days after measurement, and in a time-critical near-real time stream that is available within 3-4 hours after measurement. The NRT retrieval system uses the forecast stratospheric slant column,  $\text{NO}_2$  and temperature profile to achieve swift processing of OMI slant columns. The DOMINO product is widely used (see *Dirksen et al.* [2008] for an extensive list of DOMINO users), where the NRT product is relevant input for air quality forecast systems. Owing to a major reprocessing operation the DOMINO tropospheric  $\text{NO}_2$  observations for the entire OMI mission (October 2004-present) are now available as collection 3, version 1.0.2, which constitutes the optimal OMI tropospheric  $\text{NO}_2$  dataset to date.

The results of the DANDELIONS and INTEx-B validation campaigns show good agreement between  $\text{NO}_2$  columns from DOMINO and independent column observations. However, lidar observations and comparison with other models indicate that the DOMINO a priori profiles have too high  $\text{NO}_2$  at the surface, due to insufficient mixing by TM4 of  $\text{NO}_2$  in the boundary layer. This results in a lower tropospheric air mass factor and a subsequent overestimation of DOMINO tropospheric  $\text{NO}_2$ . Replacing the TM4 profiles by observed profiles combined with replacing the TOMS-GOME surface albedo by the OMI-derived surface albedo from *Kleipool et al.* [2008] results in an average change of 23% in the retrieved column while improving the agreement with the validation measurements. Based on the findings of validation and modeling studies the following future improvements to the DOMINO retrieval algorithm are proposed:

1. Improving the vertical mixing by TM4 of  $\text{NO}_2$  in the boundary layer by sampling the tracer  $\text{NO}_2$  field after the advection and convection steps have been performed, will produce more representative a priori profiles.
2. Replace the TOMS-GOME surface reflectivity with the OMI-based surface albedo from *Kleipool et al.* [2008]. Apart from improving the DOMINO tropospheric  $\text{NO}_2$  columns, it ensures consistency with the OMI cloud retrieval that also uses the *Kleipool et al.* [2008] surface albedo.
3. Using the effective surface elevation of OMI ground pixels instead of the coarse resolution ( $3^\circ \times 2^\circ$ ) TM4 based surface elevation will reduce the representativity error in the surface pressure that affects the a priori profile in mountainous regions.
4. Increasing the model resolution will improve the representativity of a priori profiles in regions with a spatially inhomogeneous tropospheric  $\text{NO}_2$  field due to the presence of, e.g., urban, pollution sources.





## Evaluation of stratospheric NO<sub>2</sub> retrieved from the Ozone Monitoring Instrument: intercomparison, diurnal cycle and trending

### Abstract

A 5+ year record of satellite measurements of nitrogen dioxide columns from the Ozone Monitoring Instrument (OMI) is evaluated to establish the quality of OMI stratospheric NO<sub>2</sub> and to test our understanding of NO<sub>2</sub> in the stratosphere. The use of assimilation techniques to retrieve the stratospheric vertical column of NO<sub>2</sub> from OMI slant column observations is described in detail. In the employed assimilation scheme the forecast model state is generally within  $0.15 \times 10^{15}$  molecules/cm<sup>2</sup> of the analysis over remote areas where stratospheric NO<sub>2</sub> dominates the total column. The Dutch OMI NO<sub>2</sub> (DOMINO) and Standard Product (SP) stratospheric NO<sub>2</sub> columns from OMI are consistent within  $0.3 \times 10^{15}$  molecules/cm<sup>2</sup>, or 13%, with independent, ground-based measurements of stratospheric NO<sub>2</sub>. This is comparable to the inconsistencies (15-20%) that exist between different ground-based techniques. On average, stratospheric NO<sub>2</sub> from DOMINO is higher than from SP by  $0.2 \times 10^{15}$  molecules/cm<sup>2</sup>, but larger differences occur on the synoptic scale. DOMINO captures the detailed structure and dynamics of the stratospheric NO<sub>2</sub> field during the collapse of the Arctic polar vortex in March 2005. Using the overlapping OMI orbits poleward of 30° latitude, it is possible to extract information on the diurnal variation in stratospheric NO<sub>2</sub> columns. At high latitudes (> 60°), the daytime increase of NO<sub>2</sub> has a distinct seasonal dependence with a maximum in spring and fall. Daytime increase rates inside the denoxified Arctic polar vortex are low, whereas high rates (>  $0.4 \times 10^{15}$  molecules/cm<sup>2</sup>/h) are found in the NO<sub>y</sub>-rich air outside the vortex. A multilinear regression to the 5-year DOMINO record shows a distinct quasi-biennial oscillation (QBO) signal in stratospheric NO<sub>2</sub> columns over the Tropics. The QBO's amplitude is comparable

---

The contents of this chapter, with some modifications, have been submitted as a paper to *Journal of Geophysical Research*.

to that of the annual cycle and is stronger over the Southern Hemisphere than over the Northern Hemisphere. DOMINO observations over Lauder are consistent with the ground-based stratospheric NO<sub>2</sub> measurements collected at this site, with near-identical trends for DOMINO (+0.4% per decade) and the ground-based (+0.6% per decade) for the time span of the OMI mission (2004-2010).

## 4.1 Introduction

Nitrogen dioxide (NO<sub>2</sub>) is an important trace gas in the atmosphere because of its role in the photochemistry of ozone in the stratosphere and in the troposphere. NO+NO<sub>2</sub> (NO<sub>x</sub>) in the stratosphere originates from the oxidation of N<sub>2</sub>O in the middle stratosphere. NO+NO<sub>2</sub> destroy ozone catalytically, but they can also suppress ozone depletion by converting reactive chlorine and hydrogen compounds into unreactive gas phase reservoirs such as ClONO<sub>2</sub> and HNO<sub>3</sub>. Monitoring of stratospheric NO<sub>2</sub> thus provides important support to monitoring of the ozone layer. Furthermore, outstanding questions exist about long-term changes in stratospheric NO<sub>2</sub> reported for instance from New Zealand [Liley *et al.*, 2000] and northern Russia [Gruzdev, 2008]. In the troposphere, NO<sub>x</sub> oxidizes rapidly, leading to the formation of ozone and aerosols. These secondary pollutants have highly uncertain effects on climate [IPCC, 2007], influence the oxidizing capacity of the troposphere, and affect human health. Global mapping of tropospheric NO<sub>2</sub> concentrations provides important constraints on the temporal behavior of NO<sub>x</sub> emissions.

Satellite remote sensing is used for measuring stratospheric as well as tropospheric NO<sub>2</sub> amounts. Stratospheric NO<sub>2</sub> has been measured by a number of satellites since the 1980s, e.g., SME (Solar Mesosphere Explorer) [Mount *et al.*, 1984], which first used the DOAS approach, SAGE-II/III (Stratospheric Gas and Aerosol Experiment [Chu and McCormick, 1986]), HALOE (Halogen Occultation Experiment [Gordley *et al.*, 1996]), and POAM (Polar Ozone and Aerosol Measurement [Randall *et al.*, 1998]). More recently, retrievals from the nadir-viewing UV-Vis spectrometers GOME (Global Ozone Monitoring Experiment) [Burrows *et al.*, 1999] and its successor GOME-2 [Munro *et al.*, 2006], SCIAMACHY (Scanning Imaging Absorption Spectrometer for Atmospheric Cartography) [Bovensmann *et al.*, 1999], and OMI (Ozone Monitoring Instrument) [Levelt *et al.*, 2006a] have provided information on both stratospheric and tropospheric NO<sub>2</sub>. Over unpolluted regions typically more than 90% of the observed NO<sub>2</sub> resides in the stratosphere, but over industrialized continental regions this fraction can range from 10-50%, depending on the degree of pollution. A challenge for the retrieval algorithms is the separation of the stratospheric and tropospheric contribution to the total NO<sub>2</sub> absorption inferred from the spectral measurements. Inaccuracies in this separation not only affect the stratospheric measurements themselves, but also the tropospheric retrievals that rely on residual techniques. Current methods to estimate stratospheric NO<sub>2</sub>

use chemistry-transport models [Boersma *et al.*, 2004, Richter *et al.*, 2005], filtering techniques based on subsets of satellite measurements [Bucsela *et al.*, 2006], or independent measurements of stratospheric NO<sub>2</sub> [Beirle *et al.*, 2010]. These techniques need to be thoroughly tested against independent observations, which is one of the goals of this study.

In this chapter we focus on OMI stratospheric NO<sub>2</sub>. The OMI retrievals start with total NO<sub>2</sub> slant column densities (SCDs), inferred from the instrument's spectrally resolved measurements in the visible spectral range. The total slant columns represent the integrated concentration of NO<sub>2</sub> along the effective light path through the atmosphere. Since photons in the visible traverse the lower atmosphere, there can be a significant contribution from tropospheric NO<sub>2</sub> to the total slant column. In the Dutch OMI NO<sub>2</sub> retrieval (DOMINO, Boersma *et al.* [2007]), the stratospheric component of the NO<sub>2</sub> slant column is estimated by data-assimilation of OMI slant columns in the TM4 chemistry-transport model. In the NASA/KNMI retrieval (Standard Product, Bucsela *et al.* [2006]), the stratospheric component is estimated by fitting a second order Fourier function in the zonal direction to a 24-hour composite of OMI observations. Both methods use air mass factors (AMFs) to convert stratospheric slant columns into vertical columns, but the AMFs are calculated with different radiative transfer models, and use different a priori information on the vertical distribution of stratospheric NO<sub>2</sub>.

In order to test and improve the stratospheric NO<sub>2</sub> information derived from OMI, the work presented in this chapter evaluates the two different OMI retrievals. We compare OMI stratospheric NO<sub>2</sub> from both retrievals with independent measurements taken at 14 remote NDACC (Network for the Detection of Atmospheric Composition Change) stations around the world. We used UV-Vis measurements from the SAOZ (Système d'Analyse par Observations Zénithal) network, a collection of near-identical collectively operated instruments that is part of NDACC, UV-Vis measurements from other NDACC stations as well as FTIR observations.

We subsequently evaluate the ability of the retrieval algorithms to separate out spatial and temporal variability in stratospheric NO<sub>2</sub>. We will show that the Dutch OMI NO<sub>2</sub> retrieval captures spatial and temporal variations in stratospheric NO<sub>2</sub> induced by planetary waves, and also the daytime buildup of stratospheric NO<sub>2</sub> resulting from the photolysis of N<sub>2</sub>O<sub>5</sub>. Furthermore, we will analyze the 5-year record of OMI stratospheric NO<sub>2</sub> columns and discuss signatures of the quasi-biennial oscillation apparent over tropical and mid-latitudes.

## 4.2 OMI stratospheric NO<sub>2</sub> data

### 4.2.1 OMI

The Dutch-Finnish Ozone Monitoring Instrument (OMI) is a UV-Vis imaging spectrometer that records the backscattered radiance from the Earth's atmosphere in three spectral channels between 264-504 nm at an average spectral resolution of 0.5 nm. It combines a wide longitudinal swath (2600 km) with high spatial resolution (24x13 km<sup>2</sup> at nadir). OMI is part of the NASA EOS-Aura mission (launched July 2004) which is in a Sun-synchronous ascending node orbit that crosses the equator at 13h40 local time. In the following two subsections we describe the algorithms of the DOMINO and the Standard Product. The DOMINO product is available at <http://www.temis.nl/airpollution/no2.html>, the Standard Product is available at <http://daac.gsfc.nasa.gov/Aura/data-holdings/OMI/index.shtml>. Both products use OMI NO<sub>2</sub> slant columns as input, and these are also included in the final product. A detailed description of OMI's scientific objectives is given in *Levelt et al.* [2006b], instrument details are available in *Dobber et al.* [2006].

### 4.2.2 Dutch OMI NO<sub>2</sub> (DOMINO) retrieval

The retrieval of the stratospheric and tropospheric NO<sub>2</sub> columns by the DOMINO algorithm is the result of a multi-step process. In the first step, slant columns of NO<sub>2</sub> are retrieved with the DOAS (Differential Optical Absorption Spectroscopy [*Platt and Stutz*, 2008]) method, by minimizing the differences between modeled and observed Earth reflectance spectra. The minimization is performed in the 405-465 nm spectral window, taking into account absorption by NO<sub>2</sub> and ozone, the Ring effect and a 3rd order polynomial that describes the background of the reflectance spectrum. The NO<sub>2</sub> cross section spectrum for 220 K is taken from *Vandaele et al.* [1998]. The retrieval method accounts for the temperature sensitivity of the NO<sub>2</sub> spectrum by applying a correction for the difference between the effective temperature of NO<sub>2</sub> along the light path derived from ECMWF meteorological analyses and modeled profiles, and the 220 K of the NO<sub>2</sub> absorption cross section spectrum [*Boersma et al.*, 2004]. Earth reflectance spectra follow from dividing the Earth radiance measurements by the OMI-measured solar irradiance. For signal-to-noise considerations a fixed solar irradiance spectrum has been constructed from daily irradiance measurements taken in 2005. Calibration errors resulting from, amongst others, the limited signal-to-noise of the solar irradiance measurements cause systematic enhancements of NO<sub>2</sub> slant columns at specific viewing angles, that show up as stripes along the orbit [*Boersma et al.*, 2007]. An improved calibration approach, with a better correction of the CCD detector's dark current, significantly reduced these stripes [*Dobber et al.*, 2008]. The data used in this study have been

processed with this improved dark current calibration. The precision of the retrieved NO<sub>2</sub> slant columns has been estimated to be  $0.7 \times 10^{15}$  molecules/cm<sup>2</sup> [Boersma *et al.*, 2007], which corresponds to approximately 10% of the unpolluted, and <5% of the polluted, slant column.

In the second step, OMI NO<sub>2</sub> columns are assimilated in the TM4 chemistry transport model [Dentener *et al.*, 2003]. The assimilation procedure is described in Section 4.2.2.1. In the third and final step the assimilated stratospheric slant column is subtracted from the total slant column and the remaining tropospheric slant column is converted into a vertical column by dividing by the tropospheric air mass factor (AMF). The AMF is defined as the ratio of slant-column density of the absorber along the (slant) optical path to the vertical column density. The AMF is calculated using the DAK [de Haan *et al.*, 1987, Stammes, 2001] radiative transfer model that takes into account viewing geometry, the absorber's vertical profile shape, terrain height, surface albedo, clouds, and Rayleigh scattering (including multiple scattering effects). The AMF depends on the tropospheric NO<sub>2</sub> profile, which is taken from space-time collocated TM4 model results. The spectral fitting and the tropospheric AMF have been studied in detail elsewhere [Boersma *et al.*, 2002, 2004, 2007] and we will now focus on the assimilation procedure to estimate stratospheric NO<sub>2</sub>.

#### 4.2.2.1 Estimation of the stratospheric NO<sub>2</sub> column

**4.2.2.1.1 TM4** We use the TM4 chemistry transport model (CTM) for the assimilation of OMI NO<sub>2</sub> columns. The assimilation system operates at a resolution of 3° x 2° (longitude x latitude), with 35 sigma-pressure levels up to 0.38 hPa in the vertical direction<sup>1</sup>. TM4 uses forecasted and analyzed 6-hourly meteorological fields, (3-hourly for boundary layer fields) from the European Centre for Medium Range Weather Forecast (ECMWF) operational model. These fields include global distributions of wind, temperature, surface pressure, humidity, cloud cover and (liquid and ice) water content, and precipitation. Mass conserving preprocessing of the meteorological input is performed as described by Bregman *et al.* [2003]. The physical processes included in determining tracer evolution are mass conserved advection, convective transport, boundary layer diffusion, photolysis and dry and wet deposition. NO<sub>x</sub> emissions are based on the EU POET (Precursors of Ozone and their Effects on the Troposphere) database for 1997 [Olivier *et al.*, 2003], yielding a global total of 46 Tg N/yr. Chemical processes in the troposphere are governed by the Carbon Bond Mechanism 4 (CBM-4) chemistry scheme that includes non-methane hydrocarbons to account for loss by reaction with OH [Houweling *et al.*, 1998].

<sup>1</sup> After 1 February 2006 the model configuration was changed to 34 pressure levels, driven by a change in the sigma levels of the meteorological input.

The CBM-4 scheme accounts for O<sub>x</sub>-NO<sub>x</sub>-HO<sub>x</sub> chemical reactions in the stratosphere, including the conversion of NO and NO<sub>2</sub> to N<sub>2</sub>O<sub>5</sub> and HNO<sub>3</sub>. Other chemical aspects, such as the photolysis of N<sub>2</sub>O and reactions with halogens such as bromine and chlorine are missing. Some effects of the simplified chemistry in the stratosphere are compensated for by constraining the modeled concentrations to observed climatological values in the middle/upper stratosphere. Above 50 hPa in the tropics and above 100 hPa in the extra-tropics, ozone concentrations are nudged to mean observed values taken from the Fortuin-Kelder climatology [Fortuin and Kelder, 1998] (scaled with the TOMS total O<sub>3</sub> column for 1997) with a relaxation time of 2-5 days, depending on latitude. At 10 hPa, stratospheric HNO<sub>3</sub> is nudged to the UARS-derived O<sub>3</sub>/HNO<sub>3</sub> ratios for 1992, with a characteristic relaxation time of two months. This is a modification of the original TM4 code, where the UARS O<sub>3</sub>/HNO<sub>3</sub> ratio is simply prescribed. The long relaxation time for this nudging prevents the model from strongly interfering with the NO<sub>x</sub> analysis resulting from the data assimilation discussed below. Above 10 hPa, the NO<sub>x</sub> volume mixing ratio is nudged to its modeled value at 10 hPa, again with characteristic relaxation time of two months. The prescribed 10 hPa HNO<sub>3</sub> mixing ratio constitutes the effective source of stratospheric NO<sub>x</sub> in TM4.

**4.2.2.1.2 Data assimilation** The purpose of the assimilation is to regularly update the TM4 simulation of the three-dimensional NO<sub>2</sub> distribution with available measurement data in such a way that the model simulation of the stratospheric NO<sub>2</sub> column is in close agreement with the OMI measurements. The assimilation also provides a realistic error estimate for the stratospheric NO<sub>2</sub> column (see below). The assimilation scheme is based on the Kalman filter technique, with a prescribed parameterization of the horizontal correlations between forecast errors to reduce computational effort. A schematic layout of the assimilation procedure is presented in Figure 4.1. The upper loop in Figure 4.1 illustrates the TM4 simulation of the three-dimensional NO<sub>2</sub> field with a time step  $\Delta t$  (30 minutes in TM4). If NO<sub>2</sub> slant columns are available with a measurement time within 15 minutes of the model time, the model field is updated by the Kalman filter. In the Kalman filter update, the forecast model state is adjusted towards the observations, replacing the forecast with the analysis. This analyzed profile  $\bar{x}_a$  includes NO<sub>2</sub> in both troposphere and stratosphere, and is calculated from the forecast  $\bar{x}_f$  and the superobservation  $\bar{y}$  (explained below) by

$$\bar{x}_a = \bar{x}_f + \mathbf{PH}^T (\mathbf{HPH}^T + \mathbf{R})^{-1} (\bar{y} - \bar{y}_m) \quad (4.1)$$

With matrix  $\mathbf{H}$  the observation operator,  $\mathbf{P}$  the forecast error covariance matrix, and  $\mathbf{R}$  the combined observation and representativeness error covariance [Eskes *et al.*, 2003]. The role of  $\mathbf{H}$ ,  $\mathbf{P}$  and  $\mathbf{R}$  will be discussed in more detail below. The term  $\mathbf{PH}^T (\mathbf{HPH}^T + \mathbf{R})^{-1}$  determines the most likely adjustment of the model state, given the observed difference between observed and forecast model column ( $\bar{y} -$

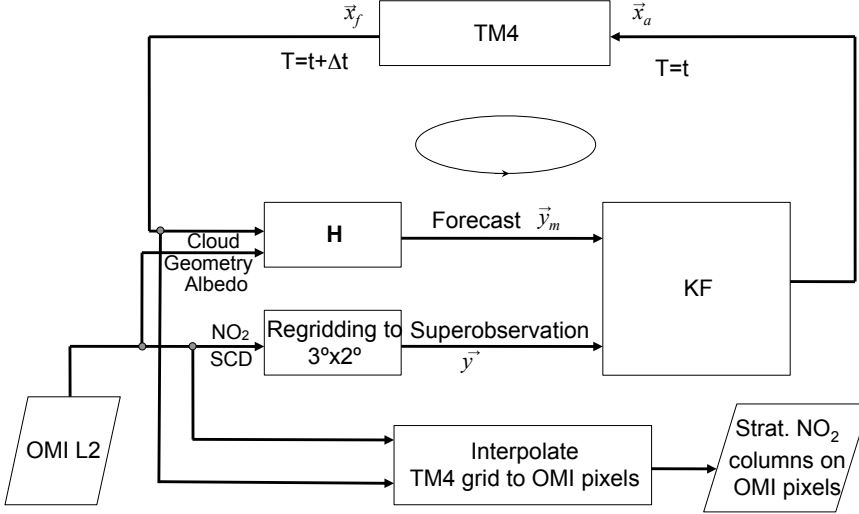


**Figure 4.1** Schematic diagram of the OMI stratospheric NO<sub>2</sub> assimilation. TM4 simulates the forecast NO<sub>2</sub> field ( $\vec{x}_f$ ) for the model time  $t + \Delta t$  (upper branch of the scheme). OMI observations coincident with this time step are averaged over the  $3^\circ \times 2^\circ$  TM4 grid cells to yield superobservations  $\vec{y}$ . The observation operator **H** uses OMI pixel coordinates, viewing geometry, cloud and albedo information from the OMI L2 data to convert the forecast NO<sub>2</sub> profiles  $\vec{x}_f$  into forecast NO<sub>2</sub> total slant columns ( $\vec{y}_m$ ). The Kalman filter (KF) then forces the forecast to the superobservation to produce analyzed NO<sub>2</sub> profiles ( $\vec{x}_a$ ) that are input to the subsequent model time step. The stratospheric NO<sub>2</sub> columns for the OMI measurements result from interpolating the forecast  $3^\circ \times 2^\circ$  NO<sub>2</sub> field to the OMI pixel locations and summing the layers above the tropopause. This is represented by the lower branch.

$\vec{y}_m$ , observation minus forecast, O–F). Note that the total slant column  $\vec{y}$  includes the NO<sub>2</sub> present in both troposphere and stratosphere. The relative size of the adjustment depends on the ratio between the uncertainties in the model forecast and observations, and the model analysis will closely follow the observations when this ratio is large.

#### Observation operator **H** and superobservations $\vec{y}$

The observation operator **H** is proportional to the averaging kernel [Eskes and Boersma, 2003], a 35-element vector that contains the sensitivity of OMI to NO<sub>2</sub> in each model-layer. The scalar product of the observation operator vector and the TM4 NO<sub>2</sub> profile at the location of the individual OMI observations yields the slant column that would be observed by OMI given the modeled profile  $\vec{x}_f$ . The average of all OMI observations (and model-equivalents) with center coordinates inside a  $3^\circ \times 2^\circ$  TM4 grid cell is treated as a single measurement,



dubbed superobservation (and model-equivalent).  $\bar{y}_m$  is the model forecast of the superobservations, given by  $\mathbf{H}\bar{x}_f$ . In order to reduce the computational effort, the Kalman filter is applied for these superobservations.

### Observation error covariance matrix $\mathbf{R}$

The diagonal elements of  $\mathbf{R}$  equal the square of the observation error  $\mathbf{R}_{ii} = \sigma_o^2$ , where  $\sigma_o$  is chosen to depend explicitly on the modeled profile shape,

$$\sigma_o = (AS_{\text{trop}} + BS_{\text{strat}})/S \quad (4.2)$$

with  $S_{\text{trop}}$  the tropospheric contribution to the total slant column  $S$ , and  $S_{\text{strat}}$  the stratospheric contribution to the slant column taken from the TM4 forecast. The unknown true  $S_{\text{trop}}$  and  $S_{\text{strat}}$  are approximated by the model estimates. The values assigned to the coefficients  $A$  and  $B$  are 4.0 and 0.25 ( $\times 10^{15}$  molecules/cm<sup>2</sup>) respectively. The small value of the stratospheric observation error  $B$  reflects the relatively accurate measurement of stratospheric NO<sub>2</sub>; radiative transfer calculations have small errors for NO<sub>2</sub> in the middle and higher atmosphere. Because of averaging of OMI observations into superobservations, much of the noise in the OMI observations cancels out, consistent with our small value for  $B$ . The value of  $B$  is furthermore consistent with the standard deviation of the observed O–F value. The large value of  $A$  reflects the large retrieval uncertainty for tropospheric NO<sub>2</sub>, which is very sensitive to assumptions on cloud modeling, surface reflectivity, profile shape or aerosol concentration [Boersma *et al.*, 2004]. In the stratosphere total reactive nitrogen (NO<sub>y</sub>) is a well-conserved quantity, with relatively small source and sink contributions. This implies that the information from the observations can be stored in the model over long time periods. Furthermore, experiences with ozone assimilation have shown that modern weather prediction models are well capable of describing the dynamical variability of stratospheric tracer concentrations. A successful stratospheric assimilation can therefore be expected. In contrast, the tropospheric NO<sub>2</sub> budget is characterized by strong sources and sinks, resulting in short NO<sub>2</sub> lifetimes of 5-20 hours in the lower troposphere. Updates brought to the simulated tropospheric NO<sub>2</sub> concentration field are therefore rapidly lost, typically within one day.

The observation error covariance matrix  $\mathbf{R}$  defined in this way effectively filters out OMI observations with increased tropospheric NO<sub>2</sub> columns by attributing less weight to OMI observations over (known) polluted areas. This filtering leads to a strong forcing of the simulated stratospheric NO<sub>2</sub> concentrations towards the OMI observations, and will result in only a marginal adjustment of the simulated tropospheric NO<sub>2</sub> field.

### Covariance matrix $\mathbf{P}$

The covariance matrix  $\mathbf{P}$  accounts for the forecast error due to model imperfections. The diagonal or variance is set to a fixed value  $\mathbf{P}_{ii} = \sigma_f^2$ , where  $\sigma_f = 0.15 \times 10^{15}$  molecules/cm<sup>2</sup>. This value is consistent with the variance of O–F

values apparent over remote areas. A second-order autoregressive (Thiebaux) function with a characteristic length of 600 km (hereafter called correlation length) describes the correlation between the errors of neighboring grid cells. This correlation length transforms a local O–F difference into a spatially extended, smeared forcing in model space. Consequently, the correlation length filters out structures smaller than 600 km in the O–F, reducing the local impact of small-scale structures (partly from tropospheric origin) on the assimilated stratospheric NO<sub>2</sub> field. This implies that small-scale variations in the OMI observations, such as the stripes [Boersma *et al.*, 2007], are dampened and have only minor implications for the (stratospheric) analysis.

Strong gradients in stratospheric NO<sub>2</sub> are occasionally found, in particular related to the Noxon cliff [Noxon, 1979]. Such sharp drops in NO<sub>x</sub> concentrations indicate that air masses on either side of the cliff have a very different chemical history. Error correlations are assumed to be small in such cases. To account for this we introduce a NO<sub>2</sub> concentration gradient dependence in the correlation,

$$C_{ij} = \begin{cases} e^{-\left(\frac{\Delta\rho_{ij}}{0.5\sigma}\right)^2} & \Delta\rho_{ij} < 0.9 \\ 0 & \Delta\rho_{ij} > 0.9 \end{cases} \quad \text{with } \Delta\rho_{ij} = \left| \frac{c_i - c_j}{c_i + c_j} \right| \quad (4.3)$$

with  $c_i$  and  $c_j$  the concentrations in grid-cells  $i$  and  $j$ ,  $\sigma$  the characteristic concentration length, which is set to 30%. Such a term is effective in preventing the occurrence of negative analyzed NO<sub>2</sub> values within the vortex. The off-diagonal elements  $\mathbf{P}_{ij}$  are the product of  $C_{ij}$  and the correlation length.

All the model NO<sub>y</sub> species (NO, NO<sub>2</sub>, NO<sub>3</sub>, N<sub>2</sub>O<sub>5</sub>, HNO<sub>4</sub>) are assumed to be fully correlated. Hence the forcing of the modeled NO<sub>2</sub> field is also directly applied to the other four nitrogen oxides. The (3°x2°) forecast NO<sub>2</sub> field is spatially interpolated to the location of the OMI pixel center, and the stratospheric column is calculated by summing all layers above the tropopause. The TM4 tropopause level follows from applying the WMO 1985 definition (lowest level where the lapse rate is smaller than 2°C/km) to the ECMWF temperature profiles. The forecast stratospheric NO<sub>2</sub> columns are used in the retrieval of the tropospheric column, and they are stored in the DOMINO data file<sup>2</sup>. This is represented by the lower branch in the scheme shown in Figure 4.1. The forecast columns in regions with negligible overlap between consecutive OMI orbits, have evolved freely for approximately 24 model hours since previous OMI overpass and model forcing. Using forecast columns instead of the analyzed columns has the advantage of reducing attribution errors for localized tropospheric contributions to the NO<sub>2</sub> slant column that are not simulated by the model, for instance from boreal fires. Such events may be partly attributed to the

<sup>2</sup> The forecast stratospheric NO<sub>2</sub> column is stored in the data field *AssimilatedStratosphericVerticalColumn*.

stratosphere in the analysis, which would lead to a local underestimation of the tropospheric column.

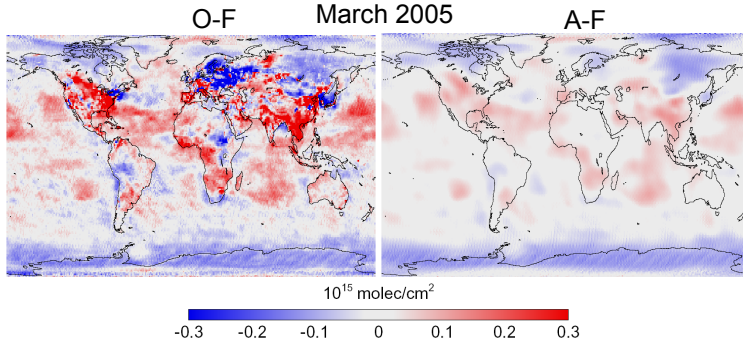


**Figure 4.2** Monthly mean observation–forecast (O–F, left panel) and analysis–forecast (A–F, right panel) differences in NO<sub>2</sub> slant columns for March 2005 ( $1^\circ \times 1^\circ$ ). For each OMI pixel, the measured slant column (observation) and the model-predicted slant column (forecast) were divided by the same geometrical air mass factor.

**4.2.2.2 Assimilation results** Figure 4.2 shows the global distribution of monthly mean observation minus forecast (O–F) and the model forcing (analysis minus forecast, A–F) for March 2005. The difference between the left and right panel in Figure 4.2 illustrates the effect of the assimilation: considerable O–F differences, resulting mostly from (anthropogenic) tropospheric NO<sub>2</sub> sources, have only a minor influence on the analysis. On the other hand, synoptic-scale structures in O–F persist in the A–F differences. That the A–F differences are much smaller (generally less than  $\pm 0.15 \times 10^{15}$  molecules/cm<sup>2</sup>) than the O–F differences (up to  $\pm 0.4 \times 10^{15}$  molecules/cm<sup>2</sup>) demonstrates that most tropospheric contributions are effectively masked by the assimilation procedure in combination with Equation 4.2. The persistent synoptic-scale structures in the A–F differences indicate a slight tendency in TM4 to deviate from the observed fields. The absence of land-sea transitions in the A–F differences illustrates that the strength of the forcing is comparable over land and over sea. This reflects that the stratospheric NO<sub>2</sub> field is largely decoupled from the troposphere in the analysis, and as such is not bound to the geographical distribution of land-sea masses.

We evaluate the impact of the assimilation by comparing a 12-month TM4 free run to the assimilation run. Both runs were initialized with the same model start field for 1 January 2005. In the tropics (30°S–30°N) the difference assimilation minus free model run increases by approximately  $+0.5 \times 10^{15}$  molecules/cm<sup>2</sup> per month and stabilizes at  $+1.3 \times 10^{15}$  molecules/cm<sup>2</sup>, which implies that TM4 in the free-running

mode underestimates the stratospheric NO<sub>2</sub> column in the tropics by 50%. For mid-latitudes the difference between TM4 and assimilation varies with season, with an amplitude comparable to the value in the tropics. The main source of stratospheric NO<sub>2</sub>, nitrous oxide (N<sub>2</sub>O), is not modeled by TM4, which may explain part of the biases in TM4 NO<sub>2</sub>. Stratospheric NO<sub>2</sub> is effectively driven by the UARS ratio of HNO<sub>3</sub>:O<sub>3</sub> in combination with the Fortuin & Kelder O<sub>3</sub> climatology. Since the nudging is relatively slow—the relaxation time is two months, comparable with the timescale of poleward transport—stratospheric NO<sub>2</sub> concentrations in TM4 follow the climatologies with significant delay. Imposing the HNO<sub>3</sub>:O<sub>3</sub> ratio, such as applied in the original TM4 model, is likely to reduce the bias.

Up to now, no validation studies of TM4 stratospheric tracers have been reported, but TM4 stratospheric ozone columns are consistent with the 30 year data record of total column ozone observations by TOMS, SBUV, GOME, SCIAMACHY, OMI and GOME-2 that is presented in *van der A et al.* [2010]. The significant differences between TM4 and assimilated stratospheric NO<sub>2</sub> that we find here, illustrate that the absolute values of the DOMINO stratospheric NO<sub>2</sub> columns are strongly driven by the OMI NO<sub>2</sub> observations and that the model input is limited to providing a forecast from observation-based analyzed fields.

#### 4.2.3 NASA GSFC (Standard product) retrieval

The Standard Product (SP) is an operational algorithm for the retrieval of tropospheric NO<sub>2</sub> vertical column densities for OMI. Analogously to the DOMINO product, the SP algorithm starts with DOAS fitted slant column densities of the OMI L2 data. The basic algorithm for the retrieval of total column and tropospheric NO<sub>2</sub> is described by *Boersma et al.* [2002] and *Bucsela et al.* [2006]. The Standard Product identifies the stratospheric NO<sub>2</sub> columns as the slowly varying part of the total column NO<sub>2</sub> field, which implies that medium-scale variations up to several 100 km in the total column NO<sub>2</sub> field are attributed to tropospheric signals.

In the first step, NO<sub>2</sub> slant columns are converted into initial vertical columns (VCD<sub>init,SP</sub>) by dividing by an (unpolluted) air mass factor (AMF<sub>init,SP</sub>). These air mass factors are derived from radiative transfer calculations with the TOMRAD radiative transfer model [*Dave*, 1965] with annually averaged simulated NO<sub>2</sub> profile shapes. These profiles are constructed by merging the GSFC CTM [*Douglass et al.*, 2003] 3-D profiles for the stratosphere with 3-D tropospheric profiles from the GEOS-Chem model [*Martin et al.*, 2002b].

In essence the Standard Product builds on the reference sector method [*Martin et al.*, 2002a] and on the method reported by *Wenig et al.* [2003], who assumed GOME observations over unpolluted regions (oceans) to represent the stratospheric NO<sub>2</sub> field for these latitudes, and interpolated to fill the gaps over the continents. The Standard Product applies a second order Fourier (wave-2) fit in 1°-wide latitude

bands in the zonal direction to all data collected within  $\pm 12$  hours of the target orbit [Bucsela *et al.*, 2008]. Prior to the wave-2 fit, regions with known high tropospheric NO<sub>2</sub> abundances (identified using GEOS-Chem) are masked and a  $9^\circ$  wide boxcar running average is applied in the meridional direction. Areas with strong deviations from the wave-2 fit are identified as contaminated by tropospheric NO<sub>2</sub> pollution and also masked. Then, the wave-2 fit is performed for the second time. The local stratospheric NO<sub>2</sub> column is thus based on a spatial fit to a 24-hour ensemble of OMI observations, and is subtracted from the OMI observations to produce the tropospheric slant column field. The stratospheric NO<sub>2</sub> columns used in this study are calculated by evaluating the wave-2 polynomial, using the coefficients that are stored in the SP data file. A detailed discussion of the Standard Product algorithm can be found elsewhere [Bucsela *et al.*, 2006, Celarier *et al.*, 2008].

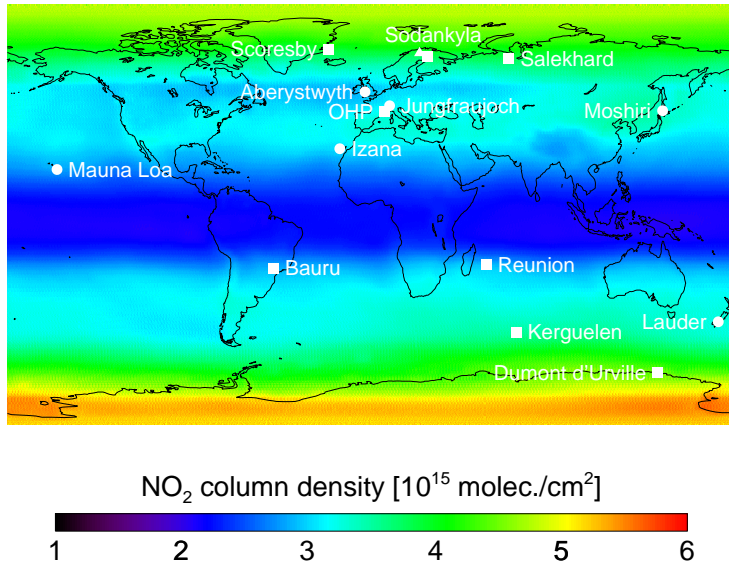


**Figure 4.3** Geographical distribution of 14 ground-based measurement sites for remote sensing observations of stratospheric NO<sub>2</sub> used in this study. Squares indicate CNRS-operated SAOZ stations, circles indicate NDACC-operated stations, the triangle indicates the FTIR station in Kiruna. The collocated FTIR stations in Izaña and Jungfraujoch are not indicated separately. The colored map represents the annual mean of DOMINO stratospheric NO<sub>2</sub> for 2005.

### 4.3 Data sets

OMI stratospheric NO<sub>2</sub> columns are compared to ground-based UV-Vis and FTIR measurements taken at various NDACC (Network for the Detection of Atmospheric Composition Change) stations. Part of the NDACC UV-Vis instruments belong to the SAOZ network. The nearly identical SAOZ instruments all are operated by CNRS. In this study we make a distinction between the SAOZ instruments and the other NDACC-certified UV-Vis instruments that are operated by individual institutes.

#### 4.3.1 SAOZ

The SAOZ (Système d'Analyse par Observations Zénithal) system constitutes a network of ground-based UV-Vis spectrometers to measure stratospheric ozone and NO<sub>2</sub>. SAOZ spectrometers [Pommereau and Goutail, 1988] record the zenith sky spectrum between 300-620 nm at 1 nm resolution. Currently, the SAOZ network consists of 10 instruments located at various latitudes between 70°S and 70°N, and their locations are shown in Figure 4.3. In general, the SAOZ instruments are situated at pristine or elevated locations, far away from significant sources of tropospheric NO<sub>2</sub>.

Measurements are performed around twilight (solar zenith angles between 86° and 91°). The long light path through the stratosphere, and the relatively short vertical light path through the troposphere make the measured slant column roughly 18 times more sensitive to stratospheric NO<sub>2</sub> than to NO<sub>2</sub> in the troposphere.

NO<sub>2</sub> slant columns are retrieved by a DOAS fit in the 410-530 nm wavelength range to the ratio of the twilight spectrum and a reference spectrum, typically taken at noon under cloud free conditions. Different SAOZ groups take different approaches for the reference spectrum. For instance, Vaughan *et al.* [2006] use a new reference spectrum for each month, whereas Ionov *et al.* [2008] employ a fixed reference spectrum for the entire measurement series at a measurement site. Slant columns are converted to vertical columns by the air mass factor (AMF) which is calculated with a radiative transfer model developed by CNRS [Sarkissian *et al.*, 1995]. The air mass factors are calculated at 470 nm taking into account solar zenith angle and NO<sub>2</sub> profile shape.

Intercomparisons of NDACC-certified UV-Vis instruments show that retrieved NO<sub>2</sub> slant columns agree within 5-10% for common spectral ranges and analysis parameters, [e.g., [Hofmann *et al.*, 1995, Vaughan *et al.*, 1997, Roscoe *et al.*, 1999, Vandaele *et al.*, 2005]]. However, the accuracy of the stratospheric NO<sub>2</sub> vertical column is limited by errors in the AMF calculation, errors in the residual NO<sub>2</sub> amount in the reference spectrum, and errors resulting from not accounting for the temperature dependence of the NO<sub>2</sub> absorption cross section. This yields an overall

accuracy of 21% of stratospheric NO<sub>2</sub> vertical columns retrieved with ground-based UV-Vis instruments [Ionov *et al.*, 2008].

In order to compare stratospheric NO<sub>2</sub> observations from SAOZ (sunrise, sunset) and OMI (approximately 13h40 local time), we need to account for the considerable time difference between the two measurement methods. A chemical box-model [Denis *et al.*, 2005, Ionov *et al.*, 2008], based on chemistry from the SLIMCAT 3-D CTM [Chipperfield *et al.*, 1996], is used to calculate representative overhead columns at 12h00 local time from the SAOZ twilight measurements. This model simulates the diurnal variation of stratospheric NO<sub>2</sub>, it includes 98 chemical and 39 photochemical reactions, including heterogeneous chemistry on liquid and solid aerosols. The error associated with this model-based adjustment is not included in the above quoted 21% accuracy. OMI stratospheric NO<sub>2</sub> data are also adjusted to local noon with the same model. The magnitude of the adjustment depends, apart from time of overpass, on season and latitude. For the SAOZ sunrise to noon correction the adjustment ranges from  $<0.1 \times 10^{15}$  molecules/cm<sup>2</sup> (5%) in the tropics to  $>2 \times 10^{15}$  molecules/cm<sup>2</sup> (30%) for the high latitude stations in summer. For DOMINO the adjustment to local noon is typically smaller (up to  $0.4 \times 10^{15}$  molecules/cm<sup>2</sup>, or 12%).

#### 4.3.2 NDACC UV-Vis zenith sky data

In addition to the SAOZ stations a considerable number of independently operated SAOZ-like instruments contribute to the NDACC network (<http://www.ndsc.ncep.noaa.gov/>). Similar to the SAOZ stations these instruments record the UV-Vis zenith sky spectrum at sunrise and sunset. NDACC and SAOZ instruments are comparable, but not identical and often of higher quality. The operational wavelength range or the employed fitting window for NO<sub>2</sub> retrieval is different for some of the NDACC instruments, as are other instrument characteristics such as spectral profile sampling and resolution. Furthermore different radiative transfer codes are used to determine the AMFs. The resulting error budget has been reported to be similar to the SAOZ instruments, with a 21% accuracy of the stratospheric vertical NO<sub>2</sub> column [Ionov *et al.*, 2008]. The twilight NO<sub>2</sub> columns retrieved by the NDACC instruments are adjusted to local noon columns by the same model that was used to adjust the SAOZ and OMI measurements.

#### 4.3.3 Ground-based FTIR stations

The NDACC network also contains several NO<sub>2</sub> observing Fourier Transform Infra-Red (FTIR) instruments. A major advantage of the FTIR systems is the use direct Sun measurements under clear sky conditions, which removes the need for complicated radiative transfer calculations to compute the air mass factor. Owing to

its wavelength range and high spectral resolution the FTIR method is sensitive to the pressure and temperature dependence of the NO<sub>2</sub> cross section spectrum. *Camy-Peyret et al.* [1983] and *Flaud et al.* [1983] presented error estimates of FTIR NO<sub>2</sub> column retrievals, showing accuracies of approximately 10%. However, the dominant error source in FTIR are inaccuracies in the a priori NO<sub>2</sub> profile assumed in the retrieval and these can result in errors of approximately 30% [*Rinsland et al.*, 2003] as we will discuss later. Other sources of error are the assumed temperature profile, signal to noise, and the accuracy of the absorption cross section.

#### 4.4 Evaluation of OMI stratospheric NO<sub>2</sub>

##### 4.4.1 Evaluation of ground-based techniques

First we investigate the consistency between the FTIR and UV-Vis measurements of stratospheric NO<sub>2</sub>. This is motivated by an earlier study by *Vaughan et al.* [1997] that reported discrepancies of up to 30% in the NO<sub>2</sub> column between different UV-Vis instruments. At the NDACC stations Jungfraujoch and Izaña, FTIR instruments are collocated with zenith sky observing instruments, which enables the evaluation of both techniques against each other. The Kiruna station is located 300 km west of Sodankyla, close enough to compare the Kiruna FTIR to the Sodankyla SAOZ instrument in absence of strong gradients in stratospheric NO<sub>2</sub>.

Figure 4.4 shows a comparison of stratospheric NO<sub>2</sub> columns inferred from ground-based FTIR and UV-Vis instruments with those retrieved from OMI for Sodankyla, Jungfraujoch and Izaña. The FTIR measurement closest in time to the OMI overpass was used, and the time difference ranges from 30 minutes to two hours. The time series in the upper row of Figure 4.4 show how the amplitude of the seasonal cycle increases with latitude, with the largest stratospheric NO<sub>2</sub> columns over Sodankyla (67.4°N) in summer. This reflects the larger number of sunlit hours at high latitudes, which causes the complete conversion of the N<sub>2</sub>O<sub>5</sub> reservoir specie to NO<sub>x</sub> in summer [*Solomon and Keys*, 1992]. The 12h00 adjusted SAOZ data are always at the lower end of the grey bars that indicate measurements of stratospheric NO<sub>2</sub> at sunrise and sunset. In the summer months, the SAOZ sunrise measurements over Sodankyla are well above the adjusted noon values, for the same reason (N<sub>2</sub>O<sub>5</sub> depletion).

The scatter plots in the bottom row of Figure 4.4 show that over Sodankyla the agreement between SAOZ and FTIR (and DOMINO) is very good ( $r=0.96$ , slope=+1.01, offset=+0.23x10<sup>15</sup> molecules/cm<sup>2</sup>). Over Jungfraujoch we find good agreement between UV-Vis and FTIR ( $r=0.91$ , slope=+1.28, offset=-0.66x10<sup>15</sup> molecules/cm<sup>2</sup>), but only after careful inspection of the effect of the a priori profile in the retrieved columns. The original a priori profile was replaced with a profile taken from the AFGL standard mid-latitude atmosphere [*Anderson et al.*, 1986] that has less NO<sub>2</sub> in the troposphere, reducing the retrieved NO<sub>2</sub> columns by 30% (Philippe



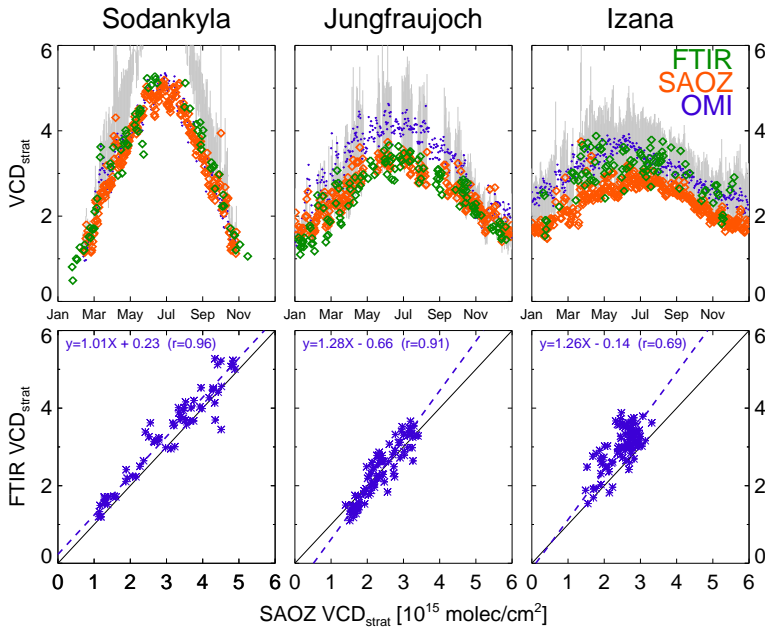


**Figure 4.4** Comparison between SAOZ, FTIR and DOMINO stratospheric NO<sub>2</sub> columns for Sodankyla/Kiruna (left column), Jungfraujoch (middle column) and Izaña (right column). OMI pixels within 10 km of the measurement station have been used. SAOZ and OMI data have been adjusted to local noon using a SLIMCAT-based chemical box-model. For days with multiple FTIR measurements, the data closest in time to OMI overpass is taken, with a typical time difference between OMI overpass and FTIR measurement of 30 minutes to two hours. The grey bands in the upper plots represent the range covered by the SAOZ sunrise and sunset measurements. The solid line in the scatter plots (bottom row) denotes unity, the dashed lines represent a reduced major axis fit [Clarke, 1980] to the data.

Demoulin, personal communication). Over Izaña the FTIR data are consistently higher than the zenith sky values with poorer correlation ( $r = 0.69$ , slope = +1.26, offset =  $-0.14 \times 10^{15}$  molecules/cm<sup>2</sup>). Recently, a thorough inspection of the UV-Vis instrument at Izaña revealed improper illumination of the detector and issues with the stray light correction resulting in a 15% underestimation of the UV-Vis stratospheric NO<sub>2</sub> columns (Manuel Gil, private communication). Correcting for these inaccuracies would bring UV-Vis more in line with FTIR and OMI. We conclude that the ground-based techniques are mutually consistent within 15-20%, which is consistent with accuracies reported in other studies. *De Mazière et al.* [1998] found a +5% offset between the ground-based FTIR and zenith sky measured vertical NO<sub>2</sub> columns at Jungfraujoch. *Kerzenmacher et al.* [2008] performed a comprehensive

validation study of ACE-FTS (a spaceborne FTIR recording solar occultation spectra) versus ground-based FTIR and UV-Vis (SAOZ) instruments and found a +15% offset between the spaceborne FTIR and SAOZ techniques.

**Table 4.1** Statistical summary of comparison DOMINO and SP versus ground-based observations.

Station (SAOZ)	abs.diff.		rel. diff. (%)		RMS		<i>r</i>	
	DOMINO	SP	DOMINO	SP	DOMINO	SP	DOMINO	SP
Dumont d'Urville	0.471	0.074	11.7	1.9	0.435	0.401	0.886	0.926
Kerguelen	0.338	0.024	10.6	0.8	0.399	0.369	0.886	0.894
Bauru	-0.109	-0.163	-3.4	-5.1	0.318	0.252	0.535	0.726
Reunion	-0.040	-0.084	-1.3	-2.8	0.349	0.334	0.660	0.732
OHP	-0.049	-0.381	-1.5	-11.6	0.454	0.467	0.824	0.767
Sodankyla	0.090	-0.101	2.6	-3.0	0.316	0.292	0.965	0.971
Scoresby	0.198	0.041	5.8	1.2	0.288	0.232	0.980	0.980
<b>Mean</b>	<b>0.128</b>	<b>-0.084</b>	<b>3.5</b>	<b>-2.7</b>	<b>0.366</b>	<b>0.335</b>	<b>0.819</b>	<b>0.857</b>
(other NDACC)								
Lauder	0.355	0.279	12.3	9.7	0.360	0.404	0.896	0.867
Mauna Loa	-0.154	-0.239	-5.5	-8.5	0.276	0.339	0.946	0.928
Izaña	0.681	0.617	29.1	26.4	0.291	0.198	0.794	0.897
Moshiri	0.137	-0.119	4.2	-3.7	0.511	0.428	0.706	0.803
Jungfrauoch	0.519	0.261	21.0	10.6	0.450	0.447	0.891	0.814
Aberystwyth	0.438	0.298	17.1	11.6	0.422	0.320	0.953	0.951
<b>Mean</b>	<b>0.329</b>	<b>0.183</b>	<b>13.0</b>	<b>7.7</b>	<b>0.385</b>	<b>0.356</b>	<b>0.864</b>	<b>0.877</b>
(FTIR)								
Izaña	0.205	0.127	6.8	4.3	0.414	0.354	0.627	0.730
Jungfrauoch	0.619	0.424	25.3	17.3	0.355	0.411	0.929	0.859
Kiruna	-0.120	-0.272	-3.6	-8.8	0.347	0.384	0.958	0.957
<b>Mean</b>	<b>0.235</b>	<b>0.093</b>	<b>9.5</b>	<b>4.3</b>	<b>0.372</b>	<b>0.383</b>	<b>0.838</b>	<b>0.849</b>

#### 4.4.2 Evaluation of OMI stratospheric NO<sub>2</sub> with ground-based measurements

DOMINO and ground-based observations of stratospheric NO<sub>2</sub> over Sodankyla agree very well, as shown in Figure 4.4. Figure 4.5 shows the seasonal variation in stratospheric NO<sub>2</sub> columns measured by DOMINO, the Standard Product (SP) and ground-based instruments from the NDACC network, with high NO<sub>2</sub> columns in summer and smaller columns in winter. DOMINO and SP both show reasonable agreement with the ground-based data. The bias between the latitude and seasonally averaged OMI products and ground-based data is generally within  $1 \times 10^{15}$  molecules/cm<sup>2</sup>, and as shown in Figure 4.6, the stations do not share a clear persistent bias pattern. Figure 4.6 shows the differences between OMI and ground-based measurements of stratospheric NO<sub>2</sub> at individual stations. The Figure does not reveal a consistent seasonal cycle in the bias among the stations. On average, the bias for both retrievals is always smaller than  $0.3 \times 10^{15}$  molecules/cm<sup>2</sup> with an RMS error of approximately  $0.4 \times 10^{15}$  molecules/cm<sup>2</sup>. The agreement between OMI and ground-based stratospheric NO<sub>2</sub> is on average within 13%. We consider this agreement optimal, given the estimated accuracy of the ground-based techniques of 21% and errors in OMI retrievals of approximately  $0.2 \times 10^{15}$  molecules/cm<sup>2</sup>. Over the SAOZ and NDACC stations, DOMINO exceeds ground-based stratospheric NO<sub>2</sub> by  $+0.23 \times 10^{15}$  molecules/cm<sup>2</sup> and SP by  $+0.06 \times 10^{15}$  molecules/cm<sup>2</sup> which implies that DOMINO is on average approximately  $0.2 \times 10^{15}$  molecules/cm<sup>2</sup> higher than SP over these stations.

#### 4.5 Detailed comparison of stratospheric NO<sub>2</sub> from DOMINO and SP

Figures 4.5 and 4.6 show that the DOMINO stratospheric columns exceed those from SP. This is confirmed by Table 4.1, which summarizes the annual mean bias between the OMI retrievals and the ground-based measurements. Figure 4.7 shows a comparison for DOMINO and SP stratospheric NO<sub>2</sub> retrievals for January and July 2005. The left panel confirms that stratospheric NO<sub>2</sub> from DOMINO is generally higher than stratospheric NO<sub>2</sub> from the Standard Product, more so in January than in July 2005. The Figure also shows that the bias between the two retrievals is not uniform, but reveals large, synoptic-scale spatial features. Such differences have been reported earlier by *Lamsal et al.* [2010], who found DOMINO and SP stratospheric slant columns to agree within  $\pm 1 \times 10^{15}$  molecules/cm<sup>2</sup>. The stratospheric NO<sub>2</sub> field retrieved from SCIAMACHY limb measurements [*Beirle et al.*, 2010] shows considerable longitudinal variation at mid-latitudes, which is similar to the zonal variations in DOMINO stratospheric NO<sub>2</sub>. This indicates that the synoptic-scale spatial features in the difference between DOMINO and SP stratospheric NO<sub>2</sub> result from the SP not properly capturing the longitudinal variation in the stratospheric NO<sub>2</sub> field. Here we examine the origin of the differences between DOMINO and SP

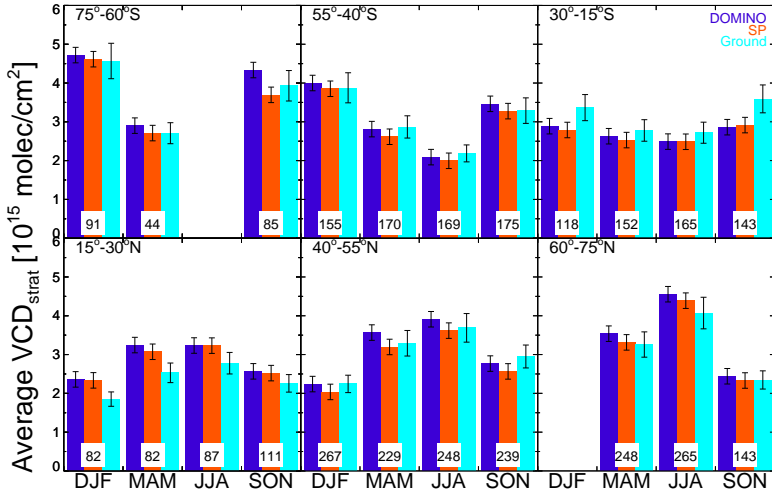


**Figure 4.5** Comparison of DOMINO (blue), SP (red), and ground-based (cyan) stratospheric NO<sub>2</sub> observations as a function of season in 2005. Coincident and collocated (< 10 km) OMI measurement data were adjusted to local noon. For days with multiple OMI overpasses, the overpass closest to local noon was selected. The numbers in the bars represent the number of ground-based observations contributing to the plot. The error bars give an indication of the measurement precision ( $0.1 \times 10^{15}$  molecules/cm<sup>2</sup> for DOMINO and SP, 10% for the ground-based data). Bauru (22.3°S) data between 15 September-31 January have been excluded because these are affected by high tropospheric NO<sub>2</sub> concentrations from biomass burning.

**Table 4.2** Overview of algorithm differences between OMI DOMINO and OMI SP.

algorithm	stripe correction	RTM	albedo		stratospheric column	profile shape
			λ (nm)	source		
DOMINO	No	DAK	440	TOMS-GOME	TM4 assimilation	TM4
SP	Yes	TOMRAD	440	GOME	wave-2 fit	Climatology of GEOS-Chem & GSFC CTM

stratospheric NO<sub>2</sub>, by comparing the stratospheric AMFs of both algorithms. The middle panel of Figure 4.7 clearly shows that DOMINO AMFs are smaller than those from the SP, especially at large solar zenith angles. This is supported by the comparison between stratospheric AMFs near the equator shown in Figure 4.8. For this particular part of the orbit, we find discrepancies between DOMINO and SP AMFs on the order of 5% with a notable increase around viewing zenith angles of

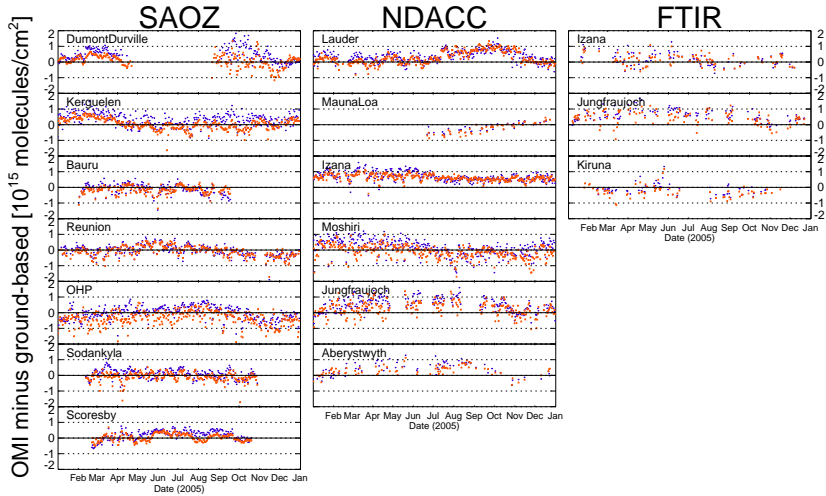


**Figure 4.6** Differences between OMI stratospheric NO<sub>2</sub> columns and ground-based observations for various stations in 2005. Blue symbols indicate the differences between DOMINO and ground-based stratospheric NO<sub>2</sub>, red symbols represent SP minus ground-based. Only satellite observations within 10 km of the ground-based station have been selected, and ground-based and satellite data have been adjusted to 12h00 local time. In case of multiple OMI overpasses per day, the overpass closest to local noon was selected.

45°. Investigation of the look-up tables of the DOMINO and SP revealed that the latter has reference points for VZA=0°, 30°, 45° & 70°, indicating that the large discrepancy for VZAs between 45° and 70° is most likely due to interpolation errors in the SP look-up table. In future versions, the SP look-up table will use more reference points to resolve this issue. The systematic discrepancy of approximately 5% between the AMFs for VZA < 45° result from differences in the AMF calculation between the DOMINO and SP algorithm. Table 4.2 gives an overview of all differences between both algorithms. Different NO<sub>2</sub> profile shapes (DOMINO profiles are taken from TM4 assimilation whereas Standard Product profiles are derived from merged GSFC CTM and GEOS-Chem simulations) accounts for a 1-2% difference between the DOMINO stratospheric AMF and AMF<sub>init,SP</sub>. Similarly, the correction for the temperature sensitivity of the NO<sub>2</sub> spectrum discussed in Section 4.2.2 will introduce differences as DOMINO uses ECMWF temperature profiles whereas SP uses climatological profiles. The different radiative transfer models used for the AMF calculation (DAK in case of DOMINO and TOMRAD for SP) account for another 1-2% difference in the AMFs. Both models assume plane-parallel atmospheres, however TOMRAD includes a correction for atmospheric sphericity while DAK includes polarization [Stammes *et al.*, 1989].

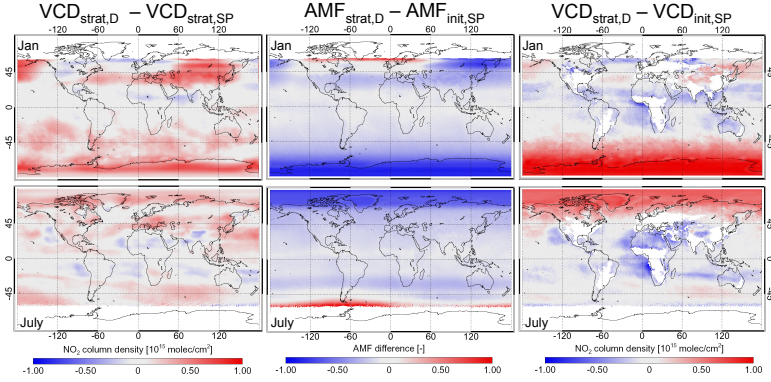


**Figure 4.7** Comparison between DOMINO and Standard Product (SP) retrievals of stratospheric  $\text{NO}_2$  for January 2005 (upper row) and July 2005 (bottom row). The left column shows the monthly mean difference  $\text{VCD}_{\text{strat,D}} - \text{VCD}_{\text{strat,SP}}$ , the center column shows  $\text{AMF}_{\text{strat,D}} - \text{AMF}_{\text{init,SP}}$ , and the right column shows  $\text{VCD}_{\text{strat,D}} - \text{VCD}_{\text{init,SP}}$ . In the right column regions with high tropospheric  $\text{NO}_2$  concentrations ( $> 1 \times 10^{15}$  molecules  $\text{cm}^{-2}$  in annual mean DOMINO) are masked.

The right panels of Figure 4.7 show the impact of the AMF differences alone. The DOMINO stratospheric columns deviate more strongly from the SP initial vertical columns ( $\text{VCD}_{\text{init,SP}}$ ) than the ultimately reported (wave-2 processed) SP stratospheric columns. Apparently, masking out polluted areas, accounting for tropospheric contributions to  $\text{VCD}_{\text{init,SP}}$ , and the wave-2 processing itself, compensate to some extent for the higher SP AMFs, as indicated by the smaller differences between DOMINO and SP stratospheric  $\text{NO}_2$  columns than between DOMINO  $\text{VCD}_{\text{strat,D}}$  and SP  $\text{VCD}_{\text{init,SP}}$  in the left panel of Figure 4.7.

#### 4.6 Day-to-day dynamical effects

The Arctic polar vortex of the 2004-2005 winter was dynamically active with various excursions to lower latitudes between January and March [Singleton *et al.*, 2007]. A major stratospheric warming in mid-March caused the final breakup of the vortex [Manney *et al.*, 2006, Singleton *et al.*, 2007].

Figure 4.9 shows the dynamic behavior of the polar vortex in the period from 9 to 21 March 2005. The PV and temperature at 50 hPa (third and fourth column of Figure 4.9, respectively) show that until 14 March the polar vortex appears stationary over the north Atlantic. On 17 March the vortex has tilted in East-West direction, after which it collapsed and broke up as seen on the 21st.

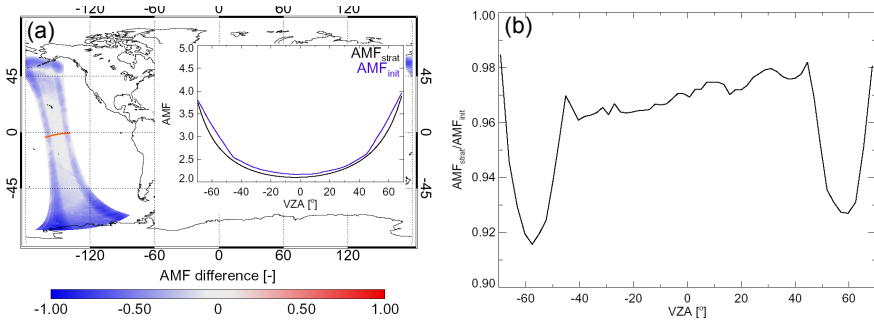


**Figure 4.8** Comparison between stratospheric air mass factors (AMF) between DOMINO and Standard Product (SP) retrievals of stratospheric NO<sub>2</sub> on 23 January 2005. (a) shows  $AMF_{strat,D} - AMF_{init,SP}$  for OMI orbit 2806 over the Pacific. The inset shows for a single OMI measurement the variation of  $AMF_{strat,D}$  and  $AMF_{init,SP}$  as a function of viewing zenith angle (VZA). The red line marks the location of the selected OMI measurement. (b) shows the  $AMF_{strat,D} / AMF_{init,SP}$  as a function of VZA. The negative viewing zenith angles correspond to the western part of the swath.

The stratospheric NO<sub>2</sub> profile peaks between 30-50 hPa, and therefore we expect good spatial correlation between the DOMINO stratospheric NO<sub>2</sub> field (left column of Figure 4.9) and the temperature distribution at 50 hPa (middle column of Figure 4.9). During 9-14 March OMI observes reduced stratospheric NO<sub>2</sub> columns inside the vortex over the North Atlantic and Greenland and enhanced NO<sub>2</sub> over Siberia and southern Europe. The boundary between reduced and enhanced stratospheric NO<sub>2</sub> roughly coincides with the  $-65^{\circ}\text{C}$  contour at 50 hPa. On 17 March, the reduced NO<sub>2</sub> columns over Great Britain coincide with the low temperatures inside the tilted and weakening vortex.

The synoptic-scale variations in the stratospheric NO<sub>2</sub> field around the vortex are not observed by the Standard Product (second column of Figure 4.9), but are smoothed by the wave-2 fitting instead. Actually, the enhanced stratospheric NO<sub>2</sub> at the vortex edge shows up as a reduction in the SP NO<sub>2</sub>, probably resulting from the masking of polluted areas.

We now focus on the effect of the movement of the vortex edge on stratospheric NO<sub>2</sub> over Sodankyla. Temperature and PV at 50 hPa show that on 9 March Sodankyla is inside the vortex, close to its edge and the warmer air mass with enhanced stratospheric NO<sub>2</sub> outside the vortex. The westward displacement of the vortex on 12 March moves NO<sub>2</sub>-rich air over Sodankyla, which results in an episodic enhancement of the stratospheric NO<sub>2</sub> columns of more than  $1 \times 10^{15}$  molecules/cm<sup>2</sup>. Figure 4.10 shows DOMINO and FTIR observations over Sodankyla and Jungfraujoch of this episodic enhancement, that peaks on 14 March and lasts approximately 7 days.

Figure 4.10 shows that the stratospheric NO<sub>2</sub> column over Sodankyla is coupled to

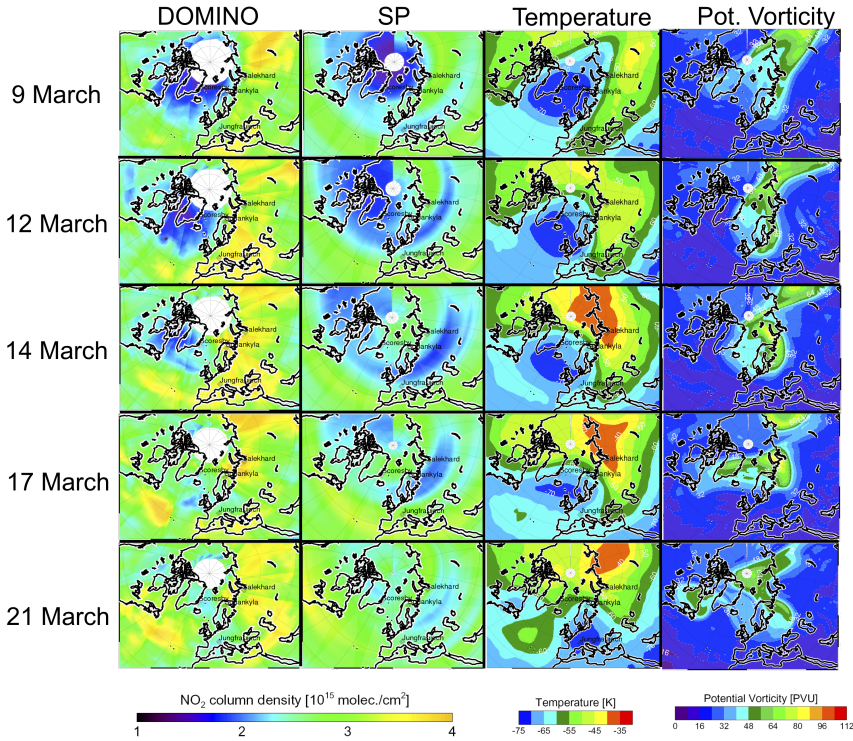


**Figure 4.9** Time series (9, 12, 14, 17, and 21 March 2005) of polar vortex dynamics. Left columns represent stratospheric  $\text{NO}_2$  fields from DOMINO and SP at local time of approximately 13h30. Third and fourth columns indicate the temperature and potential vorticity at 50 hPa (12h00 UTC) from ECWMF (ERA interim model version 1, analysis data).

the temperature at 30 hPa. The persistent low temperatures ( $T \approx -80^\circ\text{C}$ ) at 30 hPa in the first half of February coincide with low and unchanging FTIR-observed  $\text{NO}_2$  columns (approximately  $1 \times 10^{15}$  molecules/ $\text{cm}^2$ ). After 21 February the stratospheric  $\text{NO}_2$  column increases steadily in accordance with the increasing temperature, and the episodic enhancement of stratospheric  $\text{NO}_2$  around 15 March correlates with a sudden increase in the 30 hPa temperature over Sodankyla. Such positive correlations between short term changes and local stratospheric temperature have been observed before [Mount *et al.*, 1987, Pommereau and Goutail, 1988]. We find a temperature dependence of  $d\text{NO}_2/dT = 7 \times 10^{13}$  molecules/ $\text{cm}^2/\text{K}$  ( $r=0.95$ ), which is consistent with the  $6 \times 10^{13}$  molecules/ $\text{cm}^2/\text{K}$  over Kiruna reported by Pommereau and Goutail [1988]. It is unlikely that the observed temperature dependence of the stratospheric  $\text{NO}_2$  column results from the temperature sensitivity of the  $\text{NO}_2$



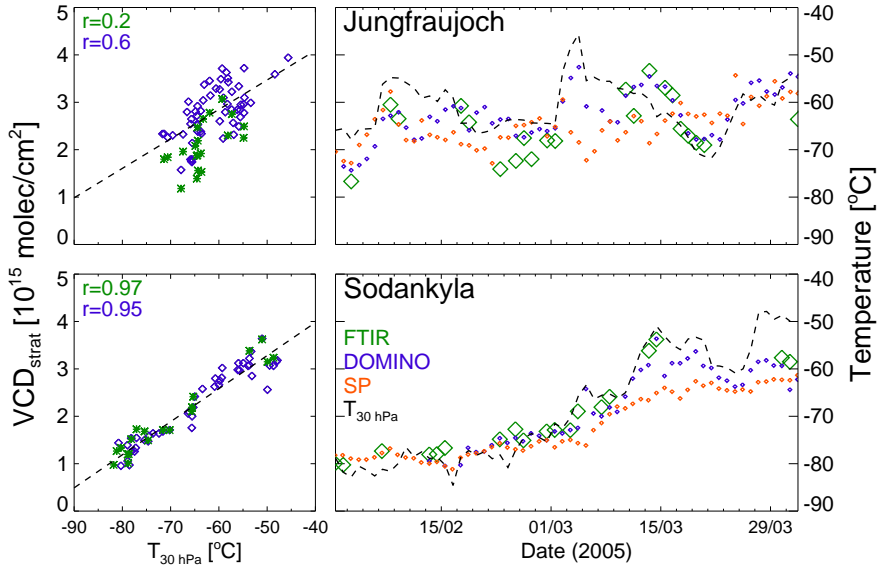


**Figure 4.10** Right column: time series of ground-based and collocated OMI observations of stratospheric NO<sub>2</sub> column over Jungfraujoch (top) and Sodankyla (bottom). OMI pixels within a 10 km radius of the ground station were selected. For multiple overpasses the OMI measurement closest to 13h00 local time was used. Shown are ground-based FTIR (green diamonds), together with OMI DOMINO (blue) and OMI Standard Product (red) stratospheric NO<sub>2</sub> columns. The Jungfraujoch FTIR measurements were adjusted (factor:+1.23, offset:-0.125) to correct for the mismatch between FTIR and DOMINO as shown in Figure 4.4. The dashed line represents the ECMWF temperature at 30 hPa. The left column shows scatterplots of FTIR (green) and DOMINO (blue) stratospheric NO<sub>2</sub> columns versus temperature. The dashed line in the insets represents a linear fit of the stratospheric NO<sub>2</sub> to the temperature data.

absorption cross section in the spectral fitting. First of all, the DOMINO retrieval takes this sensitivity into account (see Section 4.2.2). Furthermore, if this sensitivity were to be neglected, it is much weaker and different in sign (-0.3%/K) than the effect we find here (+3.5%/K over Kiruna). We attribute the coupling between temperature and stratospheric NO<sub>2</sub> to the temperature dependence of the N<sub>2</sub>O<sub>5</sub> (photo)dissociation rate and the NO/NO<sub>2</sub> partitioning, as proposed by Van Roozendael *et al.* [1994]. The weaker correlation between temperature and stratospheric NO<sub>2</sub> column over Jungfraujoch (upper panel of Figure 4.10) most likely results from stronger stratospheric dynamics at this location.

During the cold winter of 2004-2005, over a large area the stratospheric temperatures fell below the formation temperature of polar stratospheric clouds (PSC), resulting in increased ozone loss in the Arctic stratosphere [Singleton *et al.*, 2007].

However, after 21 February the stratospheric NO<sub>2</sub> column over Sodankyla, which lies inside the vortex until 11 March, increases steadily with the rising temperature at 30 hPa. This implies that the N<sub>2</sub>O<sub>5</sub> and HNO<sub>3</sub> reservoirs in the vortex air over Sodankyla are not depleted by denitrification and subsequent sedimentation, but are still present to be (photolytically) converted into NO<sub>x</sub>.

Figure 4.10 shows that the Standard Product reproduces the seasonal trend of the stratospheric NO<sub>2</sub> but does not capture the short-term increases associated with the vortex displacement. This is also shown by the sequence of SP stratospheric NO<sub>2</sub> plots in Figure 4.9 (second column). The lower panel in Figure 4.10 shows that the discrepancy between DOMINO and SP stratospheric NO<sub>2</sub> in case of large gradients in the stratospheric NO<sub>2</sub> field can be as large as  $1 \times 10^{15}$  molecules/cm<sup>2</sup>.

#### 4.7 OMI observations of the diurnal variation of stratospheric NO<sub>2</sub>

As a result of OMI's 2600 km wide swath, consecutive orbits start to overlap poleward of 30° latitude. The overlap increases with increasing latitude and results in up to 4 OMI overpasses per day at the same ground location near the arctic circle. The number of overpasses is even higher for regions in midnight Sun when OMI observations are also possible during the descending part ("night-side") of the orbit. For instance, Scoresby (70.5°N) can have as much as 7 OMI overpasses in summer. Therefore, OMI is able to sample the diurnal variation of stratospheric NO<sub>2</sub> from space with an interval of 100 minutes. Initial attempts to observing the diurnal variation of stratospheric NO<sub>2</sub> from space made use of climatological data [Sassi and Salby, 1999, Brohede et al., 2007]. Here we report for the first time on the direct observation of the diurnal variation in stratospheric NO<sub>2</sub> columns. Figure 4.11 (a) shows the diurnal variation of DOMINO stratospheric NO<sub>2</sub> over Scoresby on individual days between 9 March and 8 October 2005. With the exception of very early measurements in June and July, stratospheric NO<sub>2</sub> increases quasi-linearly during the day. The number of daily overpasses increases from winter to summer as a result of the increasing number of sunlit hours with season. The slope of the curves in Figure 4.11 (a) indicates that the increase rate of stratospheric NO<sub>2</sub> is larger in spring and fall than during summer. The low increase rate in summer results from the depletion of the N<sub>2</sub>O<sub>5</sub> reservoir by photo-dissociation during the long sunlit hours, while the nights are too short to replenish the reservoir. The DOMINO stratospheric NO<sub>2</sub> column over Scoresby in June-July (represented by the light and dark green lines in Figure 4.11 (a)) decreases before 10h00 LT (OMI measurements from descending part of the orbit), and increases quasi-linearly after 10h00 LT (OMI measurements from ascending part of the orbit). We hypothesize that the early-morning decrease is caused by the rising Sun, shifting the NO-NO<sub>2</sub> partitioning towards NO. The observed early-morning decrease and consecutive increase after 10h00 LT is consistent with SLIMCAT-based box-model simulations

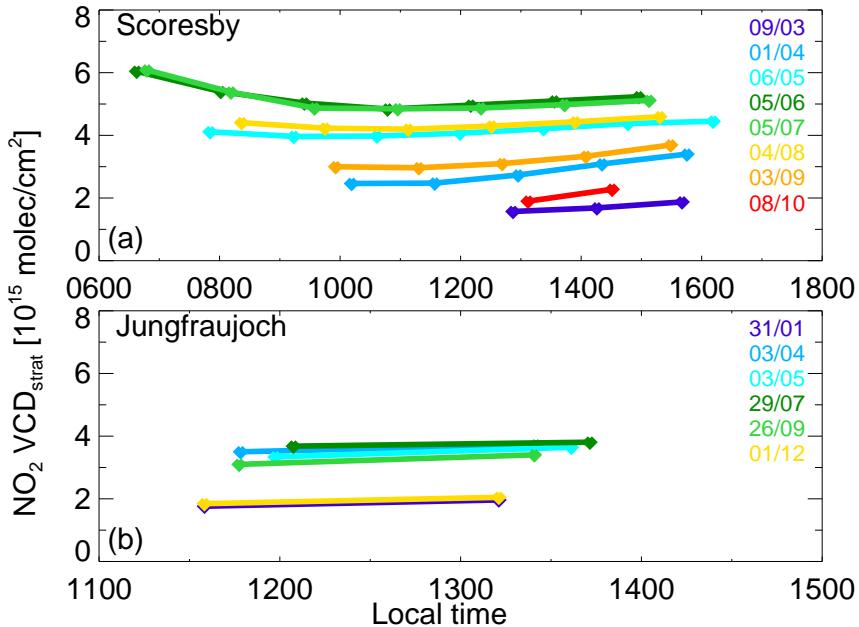


**Figure 4.11** OMI stratospheric NO<sub>2</sub> column over (a) Scoresby (70.5°N, 22°W) and (b) Jungfraujoch (46.5°N, 8°E) as a function of local time of observation. The colors refer to the day and month of observation.

(see e.g., Figure 2 in *Celarier et al.* [2008]). For comparison, Figure 4.11 (b) shows the diurnal variation of DOMINO stratospheric NO<sub>2</sub> over Jungfraujoch. Because of its lower latitude (46.5°N), Jungfraujoch has at most two OMI overpasses per day. Apart from the seasonal increase in stratospheric NO<sub>2</sub>, we find that the increase rate is more constant throughout the year compared to the high-latitude sites. The weaker seasonal dependence of the increase rate is caused by the longer nights that allow for the replenishing of N<sub>2</sub>O<sub>5</sub>.

Figure 4.12 shows the OMI-inferred (a) and SAOZ-inferred (b) linear increase rate of stratospheric NO<sub>2</sub> for Scoresby and other high-latitude SAOZ stations. The linear increase rates of stratospheric NO<sub>2</sub> for these high-latitude sites both show a distinct seasonal dependence, with strongest increases in spring and fall, reflecting the formation of N<sub>2</sub>O<sub>5</sub> during the night in those seasons.

The increase rate is determined by a linear fit to OMI stratospheric NO<sub>2</sub> (forecast based on assimilation) of consecutive overpasses after 10h00 LT. We also determined the increase rate using the measured slant columns divided by the geometric air

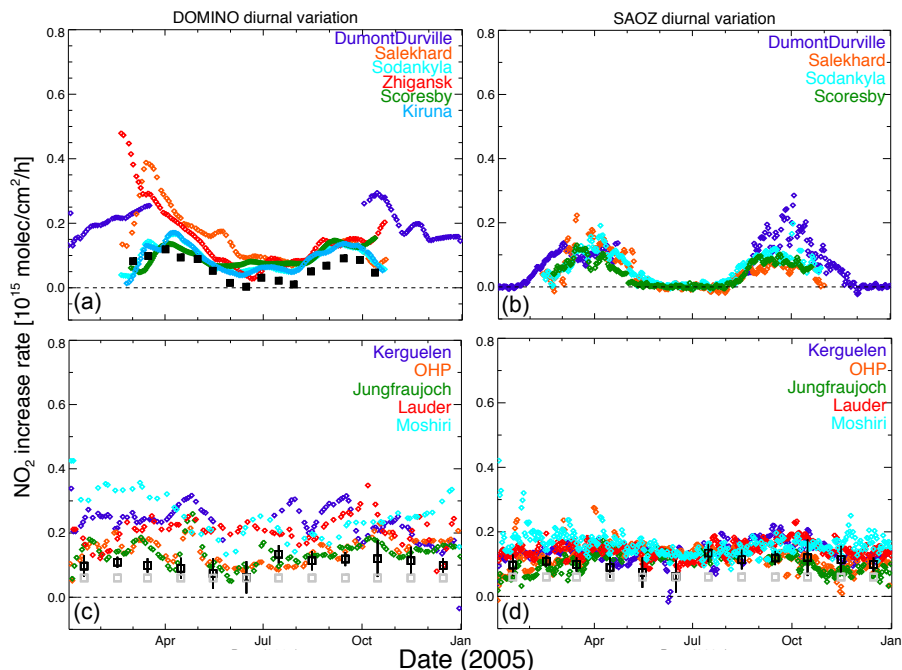


**Figure 4.12** Increase rate of stratospheric  $\text{NO}_2$  as a function of month for (a) seasonal variation in the increase rate of the DOMINO stratospheric  $\text{NO}_2$  column over high-latitude stations with 3 or more daily overpasses. (b) Linear increase rate for high-latitude stations derived from sunrise and sunset SAOZ measurements. (c) same as (a) for mid-latitude stations with two or more daily overpasses. (d) same as (b) for mid-latitude stations. The OMI increase rate follows from a linear fit to the observations performed during the ascending part (when the spacecraft flies northwards) of consecutive orbits. Curves in (a) and (c) were smoothed by a 9-point median filter followed by 15-day averaging, curves in (b) and (d) were smoothed by 3-day averaging. The filled boxes in (a) represent the increase rate derived from OMI  $\text{NO}_2$  slant column observations over Kiruna. The black boxes in (c) and (d) represent the increase rate measured by FTIR at Zugspitze, data taken from Figure 3(b) in Sussmann et al. [2005]. The grey boxes in (c) and (d) represent the annual mean increase rate at Izaña [Gil et al., 2008]. In the plots OMI pixels within 100 km of the measurement site were used.

mass factor. The resulting increase rates were very similar to the results presented in Figure 4.12 (a), suggesting that the increase rates reported here do not result from the assimilation, but are actually observed.

At high latitudes, in spring and fall the increase rate is approximately  $0.2 \times 10^{15}$  molecules/cm<sup>2</sup>/h and drops to  $0.05$ - $0.1 \times 10^{15}$  molecules/cm<sup>2</sup>/h in summer. For Salekhard and Zhigansk (orange and red data points) the OMI-inferred increase rate in

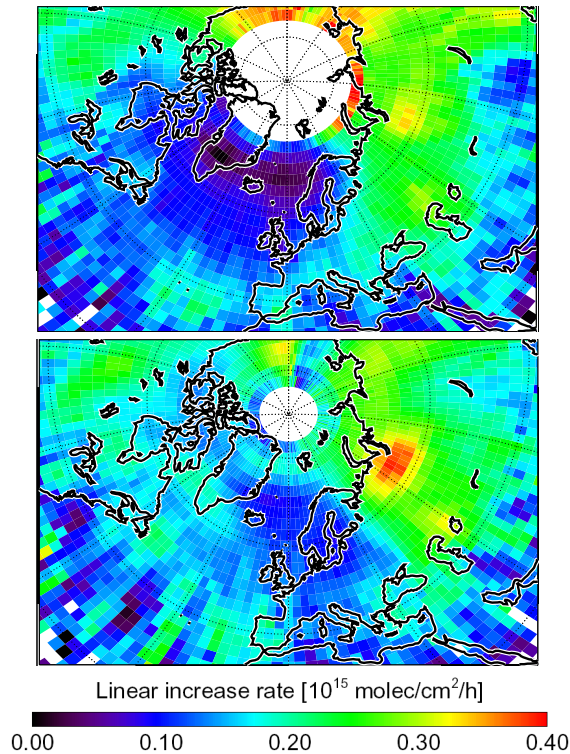


**Figure 4.13** Average diurnal linear increase rate of DOMINO stratospheric NO<sub>2</sub> columns for the Northern Hemisphere for 1-15 March 2005 (upper panel) and 16-31 March 2005 (lower panel). The linear increase rate is calculated for locations with two or more OMI overpasses per day.

spring ( $0.4 \times 10^{15}$  molecules/cm<sup>2</sup>/h) is considerably higher than in fall ( $0.15 \times 10^{15}$  molecules/cm<sup>2</sup>/h). This asymmetry between spring and fall is likely caused by the collar of NO<sub>y</sub>-rich (and warmer) air, which girds the Arctic polar vortex, that lies over Salekhard and Zhigansk in spring. In fall, the vortex and its surrounding collar are absent. The position and movement of the Arctic polar vortex in spring 2005 was discussed in Section 4.6. The seasonal dependence of the increase rate derived from SAOZ measurements (Figure 4.12 (b)) is similar to DOMINO, with a maximum in spring and fall, and a minimum in summer. SAOZ-inferred increase rates over Salekhard also indicate a higher increase rate in spring than in fall. During summer, SAOZ-derived increase rates for high-latitude sites are close to 0, which is consistent with the identical morning and evening SAOZ NO<sub>2</sub> columns over Sodankyla

in summer reported by *Goutail et al.* [1994]. For mid-latitudes, the OMI-derived increase rates (Figure 4.12 (c)) are similar to those derived from SAOZ (Figure 4.12 (d)), with weak seasonal dependence. The OMI and SAOZ-inferred increase rates over Jungfraujoch are comparable to the annual mean increase rate of  $0.1 \times 10^{15}$  molecules/cm<sup>2</sup>/h reported for Zugspitze [*Sussmann et al.*, 2005]. For comparison, *Gil et al.* [2008], reported an annual mean increase of  $0.06 \times 10^{15}$  molecules/cm<sup>2</sup>/h over Izaña (28.3°N).

Figure 4.13 shows a map of the mean linear increase rate of OMI stratospheric NO<sub>2</sub> for the Northern Hemisphere, derived for the first (upper panel) and second half (lower panel) of March 2005. The geographical distribution of the increase rate closely resembles the morphology of the stratospheric NO<sub>2</sub> that was presented in Figure 4.9: the region with low increase rates coincides with the low NO<sub>2</sub> values inside the denoxified polar vortex and we find high increase rates for the air outside the vortex that is rich in reactive nitrogen. The mid-March break-up of the polar vortex is reflected in the geographical distribution and the values of the increase rate for the second half of March (lower panel of Figure 4.13): the area with low increase rates has shrunk, and the value of the increase rates themselves has grown.

## 4.8 OMI observed trends stratospheric NO<sub>2</sub>

The DOMINO dataset covers more than five years (October 2004-May 2010) of global stratospheric and tropospheric NO<sub>2</sub> observations, which allows for the study of temporal variability on various timescales in stratospheric NO<sub>2</sub>.

### 4.8.1 Seasonal variation and QBO

Figure 4.14 shows a multi-year time series of zonally averaged DOMINO stratospheric NO<sub>2</sub> columns. Over the polar and mid-latitudes, stratospheric NO<sub>2</sub> shows a distinct annual cycle, that is related to the number of sunlit hours and peaks in summer. The annual cycle is strongest over the polar regions, because of wintertime denoxification in the polar night when stratospheric NO<sub>2</sub> is converted into the long-lived HNO<sub>3</sub> and N<sub>2</sub>O<sub>5</sub> reservoirs. The latitudes between 60°-90°S show reduced NO<sub>2</sub> columns in Antarctic spring (OND) as a result of denitrification inside the polar vortex during winter and early spring.

Figure 4.14 shows consistently higher summertime values of stratospheric NO<sub>2</sub> over the Antarctic in comparison to the Arctic. This interhemispheric asymmetry in the summertime stratospheric NO<sub>2</sub> columns has also been observed in GOME [*Wenig et al.*, 2004] and in ODIN/OSIRIS measurements [*Brohede et al.*, 2007]. *Solomon et al.* [1984] attribute this interhemispheric asymmetry to differences in the meridional circulation as the Southern Hemisphere exhibits much less planetary

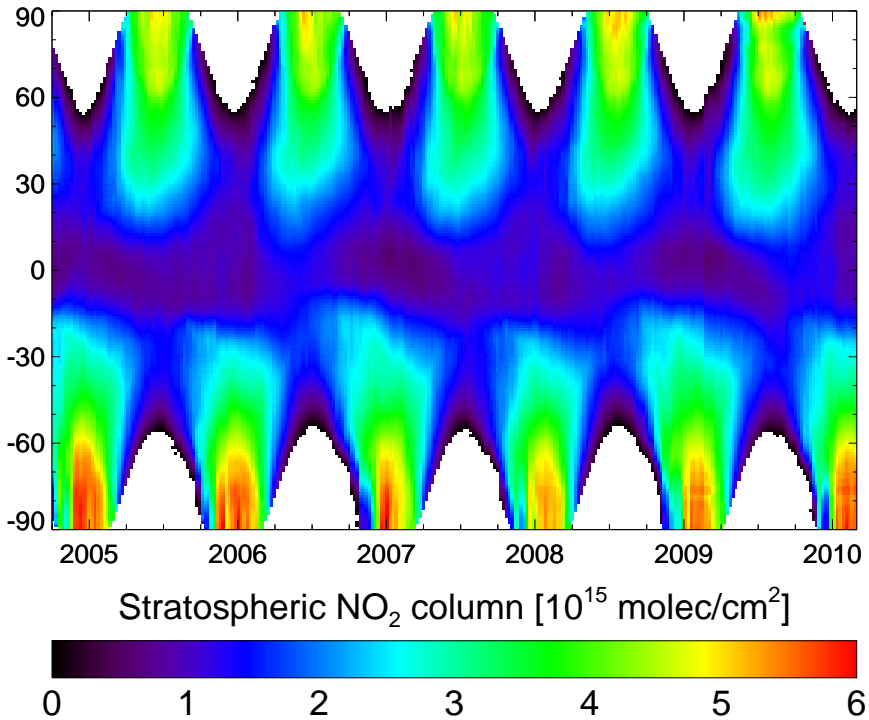


**Figure 4.14** Timeseries of zonal mean DOMINO stratospheric NO<sub>2</sub> columns as a function of latitude, spanning 1 October 2004 to 1 January 2010. Data are collected in seven-day bins and gridded to 1°x1°. The plot shows the zonal average in 1° wide latitude bands. The white regions poleward of 55° denote missing data because of the polar night.

wave activity than the Northern Hemisphere. The weaker planetary wave activity in the Southern Hemisphere should result in less efficient transport away from the pole. *Naudet et al.* [1987] suggested that the lower albedo (more ocean) at visible wavelengths and larger solar zenith angles in the Southern Hemisphere (resulting from the smaller Earth-Sun distance in Southern Hemisphere summer) lead to less photodissociation and thus higher concentrations of NO<sub>2</sub> in the stratosphere. Model calculations by [*Cook and Roscoe*, 2009] show that the NO<sub>x</sub> partitioning depends on temperature, with an increase of the modeled NO<sub>2</sub> vertical column of 0.5%/K. Therefore, it is likely that the higher summertime stratospheric NO<sub>2</sub> over Antarctica is also related to the Antarctic summer stratosphere is up to 8 K warmer than over the Arctic, owing to radiative (shorter Earth-Sun distance in January) and to

dynamical effects [Rosenlof, 1996, Siskind et al., 2003].

For mid-latitudes, we see a clear annual cycle in stratospheric NO<sub>2</sub>, with an amplitude of approximately  $1 \times 10^{15}$  molecules/cm<sup>2</sup>. At higher latitudes the seasonal cycle is stronger as a result of the denoxification in winter. In the tropics the amplitude of the seasonal cycle is comparable to the amplitude of semiannual harmonics that, as we will show later, results from the quasi-biennial oscillation (QBO, [Reed et al., 1961]). The weaker seasonal cycle in the tropics reflects the weak seasonal variation in the solar irradiation and the lower stratospheric NO<sub>2</sub> concentration. In the tropics, tropospheric air enters the stratosphere. During the poleward transport by the Brewer-Dobson circulation, N<sub>2</sub>O in this imported air is converted into NO<sub>y</sub> by the reaction with atomic oxygen. This leads to an increase of stratospheric NO<sub>2</sub> concentration with latitude and a build up of NO<sub>2</sub> in the polar regions.

The QBO is an oscillation in the equatorial zonal winds between 20 and 35 km altitude. The period of the oscillation ranges between 23 and 34 months, with a mean period of 28 months, hence the name quasi-biennial. The QBO in stratospheric ozone has been observed for many years [Funk and Garnham, 1962], but its effect was observed for the first time in stratospheric NO<sub>2</sub> by analysis of altitude-resolved SAGE II measurements [Zawodny and McCormick, 1991]. They attribute the NO<sub>2</sub>-QBO mainly to QBO-induced modulations in the vertical transport of NO<sub>y</sub> in the equatorial region, because changes in the NO<sub>x</sub> partitioning due to changes in observed temperature and ozone concentrations are insufficient to explain the NO<sub>2</sub>-QBO. Ground-based observations at mid- and high latitudes suggest that the NO<sub>2</sub>-QBO is not confined to the tropics: analysis of long-term measurement series reveals a correlation between the QBO cycle and variations in the overhead stratospheric NO<sub>2</sub> column at Lauder [Liley et al., 2000] and over Antarctica [Cook and Roscoe, 2009]. Liley et al. [2000] propose that the QBO affects stratospheric NO<sub>2</sub> outside the tropics "dynamically", by changing transport rates of relevant chemical species.

We now analyze the OMI NO<sub>2</sub> time series with the multilinear regression methods described by Zawodny and McCormick [1991], Liley et al. [2000] and Gruzdev and Elokhov [2009] in search of the QBO. The employed fitting model

$$y(t) = A_0 + \sum_{i=1}^3 \Gamma_i + A_4 t + A_5 I_{\text{QBO}}(t + \phi_{\text{QBO}}) + A_6 I_{\text{SI}}(t) + A_7 I_{\text{ENSO}}(t + \phi_{\text{ENSO}}) \quad (4.4)$$

contains background ( $A_0$ ) and linear trend ( $A_4 t$ ).  $\Gamma_i = A_i \sin(\frac{i2\pi t}{365.25}) + B_i \cos(\frac{i2\pi t}{365.25})$  are harmonic terms with 12, 6 and 4 month periodicity. The harmonic terms with 12 and 6 months periodicity describe the annual cycle and the asymmetry between the equinoctial periods, respectively. Additional index terms describe the QBO ( $I_{\text{QBO}}$ ), Solar Index ( $I_{\text{SI}}$ ) and El Niño Southern Oscillation ( $I_{\text{ENSO}}$ ).  $\phi_{\text{QBO}}$  and  $\phi_{\text{ENSO}}$  represent the phase (lag) of the QBO and of the ENSO terms, respectively.



**Table 4.3** Fitted trends in ground-based (middle column) and OMI (right column) stratospheric NO<sub>2</sub> over Lauder. The errors are estimated by varying the length of the fitting window with  $\pm 1$  year.

Period	Trend (%/decade)	
	Lauder	OMI
1981-1999	5.2( $\pm 0.5$ )	
1981-2010	5.2( $\pm 0.5$ )	
2004-2010	0.4( $\pm 2$ )	
2004-2010		0.6 ( $\pm 2$ )

The QBO index is given by the monthly mean of the zonally averaged equatorial winds at 30 hPa calculated by the NCEP/NCAR Climate Data Assimilation System (<http://www.cpc.ncep.noaa.gov/data/indices/qbo.u30.index>). The Solar Index  $I_{SI}$  is parameterized by the monthly means of the solar radio flux density at 10.7 cm ([ftp://ftp.ngdc.noaa.gov/STP/SOLAR\\_DATA/SOLAR\\_RADIO/FLUX/Penticton\\_Absolute/monthly](ftp://ftp.ngdc.noaa.gov/STP/SOLAR_DATA/SOLAR_RADIO/FLUX/Penticton_Absolute/monthly)). The ENSO index  $I_{ENSO}$  is based on the monthly mean sea level pressure difference between Tahiti and Darwin (<http://www.bom.gov.au/climate/current/soihtm1.shtml>).  $I_{QBO}$ ,  $I_{SI}$  and  $I_{ENSO}$  are scaled to  $[-1,+1]$ . Prior to applying the fitting model to the OMI data series, we tested our fitting procedure by reproducing the coefficients reported by *Liley et al.* [2000] for stratospheric NO<sub>2</sub> observed at NDACC station Lauder between 1981-1999. As shown in Table 4.3 we found a trend of +5.2( $\pm 0.5$ )% per decade, which is consistent with the +5% per decade reported by Liley. Similar to their approach we fixed the lag of the QBO and ENSO terms of 140 days and 13 months, respectively. Additional terms were used to account for the El Chichón (April 1982) and Pinatubo (June 1991) eruptions (see *Liley et al.* [2000] for details). The amplitude and lag of the QBO index are free parameters in the fit to the global OMI data set, SI and ENSO were not fitted because these parameters affect fitting stability at certain latitudes.

As a confidence check we also employed the fitting model of *Zawodny and McCormick* [1991] who parameterize the QBO by harmonics with 18, 24 and 30 month periodicity. These harmonic functions adequately parameterize the QBO index for the limited time range of the OMI data set, and this parameterization yields more stable fits than the tabulated monthly mean QBO index. The harmonic fitting model produces the same results as the fitting model based on *Liley et al.* [2000]. The fitting model, whose results are presented in Figure 4.15, shows that the ratio of the NO<sub>2</sub>-QBO and the annual term (green trace in Figure 4.15 (f)) peaks in the tropics with maxima located around 15°S and 5°N. The amplitude of the NO<sub>2</sub>-QBO in the tropics is comparable to the annual term, which is illustrated by Figure 4.15 (a), (b) and (e) and by Figure 4.14. The OMI time series show a clear interhemispheric asymmetry in the NO<sub>2</sub>-QBO: its peak value is nearly two times larger in the Southern Hemisphere than in the Northern Hemisphere. Furthermore the NO<sub>2</sub>-QBO peaks at

15°S in the Southern Hemisphere versus 5° in the Northern Hemisphere. This is illustrated by Figures 4.15 (a), (b), (d) and (e), showing the OMI time series for 5°S, 15°S, 5°N, and 15°N, respectively.

Other studies into the QBO such as *Zawodny and McCormick [1991]*, *Dunkerton [2001]* and *Randel and Wu [1996]*, usually report QBO anomalies that are equatorially symmetric in the tropics. However, these studies involve altitude resolved measurements of trace species, whereas OMI observes integrated stratospheric NO<sub>2</sub> columns. Integrated columns based on SAGE II measurements between 25-40 km also seem to suggest a stronger NO<sub>2</sub>-QBO in the southern tropics (Figure 7 of *Zawodny and McCormick [1991]*), the same is seen for integrated GOMOS-observed partial NO<sub>2</sub> columns between 20-50 km (Figure 21 of *Kyrölä et al. [2010]*).

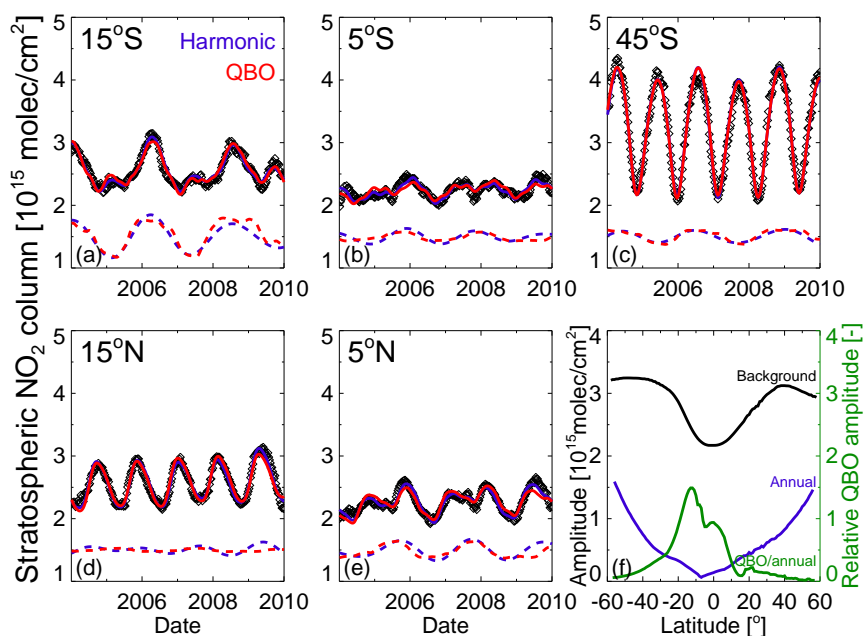


**Figure 4.15** (a)-(e) Time series of total mean OMI stratospheric NO<sub>2</sub> (black diamonds) and multilinear regression fit (solid line) to the data at selected latitudes. The red trace represents the fit with a model that parameterizes the QBO using the tabulated monthly mean QBO index, and the blue trace represents a fitting model that parameterizes the QBO with harmonic functions of 18, 24 and 30 month periodicity. The dashed lines represent the QBO-term in the resulting fit. (f) Background (black), annual (blue), and QBO fitting coefficients for the 2004-2010 OMI stratospheric NO<sub>2</sub> record as a function of latitude. The green trace shows the ratio of the QBO and the annual term (right y-axis).

#### 4.8.2 Long-term trends in stratospheric NO<sub>2</sub>

Figure 4.16 shows the agreement between collocated OMI stratospheric NO<sub>2</sub> data and the 1981-2010 time series of ground-based stratospheric NO<sub>2</sub> columns measured at Lauder at sunrise. OMI generally reproduces the values of the summer maxima and their year-to-year variability. This shows the potential of instruments such as OMI, and presumably also GOME and SCIAMACHY, to contribute to observing trends in stratospheric NO<sub>2</sub> from space, provided that the data record is of sufficient length.

For the 1981-1999 period *Liley et al.* [2000] report a 5.3% per decade increase in stratospheric NO<sub>2</sub>, which is twice the well-known 2.5% per decade increase rate of tropospheric N<sub>2</sub>O [WMO (*World Meteorological Organisation*), 2007]. This increase remains unchanged when the Lauder data record is extended to 2010. As shown in Table 4.3, this trend in stratospheric NO<sub>2</sub> over Lauder cannot be reproduced by OMI because of the short time period with measurements. For the time span of the OMI mission (2004-2010) the Lauder data yields an increase of 0.4(±2)% per decade, which is similar to the 0.6(±2)% per decade increase of stratospheric NO<sub>2</sub> derived from the OMI data over Lauder. For instance, for 1995-2010 we find a trend of +3.0 (±1)% per decade, showing that a 15-year period is also too short to reproduce the trend observed in Lauder between 1981 and 1999 (and 1981-2010).

This dependence of the trend on the period considered has also been reported by *Cook and Roscoe* [2009], who found little or no trend in NO<sub>2</sub> over Antarctica between 1990 and 2007 (1±4% per decade), and reported different trends for 1990-2000 (+11% per decade) and for 2000-2007 (-21% per decade). This indicates that in addition to the increase of N<sub>2</sub>O, additional factors influence the trend in stratospheric NO<sub>2</sub>. *Cook and Roscoe* [2009] found correlations between the annual variability in the summer maxima of stratospheric NO<sub>2</sub> over Antarctica and QBO, ENSO and Solar activity, but these factors still leave a considerable part of the observed annual variability unexplained. In contrast to the findings of *Cook and Roscoe* [2009], *Liley et al.* [2000] found no correlation between the Solar activity and the annual variability of stratospheric NO<sub>2</sub>. *Gruzdev and Elokhov* [2009] estimated the latitudinal dependence of the stratospheric NO<sub>2</sub> trend from ground-based measurements. Save a few exceptions, the employed data records cover an observational period of 10 years or longer.

This dependence of the trend on the period considered has also been reported by *Cook and Roscoe* [2009], who suggested that in addition to the increase in N<sub>2</sub>O, additional factors influence the trend in stratospheric NO<sub>2</sub> on timescales less than 15 years.

They reported predominantly positive trends, up to +10% per decade, for the Southern Hemisphere. For the Northern Hemisphere trends of similar magnitude but with positive and negative sign were found. There is considerable scatter in the trends reported by *Gruzdev and Elokhov* [2009] which illustrates the sensitivity of

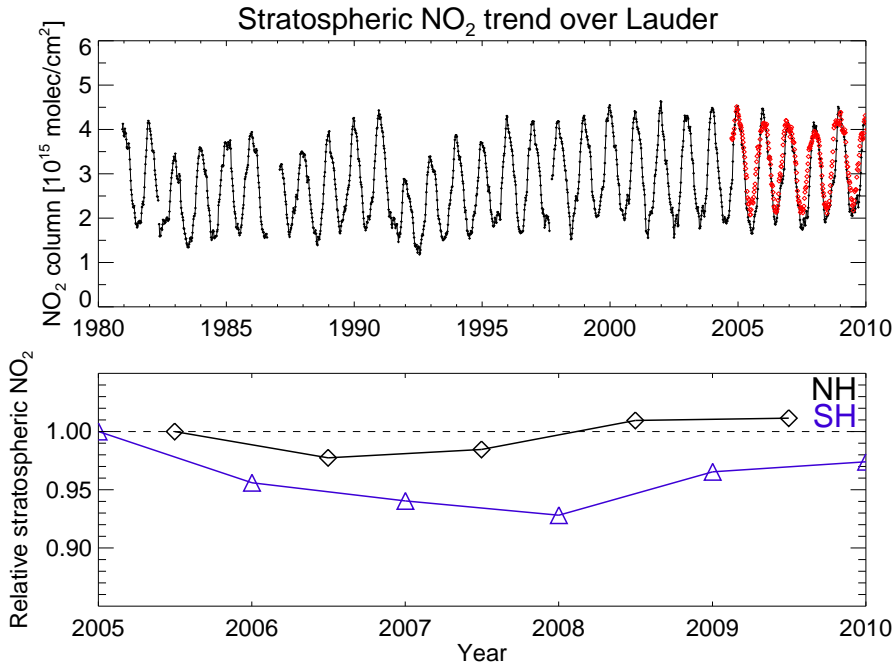


**Figure 4.16** Upper panel: Time series of sunrise stratospheric NO<sub>2</sub> columns measured at Lauder (black) and collocated DOMINO stratospheric NO<sub>2</sub> columns (red diamonds). Data were averaged in 7-day bins and a three point wide running average filter was applied. The Lauder data was downloaded from <ftp://ftp.cpc.ncep.noaa.gov/ndacc/station/lauder/ames/uvvis/>. Lower panel: multi-year trend of the summer maximum of the hemispheric average of DOMINO stratospheric NO<sub>2</sub>. Zonal average data between 40° and 85° latitude were used. Latitudes below 40° were excluded to rule out the QBO. The summer maxima are indexed with respect to the 2005 summer value. The dashed black line serves to guide the eye.

the trendfitting to the length of the time series.

The linear trend in OMI stratospheric NO<sub>2</sub> at various latitudes was fitted as part of the NO<sub>2</sub>-QBO analysis, as described in Section 4.8 above. The 5+ years covered so far by the OMI mission are obviously too short a period to reliably distinguish long term trends from inter-annual variability. Nevertheless, we find indications for negative trends in the Southern Hemisphere and for positive trends in the Northern Hemisphere. This finding is consistent with the trend of the hemisphere-averaged summer maximum (lower panel of Figure 4.16). Over the Northern Hemisphere, the summer maximum is reduced by 3% in 2006, and rises afterwards to be 2% higher in

2009 than in 2005 (a net positive trend). On the Southern Hemisphere the summer maximum declines to reach a 7% reduction in 2008 in comparison with 2005, and recovers to 97% of the 2005 value in 2010 (a net negative trend). The variability of the hemisphere-averaged summer maximum is uncorrelated with the Solar activity that goes through a minimum in 2009. *Cook and Roscoe* [2009] found a considerable inter-annual variability in the summer maxima of stratospheric NO<sub>2</sub> over Antarctica that could not be accounted for by QBO and Solar activity, and concluded that other (unidentified) processes affect the long term variability of stratospheric NO<sub>2</sub>. Based on the OMI data record, the long-term variability in the Southern Hemisphere appears stronger and its trend appears to lag the trend in the Northern Hemisphere. The need for an extended data record, e.g., by including GOME and SCIAMACHY observations, is obvious to quantify the global trend in stratospheric NO<sub>2</sub> from space.

#### 4.9 Summary and Conclusions

We have presented stratospheric NO<sub>2</sub> columns obtained from OMI with a data assimilation approach that makes use of the TM4 chemistry transport model. For each OMI observation, we calculate the stratospheric NO<sub>2</sub> column from the TM4 forecast that is based on the analyzed model state. The assimilation of OMI NO<sub>2</sub> total columns in TM4 corrects the tendency of the stratospheric part of the model to diverge from the observations. The scheme is insensitive to tropospheric contributions, and results in a forecast model state that is generally within  $0.15 \times 10^{15}$  molecules/cm<sup>2</sup> of the analysis over remote areas where stratospheric NO<sub>2</sub> dominates the total column.

The evaluation of ground-based techniques for measuring stratospheric NO<sub>2</sub> shows that UV-Vis and FTIR retrievals are only consistent within 15-20%, casting some doubt on their usefulness as ‘ground-truthing’ for satellite retrievals. Lacking an alternative, we used ground-based UV-Vis and FTIR measurements from 13 mostly pristine locations in the world to validate the Dutch OMI NO<sub>2</sub> (DOMINO) retrieval (based on data assimilation) and the NASA GSFC Standard Product. OMI retrievals and ground-based estimates of stratospheric NO<sub>2</sub> columns agree on average within  $0.3 \times 10^{15}$  molecules/cm<sup>2</sup> (13%), comparable to the accuracy of the ground-based instruments.

Stratospheric NO<sub>2</sub> retrieved from the DOMINO retrieval on average exceeds the Standard Product by  $0.2 \times 10^{15}$  molecules/cm<sup>2</sup>, but on short spatial and timescales, larger biases occur (up to  $1 \times 10^{15}$  molecules/cm<sup>2</sup>). Synoptic-scale differences between the two retrievals are explained by differences in the stratospheric air mass factors, and by the spatial smoothing technique used in the Standard Product algorithm. Differences between stratospheric air mass factors can be as high as 8% for specific satellite viewing angles, partly because of interpolation errors in the Standard Product air mass factor look-up table that has only few reference viewing angles.

The considerable differences resulting from the air mass factors are dampened by the spatial smoothing (wave-2 fit) in the Standard Product.

The OMI data record runs from October 2004 onwards and at the moment of writing covers more than 5 years of measurements. This allows for the study of temporal variability in stratospheric NO<sub>2</sub> columns on various timescales. During Arctic winter, DOMINO retrievals show low stratospheric NO<sub>2</sub> concentrations within the Arctic polar vortex, and higher NO<sub>2</sub> in adjacent regions. The morphology of the stratospheric NO<sub>2</sub> field in the wider vortex area closely resembles the temperature distribution at 50 hPa. A study of day-to-day variability in stratospheric NO<sub>2</sub> shows that DOMINO captures the collapse of the polar vortex during late winter, corroborated by ground-based NO<sub>2</sub> observations over Sodankyla and Jungfraujoch. The early springtime stratospheric NO<sub>2</sub> columns correlate strongly with stratospheric (30-50 hPa) temperatures, reflecting the temperature dependence of the N<sub>2</sub>O<sub>5</sub> (photo)dissociation rate and of the NO/NO<sub>2</sub> partitioning.

Using the overlapping orbits poleward of 30° latitude, we find that it is possible to observe the diurnal variation in stratospheric NO<sub>2</sub> columns from space. At high latitudes (> 60°), the diurnal increase rate has a distinct seasonal dependence with a maximum in spring and fall, which is consistent with increase rates inferred from SAOZ measurements at sunrise and sunset. The low increase rates at high latitudes in summer are attributed to the near-depletion of stratospheric N<sub>2</sub>O<sub>5</sub>, resulting from the long sunlit hours. A map of OMI-derived increase rates shows that in late winter its geographical distribution follows the morphology of the stratospheric NO<sub>2</sub> field with low increase rates inside the denoxified Arctic polar vortex and high increase rates in the NO<sub>x</sub>-rich air outside the vortex.

We analyzed the 5+ year time series of DOMINO stratospheric NO<sub>2</sub> columns with a multilinear regression model that includes background, linear trend, and harmonic terms, as well as the quasi-biennial oscillation (QBO). The background and the annual terms are smallest over the tropics and increase gradually towards the poles. Our analysis shows that the QBO in stratospheric NO<sub>2</sub> over the tropics is comparable to the annual term, and stronger over the Southern Hemisphere than over the Northern Hemisphere. The ability to detect long-term trends in stratospheric NO<sub>2</sub>, possibly resulting from the well-known positive trend in its N<sub>2</sub>O source, with the relatively short OMI satellite data record is limited. Our regression model, when applied to the well-established data record for Lauder, reproduces the previously found +5% per decade in stratospheric NO<sub>2</sub> columns for the 1981-1999 period. This increase remains unchanged when extending the Lauder data record to 2010, but for shorter, more recent periods the derived trend strongly depends on the time range chosen. For the time span of the OMI mission (2004-2010) +0.4% per decade is found, consistent with the trend in collocated OMI stratospheric NO<sub>2</sub> observations over Lauder (+0.6% per decade). The good agreement between the Lauder data record and collocated DOMINO stratospheric NO<sub>2</sub> observations, as well as the first ever space-based observation of diurnal variation in stratospheric NO<sub>2</sub> columns, indicate

that OMI makes a valuable contribution to the study of stratospheric NO<sub>2</sub>. The issue of long-term trend detection from space deserves further examination; the current OMI data record should be extended with the stratospheric NO<sub>2</sub> columns from the GOME, SCIAMACHY, and GOME-2 measurements.

### *Acknowledgements*

I want to thank the following people for providing the data used in this study: Florence Goutail and Andrea Pazmiño for the SAOZ data, Karin Kreher for her assistance with the Lauder data, Michel Van Roozendael and Philippe Demoulin for reanalyzing the Jungfraujoch FTIR data, Thomas Blumenstock and Manuel Gil for the Izaña FTIR data. Peter Siegmund and Wim Verkleij are thanked for valuable discussions about dynamical processes in the stratosphere.

## **An aerosol boomerang: Rapid around-the-world transport of smoke from the December 2006 Australian forest fires observed from space**

### **Abstract**

We investigate rapid around-the-world transport of a smoke aerosol plume released by intense forest fires in southeastern Australia in December 2006. During the first half of December 2006, southeastern Australia suffered from severe drought and exceptionally high temperatures. On 14 December 2006, a passing cold front in combination with the intense heat from the fires causing pyro-convective lofting, injected a large mass of aerosol particles into the jet stream. We track the resulting aerosol plume using Aerosol Absorbing Index (AAI) observations from the Ozone Monitoring Instrument (OMI) and find that it circumnavigated the world in 12 days. Using observations from OMI and the CALIOP (Cloud-Aerosol Lidar with Orthogonal Polarization) spaceborne lidar, we show that the plume resided in the high troposphere at different stages of its evolution. In absence of CALIOP data, we explored OMI  $O_2-O_2$  pressures to obtain information on the aerosol plume height. Detailed radiative transfer calculations suggest that the current OMI  $O_2-O_2$  retrievals contain useful information on the altitude of the aerosol plume under specific conditions (high AAI, no clouds below). The observed two-dimensional evolution of the smoke aerosol plume and the vertical distribution of the plume detected by CALIOP is matched by simulations with the TM4 chemistry transport model for an injection height of 248 hPa ( $\approx 10$  km). Injection heights at the surface and at 540 hPa ( $\approx 5$  km) resulted in simulated vertical distributions that were 2-3 km too low relative to CALIOP observations, and showed less agreement with the AAI patterns. The high injection altitude of 10 km mimics the effect of pyro-convective lofting as the additional buoyancy from the intense fires is not accounted for in the model. TM4 simulations with an inert and a water soluble tracer reproduce the observed dilution of the plume and show

---

The contents of this chapter have been adopted from the paper by *Dirksen et al.* [2009], with minor modifications.



that the latter gives the best agreement with the observations, suggesting that the ultimate removal of the aerosol particles is by scavenging. To our knowledge, this is the first detailed study of around-the-world long-range transport of forest fire emissions in the extratropical Southern Hemisphere.

## 5.1 Introduction

In December 2006, southeastern Australia suffered from exceptionally intense forest fires. Although forest fires are common in Australia's hot summer months, this particular episode was being described by government officials as exceptional [e.g., [http://en.wikipedia.org/wiki/2006-07\\_Australian\\_bushfire\\_season](http://en.wikipedia.org/wiki/2006-07_Australian_bushfire_season)]. In this study we use three-dimensional (3-D) satellite observations of aerosols and clouds, and simulations with a global 3-D chemistry transport model (CTM) to examine the origin, long-range transport, and removal of an exceptionally persistent Australian biomass burning pollution plume in December 2006.

Biomass burning and forest fire emissions contribute significantly to atmospheric composition on regional and global scales. Emissions from fires contain a variety of chemically active trace gases that affect the oxidizing capacity of the troposphere and ultimately lead to the formation of tropospheric ozone. Another major component of fire emissions is aerosol, which has strong radiative effects, and serves as a site for heterogeneous chemistry impacting trace gas concentrations. The sensible heat produced by the fires often leads to convective lofting of emitted species to the free troposphere [Pickering *et al.*, 1996]. Once in the free troposphere the gases and aerosols can be transported over vast distances affecting the concentrations of trace substances in remote regions.

So far, few studies into long range transport of pollution in the extra-tropical Southern Hemisphere have been performed. These events are relatively rare due to few prominent sources. The first satellite observation of long range transport in the extra-tropical Southern Hemisphere was reported by Wenig *et al.* [2003], who described the transport of a NO<sub>2</sub> plume of anthropogenic origin from South Africa to Australia. Fromm *et al.* [2006] revealed that forest fires near Canberra (southeastern Australia) in 2003 injected smoke into the stratosphere. Studies of the long range transport of biomass burning pollution in the southern tropics showed that the majority of the pollutants end up circulating in large accumulation regions over the southern Atlantic and over the Indian ocean [Staudt *et al.*, 2002, Stein *et al.*, 2003, Edwards *et al.*, 2006]. Under favorable meteorological conditions, i.e., by the passage of a frontal system, air from these accumulation regions is flushed and subsequently transported eastward, traveling as far as the Pacific [Staudt *et al.*, 2002, Sinha *et al.*, 2004]. The fraction of the pollutants following this pathway, based on Figure 3 in Edwards *et al.* [2006], is estimated to be less than 10% of the total emission in South America and Africa. Boreal fires are also important sources, and inter-continental

transport of pollution from such fires has been reported on several occasions [Forster *et al.*, 2001, Spichtinger *et al.*, 2001, Damoah *et al.*, 2004].

Satellite measurements are particularly useful to study the evolution of pollution from fires. Herman *et al.* [1997] used the Absorbing Aerosol Index (AAI) for the first time to track aerosol plumes with satellite measurements. The recent availability of space borne remote sensing instruments such as the Ozone Monitoring Instrument (OMI) [Levelt *et al.*, 2006b] and the Cloud-Aerosol Lidar with Orthogonal Polarization (CALIOP) [Winker *et al.*, 2003] enables us to observe and evaluate the sources, 3-D long range transport and dissipation of biomass burning plumes. The global daily coverage of AAI measurements by OMI is elemental in following the evolution of rapidly moving pollution plumes as was previously demonstrated for the 2006 Australian forest fires by Torres *et al.* [2007]. CALIOP measurements provide information on the vertical distribution of the biomass burning plume. Here we also investigate the possibility, in absence of CALIOP measurements, to derive the aerosol plume height from OMI O<sub>2</sub>-O<sub>2</sub> retrievals.

Fire plumes can reach a wide range of altitudes. Labonne *et al.* [2007], employing CALIOP measurements to determine plume heights, states that the majority of biomass burning plumes remains in the mixing layer and only sporadically reaches the free troposphere. This relates to the fact that the majority of wild fires occur in high-pressure ("good-weather") conditions with corresponding thermal stability by subsidence [Kahn *et al.*, 2007]. Using MISR data, Kahn *et al.* [2008] showed that approximately 20% of fires over Alaska-Yukon inject smoke directly into the free troposphere and the tendency of CALIOP to predominantly observe boundary layer plumes is attributed to its narrow swath. Mazzoni *et al.* [2007] report the majority of the biomass burning plumes over North America to reside in the lower troposphere between 2 and 3 km altitude. Detailed studies of summertime fires in northern Canada showed that under favorable meteorological conditions, i.e., an unstable atmosphere, pyro-convection can quickly loft forest fire smoke to the upper troposphere or even into the lower stratosphere [Fromm and Servranckx, 2003]. The term pyro-convection refers to convection triggered by an intense heat source at the surface, e.g., forest fires. Plumes in the upper troposphere have a much longer lifetime than their lower tropospheric counterparts, because of prevailing low humidity and low temperatures that suppress scavenging, thereby augmenting the horizontal range over which they are transported. We will show here that the aerosol plume from the 14 December 2006 Australian forest fires was lofted by pyro-convection in an unstable atmosphere into the jet-stream and circumnavigated the world in 12 days. A comparable event was reported by Damoah *et al.* [2004] for a boreal fire plume; here we report for the first time on rapid circumnavigation by forest fire plumes of the Southern Hemisphere. As pointed out by Hyer *et al.* [2007], the effective injection height of fire emissions depends on both the energy of the fire and on the local meteorological conditions. Currently, CTMs ignore the energy of fire plumes, and biomass burning emissions are released in the lower model

levels [e.g., [Lavoué *et al.*, 2000, Colarco *et al.*, 2004]]. Consequently, lofting of the plume depends solely on meteorological conditions. We show that using appropriate injection heights is essential for simulation of the observed 3-D transport of the Australian aerosol plume.

## 5.2 Satellite observations and Transport Model

### 5.2.1 OMI

The Dutch-Finnish Ozone Monitoring Instrument (OMI) is a UV-Vis imaging spectrometer that records the backscattered radiance from the Earth's atmosphere in three spectral channels between 264-504 nm at an average spectral resolution of 0.5 nm. It combines a wide swath (2600 km) with high spatial resolution (24x13 km<sup>2</sup> at nadir). OMI is part of the EOS-Aura mission (launched July 2004) which is in a Sun-synchronous ascending node orbit that crosses the equator at 13h40m local time. In this study we use the OMI scientific data products AAI, cloud fraction and cloud pressure, and false color RGB images. A detailed description of OMI's scientific objectives is given in *Levelt et al.* [2006b], instrument details are available in *Dobber et al.* [2006].

### 5.2.2 OMI AAI

The Absorbing Aerosol Index (AAI) is a measure of the spectral slope of the atmospheric backscattered radiance in the UV as compared to the spectral slope of a pure molecular atmosphere described by Rayleigh scattering [*Herman et al.*, 1997]. The AAI is the positive part of the residue which is defined as

$$r_{\lambda_1, \lambda_2} = -100 \cdot \left\{ 10 \log \left( \frac{R_{\lambda_2}^{\text{meas}}}{R_{\lambda_1}^{\text{meas}}} \right) - 10 \log \left( \frac{R_{\lambda_2}^{\text{Ray}}}{R_{\lambda_1}^{\text{Ray}}} \right) \right\} \quad (5.1)$$

with  $\lambda_1, \lambda_2$  the wavelength pair used to calculate the residue,  $R_\lambda$  the reflectance at wavelength  $\lambda$ ,  $R^{\text{meas}}$  the measured reflectance, and  $R^{\text{Ray}}$  the calculated reflectance for a Rayleigh atmosphere. Here the surface albedo of the Rayleigh atmosphere is adjusted such that  $R_{\lambda_1}^{\text{Ray}} = R_{\lambda_1}^{\text{meas}}$ . To calculate  $R_{\lambda_2}^{\text{Ray}}$ , the surface albedo at  $\lambda_2$  is assumed to be equal to the surface albedo at  $\lambda_1$ .

Positive values of the residue denote the presence of UV absorbing particles. Clouds or scattering aerosols produce zero or negative residue values. Although the AAI does not represent one single aerosol property but rather depends on several properties [*de Graaf et al.*, 2005], its advantage is that it can detect aerosols over a wide variety of scenes, including bright surfaces and clouds. The AAI is a powerful

method for tracking aerosol plumes in satellite measurements, and it has been employed in various studies of the transport of aerosol plumes [Herman *et al.*, 1997, de Graaf *et al.*, 2005, Fromm *et al.*, 2005]. Here we use the AAI that is included in the OMI TOMS Ozone product [Bhartia and Wellemeyer, 2002]; the wavelength pair used to calculate the AAI is 331/360 nm. Ahn *et al.* [2008] successfully verified the consistency of OMI AAI with other aerosol products.

### 5.2.3 OMI RGB images

False color RGB images are constructed from the OMI data by integrating three 20 nm wide wavelength bands in the VIS channel centered at 360, 420 and 484 nm, the "B", "G" and "R" wavelength bands respectively. Kroon *et al.* [2008] describes the construction of the RGB images in detail and applied these in the validation of OMI's geolocation. The B wavelength band is close to the wavelength pair that is used for determining the AAI, so that UV-absorbing aerosols are well visible as a brown hue in the OMI RGB images.

### 5.2.4 OMI O<sub>2</sub>-O<sub>2</sub> data products

The OMI cloud retrieval algorithm uses the O<sub>2</sub>-O<sub>2</sub> absorption feature at 477 nm [Acarreta *et al.*, 2004]. The continuum reflectance of the scene is used to determine the effective cloud fraction  $c_{\text{eff}}$ . A DOAS (Differential Optical Absorption Spectroscopy) fit of the OMI reflectance spectrum between 460 and 490 nm is used to determine the slant column amount of O<sub>2</sub>-O<sub>2</sub>. This quantity represents the O<sub>2</sub>-O<sub>2</sub> column along the average photon path from the Sun through the atmosphere to the effective scattering pressure level, and back to the satellite instrument. Sneep *et al.* [2008] showed that over cloudy scenes, the effective scattering height is situated in the middle of the cloud. The O<sub>2</sub>-O<sub>2</sub> slant column, together with the viewing and solar geometry, is used to find the effective scattering pressure by means of a lookup table. The lookup table was produced using the DAK (Doubling Adding KNMI) radiative transfer model [de Haan *et al.*, 1987, Stammes, 2001]. Clouds are approximated as Lambertian surfaces with albedo 0.8. Light can also be reflected by aerosols, and the O<sub>2</sub>-O<sub>2</sub> algorithm, using the assumed cloud model, will retrieve an effective O<sub>2</sub>-O<sub>2</sub> pressure and  $c_{\text{eff}}$  for scenes with aerosols. The reflectance due to aerosols in the pixel is ascribed to a cloud with albedo 0.8, thus yielding a small value for the effective cloud fraction. The retrieved O<sub>2</sub>-O<sub>2</sub> cloud pressure belongs to this cloud fraction. OMI O<sub>2</sub>-O<sub>2</sub> cloud fractions have been validated successfully against MODIS-Aqua cloud observations [Stammes *et al.*, 2008], and OMI cloud pressures were generally within 100 hPa of PARASOL cloud pressures.

### 5.2.5 CALIOP/CALIPSO

The CALIPSO (Cloud-Aerosol Lidar and Infrared Pathfinder Satellite Observation) satellite carries a two-wavelength (532 and 1064 nm) lidar, named CALIOP (Cloud-Aerosol Lidar with Orthogonal Polarization), and uses backscattered lidar pulse to measure the vertical distribution of aerosols and clouds, with a horizontal resolution of 333 m along track and a vertical resolution of 30-60 m [Winker *et al.*, 2003]. Together with EOS-Aura, CALIPSO is part of the A-train, (<http://www-calipso.larc.nasa.gov/about/atrain.php>) a formation of five scientific platforms in near-identical orbits with 15 minutes separation between the leading and the trailing satellite. CALIPSO observes the same scene 5-10 minutes prior to OMI, albeit with a much narrower swath. McGill *et al.* [2007] reported good agreement between cloud top altitude determination by CALIOP and the airborne Cloud Physics Lidar (CPL). Kim *et al.* [2008] showed that in comparison with a ground based lidar CALIOP measurements of cloud top height agree within 0.1 km, and that CALIOP retrieval of aerosol vertical distributions agree well when not obscured by overlying clouds.

### 5.2.6 TM4

The Tracer Model version 4 (TM4) is a 3-D CTM based on the parent model TM3 (Dentener *et al.* [2003] and references therein). We conduct TM4 simulations with a spatial resolution of  $3^\circ \times 2^\circ$  and 34 sigma-pressure levels up to 0.1 hPa in the vertical direction. The model is driven by 6-hour (3-hour in the boundary layer) meteorological fields from 90-layer ECMWF operational analysis data. The transformation of the vorticity, divergence, and surface pressure fields in the spectral representation of the ECMWF model to the velocity and surface pressure fields on the regular model grid is performed using the method described by Segers *et al.* [2002]. Model transport of SF<sub>6</sub> in the troposphere has been evaluated with flask measurements showing good agreement [Peters *et al.*, 2004]. The latter study was performed with the successor of TM4, TM5, but the meteorological input data and transport scheme are identical between both model versions. Gloudemans *et al.* [2006] and de Laat *et al.* [2007] compared TM4 simulations of CO concentrations with CO measurements from SCIAMACHY, and found good agreement between the simulated and observed transport of CO, with the model bias most likely due to uncertainties in the emission database. In this study we focus on transport of biomass burning aerosols, here represented by a passive tracer with a molar mass similar to that of air. The location and amount of this biomass burning tracer emission were taken from version 2 of the Global Fire Emission Database (GFED-2) [van der Werf *et al.*, 2006]. GFED-2 provides monthly and 8-day means of biomass burning emissions on a  $1^\circ \times 1^\circ$  data-grid. For our relatively cloud-free study region, we scaled the monthly emissions to a daily

resolution using Terra and Aqua MODIS fire hotspots [Giglio *et al.*, 2003], consistent with the GFED approach.

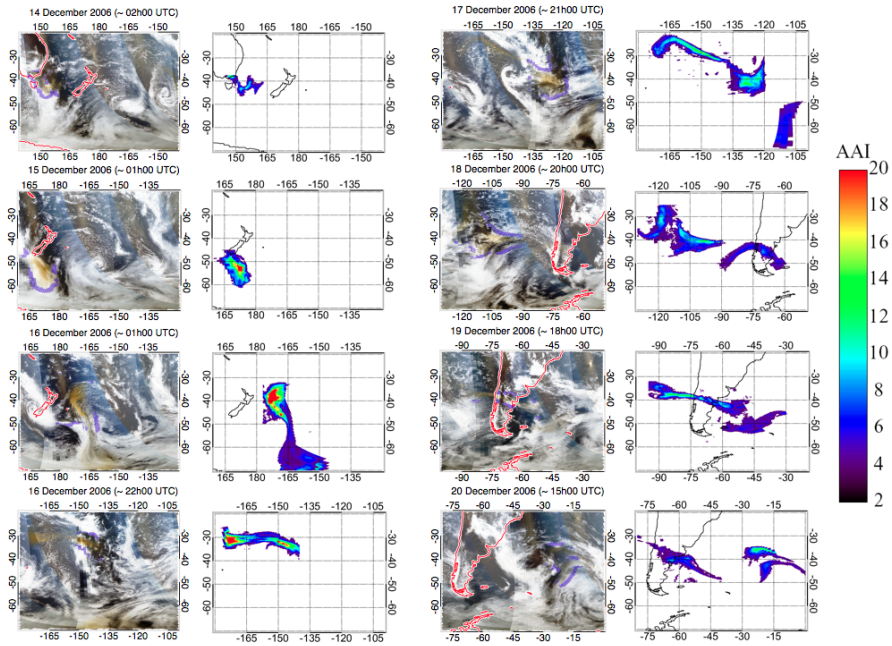


**Figure 5.1** Evolution of the biomass burning aerosol plume from 14 to 20 December 2006. The left panels represent false color image derived from OMI observations where the aerosol plume appears in brown. The right panels show the OMI-derived absorbing aerosol index (AAI) included in the OMI TOMS  $O_3$  product. The dark blue pixels in the false-color images show the locations of the viewing scenes used to calculate the altitude of the clouds adjacent to the plume shown in Figure 5.2.

### 5.3 Origin and Vertical Transport of the Australian Biomass Burning Event

Figure 5.1 presents OMI observations of the time evolution and transport of the Australian biomass burning event from 14 to 20 December 2006. The RGB and AAI images show that a large amount of absorbing aerosol was released into the atmosphere on 14 December 2006 from southeastern Australia, and that the resulting plume was subsequently transported over the Pacific Ocean. Figure 5.1 indicates that the aerosol plume travelled from Tasmania to Chile within a period of five days,

corresponding to an average (Eastward) plume velocity of more than 100 km/h. We will later show (Figure 5.9) that the frontal part of the plume completed its journey around the world and reached the point where it was emitted after 12 days.

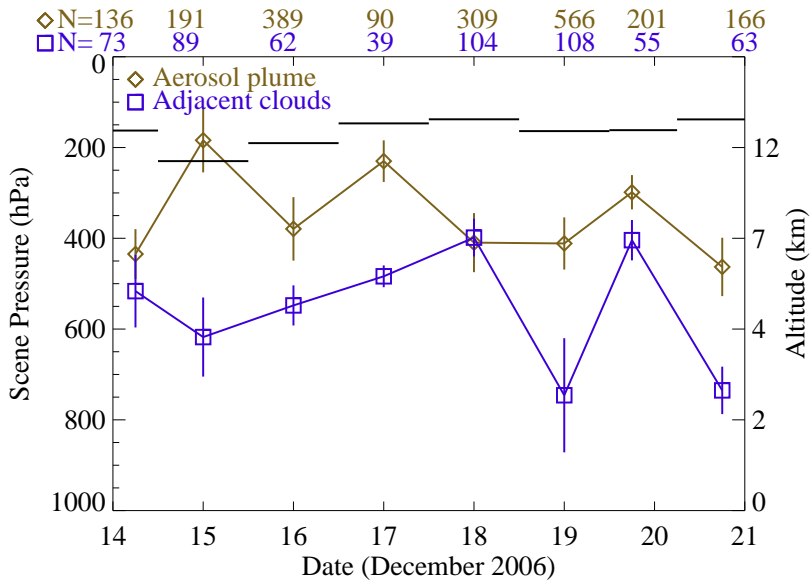


**Figure 5.2** Temporal evolution of ( $O_2-O_2$ ) effective scene pressure for clouds adjacent to the aerosol plume (blue squares), and the aerosol plume (brown diamonds) originating from Australian forest fires in December 2006, as observed by OMI. The error bars represent the standard deviation of the distribution; the number of pixels used for each datapoint are given in the upper x-axis. The right y-axis represents approximate altitudes for the pressures on the left y-axis. The pixels used for the adjacent cloud pressures are marked blue in Figure 5.1. The black line represents the ECMWF tropopause height (WMO 1985 criterion).

The RGB images in Figure 5.1 shows that the dark brown aerosol plume was often situated over white cloudy areas, and persisted for more than a week, suggesting that the aerosol plume resided in the dry air well above the clouds. This is considerably longer than the average lifetime of 3.8 days for aerosols in biomass burning outflow plumes as calculated by *Edwards et al.* [2006]. Because CALIPSO was switched off between 6 and 18 December 2006 due to space weather conditions, we use effective cloud/aerosol pressures from the OMI  $O_2-O_2$  algorithm [*Acarreta et al.*, 2004] to evaluate the vertical distribution of the aerosol plume.

Figure 5.2 shows that clouds adjacent to the plume (indicated by the dark blue pixels in the RGB images of Figure 5.1) on average reside between 800 and 400 hPa,

corresponding to altitudes of up to 6 km. These  $O_2-O_2$  cloud levels provide a lower limit for the height of the aerosol plume. Using the  $O_2-O_2$  pressures retrieved for the OMI pixels with enhanced AAI, we find significantly lower pressures (brown diamonds in Figure 5.2) than for the adjacent cloud scenes, which confirms that the absorbing aerosol plume is situated in the upper troposphere above the clouds. Figure 5.2 also shows the tropopause pressure from ECMWF meteorological fields, using the WMO 1985 definition of the tropopause (lowest level where the lapse rate is smaller than  $2^\circ\text{C}/\text{km}$ ). CALIOP measurements of the plume altitude, which will be discussed in the next section, suggest that the aerosol plume resided near the tropopause, and that part of the plume may have entered the lower stratosphere.

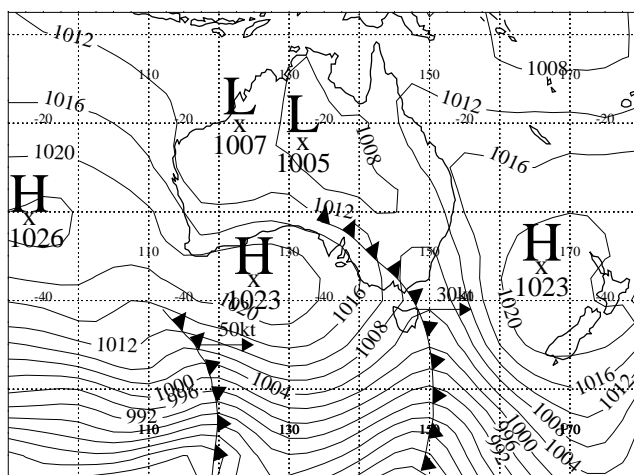


**Figure 5.3** Weather chart showing the mean sea level pressure (manual analysis) for the Australian region on 14 December 2006 at 0600 UTC. The cold front that caused the lofting of the smoke plume stretches over southeastern Australia. Image based on data from the Australian Government Bureau of Meteorology and on NCEP/NCARR reanalysis.

The OMI  $O_2-O_2$  pressure for the plume on 14 December indicates that the plume is at approximately 450 hPa right after the biomass burning event. This is most likely due to pyro-convection and rapid uplifting by a frontal system that reached southeastern Australia on 14 December. Until 13 December, the meteorological situation over southeastern Australia was dominated by a subtropical high. A normal situation for that time of year, which is characterized by intense drought and heat, creating favorable conditions for spawning forest fires. On 14 December,



a low pressure trough, associated with a depression at 60°S, 140°E, approached southeastern Australia from the west as shown in the weather chart of Figure 5.3. The approaching trough resulted in a strong pressure gradient between this low and the subtropical high situated between Australia and New Zealand. The location and timing of the rapid eastward transport and frontal uplifting of the aerosol pollution plume on 14 and 15 December corresponds well with this pressure gradient.

We see from Figure 5.2 that on 15-17 December, right after the biomass burning event on 14 December, the plume appears to be particularly high, with O<sub>2</sub>-O<sub>2</sub> pressures of approximately 300 hPa. At these altitudes, the aerosol plume is rapidly transported in easterly direction by the subtropical jet stream, in line with the observations shown in Figure 5.1. Between 18 and 23 December, the plume O<sub>2</sub>-O<sub>2</sub> pressures gradually decrease to values around 500 hPa. To investigate whether this apparent subsidence of the aerosol plume is real, we now compare the OMI O<sub>2</sub>-O<sub>2</sub> pressures to backscatter information from CALIOP.

#### 5.4 Evaluation of OMI O<sub>2</sub>-O<sub>2</sub> pressures for aerosol vertical distribution

##### 5.4.1 Comparison with CALIOP results

Figure 5.4 shows a comparison between the vertical distribution of the aerosol plume observed by CALIOP and by OMI for four cases on 19 and 21 December 2006. We selected OMI pixels with AAI>2 collocated with the CALIOP track. For all four cases, the altitude associated with the OMI O<sub>2</sub>-O<sub>2</sub> pressures is significantly lower than the vertical distribution of the plume observed by CALIOP. For OMI orbit 12923, shown in Figure 5.4(a), CALIOP observed the aerosol plume at approximately 10 km above a low-lying cloud layer at approximately 1 km altitude (illustrated by gray colors indicating high backscatter signals).

For this situation, OMI O<sub>2</sub>-O<sub>2</sub> pressures agree well with the altitude of the low-lying cloud layer (solid red line). For OMI orbit 12924, when the aerosol plume crossed South America, CALIOP indicates the aerosol plume at 12 km altitude above a 8 km high cloud layer (Figure 5.4(b)). Again, the OMI O<sub>2</sub>-O<sub>2</sub> pressures correspond with the CALIOP cloud levels, indicating that OMI O<sub>2</sub>-O<sub>2</sub> pressure retrievals are mainly sensitive to bright clouds in such situations, and not to aerosol plumes residing above. Figure 5.4(c) shows the comparison for a situation with a high aerosol plume (10-14 km) over high, intermittent clouds (OMI orbit 12925, western Atlantic). Here, O<sub>2</sub>-O<sub>2</sub> pressures indicate altitudes as high as 8 km, notably between 33°S and 36°S, a region where CALIOP did not observe clouds. This finding suggests that the OMI O<sub>2</sub>-O<sub>2</sub> retrieval is sensitive enough to detect the presence of a high aerosol plume over cloud-free scenes, but also that the O<sub>2</sub>-O<sub>2</sub> pressures are an overestimate of the actual aerosol plume pressure. This is confirmed by Figure 5.4(d) showing the comparison for orbit 12953, observed on 21 December 2006 over South

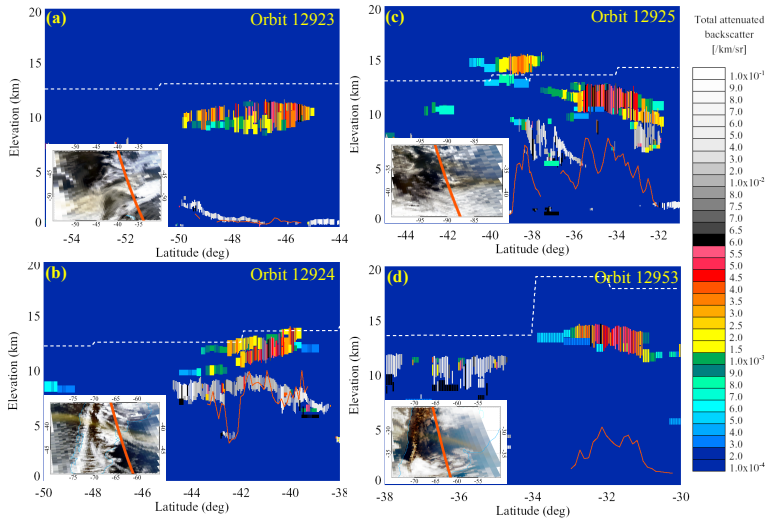


**Figure 5.4** CALIOP observation of the aerosol plume on 19 and 21 December 2006. The color coding represents the total attenuated backscatter ( $1/\text{km}/\text{sr}$ ) from the CALIOP aerosol and cloud layer product. The OMI  $O_2-O_2$  derived plume height is co-plotted in red. The insets show the OMI RGB image of the plume together with the CALIOP footprint in orange. The dashed white line represents the ECMWF tropopause level. Panel (a) shows OMI orbit 12923 (southern Atlantic, 19 December), (b) OMI orbit 12924 (South America, 19 December), (c) OMI orbit 12925 (southern Atlantic, 19 December), and panel (d) OMI orbit 12953 (South America, 21 December).

America. On this clear-sky day, CALIOP measured the plume between 12 and 14 km, but the OMI  $O_2-O_2$  pressures correspond to altitudes up to 5 km.

Figures 5.4(c-d) suggest that the discrepancies between CALIOP and OMI plume heights over cloud-free scenes decrease with increasing backscattered signal from the plume. This is most evident in orbit 12925 where OMI observes highest altitudes for backscatter values up to  $0.006 \text{ km}^{-1}\text{sr}^{-1}$ . We evaluate the sensitivity of OMI  $O_2-O_2$  pressures of the aerosol plume to the density of the aerosol plume in Figure 5.5. Figure 5.5 indicates that the OMI  $O_2-O_2$  pressures of aerosol plumes generally decrease with increasing AAI (and that the agreement with CALIOP altitudes improves), i.e., that high aerosol plumes are best obtained from OMI scenes with high AAI. For such situations there is a smaller contribution from scattering from the atmosphere below the plume than for situations with low AAI, resulting in less  $O_2-O_2$  absorption.

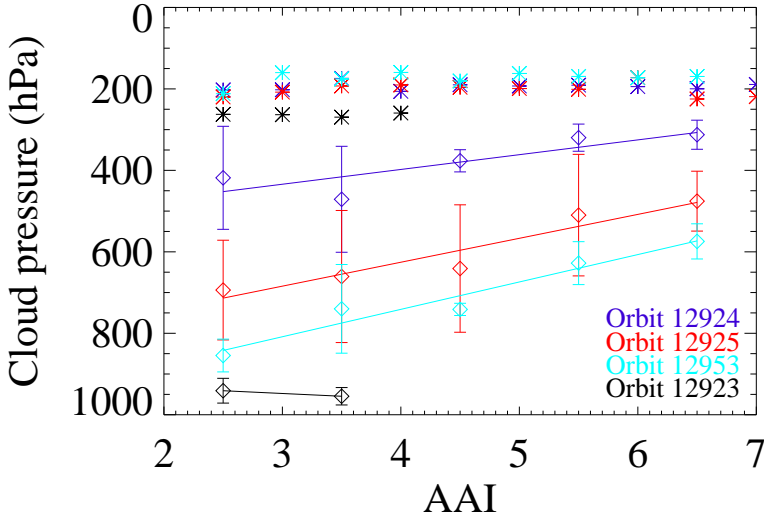


**Figure 5.5** OMI  $O_2-O_2$  cloud pressure versus AAI for pixels of the smoke plume collocated with the CALIOP footprint. The solid lines represent a linear fit to the OMI data points (diamonds). The asterisks represent the CALIOP altitude for collocated pixels. In case of orbit 12923 (black) a low lying cloud layer yields high cloud pressures. For orbits 12924 (blue) and 12925 (red) a high lying cloud layer resides below the aerosol plume. Orbit 12953 (cyan) represents a truly cloud-free scene (see Figure 5.4).

#### 5.4.2 Radiative transfer results

To further investigate the low bias in OMI aerosol altitude retrievals relative to CALIOP, we conducted radiative transfer simulations with the atmospheric situation (cloud and plume height) observed by CALIOP as input, and top-of-atmosphere UV-Vis reflectance spectra as output. We subsequently applied the OMI  $O_2-O_2$  and AAI retrieval algorithms to the simulated spectra. The simulations were done with the DAK radiative transfer model that includes all relevant physical processes including Rayleigh and multiple scattering, trace gas absorption, scattering by aerosol or cloud particles, and polarization. Aerosols were characterized by their single scattering albedos (0.79-0.94, consistent with values observed for biomass burning plumes [Dubovik *et al.*, 2002, Mitchell *et al.*, 2006, Qin and Mitchell, 2009] and aerosol optical thicknesses. Further details about the radiative transfer simulations are listed in Table 5.1. We found that our simulations result in AAI values that agree well with the actually observed AAI values, supporting the assumptions on aerosol characteristics in our simulations. Figure 5.6 shows the aerosol height input to DAK, and the subsequently retrieved aerosol height from the  $O_2-O_2$  algorithm.

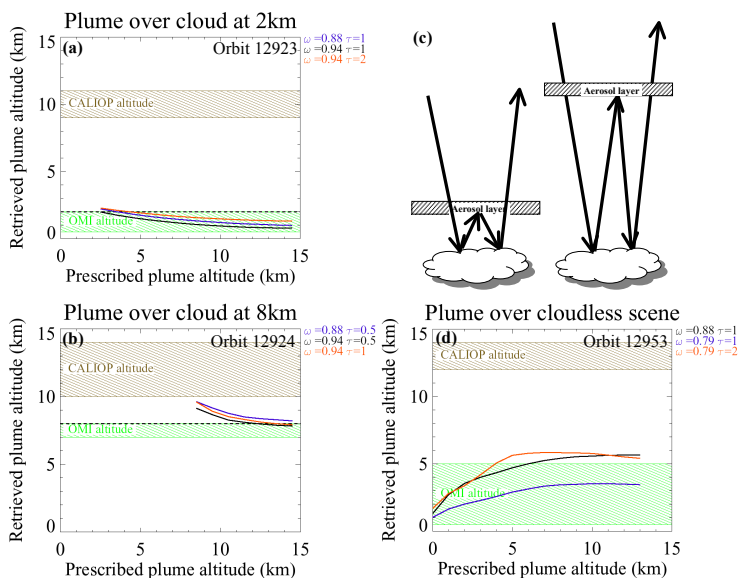


**Figure 5.6** Retrieved (simulated) OMI  $O_2-O_2$  plume altitudes as a function of prescribed plume altitude for various cloud-aerosol plume scenarios. The bands indicate the plume altitude observed by OMI (green) and CALIOP (brown). In panel (a) the cloud is situated at 2 km and the prescribed plume altitude varies between 3 and 14 km. The dashed black line represents the altitude of the cloud in the radiative transfer calculation. The solid lines represent the resulting plume altitude from the RTM simulations. The single scattering albedo ( $\omega$ ) of the aerosols and the optical thickness ( $\tau$ ) of the plume are given in the legend of each plot. In panel (b) the cloud is situated at 8 km and the prescribed plume altitude was varied between 9 and 14 km. In panel (d) the prescribed plume altitude was varied between 0 and 14 km over a cloudless scene. Panel (c) shows a schematic drawing of the photonpath lengthening caused by an aerosol layer lying closely above a cloud (left drawing) or high above a cloud (right drawing).

Simulations of orbits 12923 (Figure 5.6(a)) and 12924 (Figure 5.6(b)) confirm that the  $O_2-O_2$  algorithm is sensitive to the altitude of the cloud rather than the altitude of the aerosol plume in situations of an optically thin aerosol plume above a lower-lying cloud deck. In Figure 5.6(d), a simulation of orbit 12953, we see that the  $O_2-O_2$  algorithm does detect the lofted plume, but underestimates its altitude; for a 13-15 km aerosol plume (as observed by CALIOP), OMI retrieves a plume at 3-6 km, consistent with the observations shown in Figure 5.4(d). We also performed a simulation of an optically thick ( $\tau > 3$ ) aerosol plume over a cloud deck, similar to the

situation observed for OMI orbit 12856 on 15 December, in absence of CALIOP data. In this case the O<sub>2</sub>-O<sub>2</sub> algorithm retrieved the altitude of the aerosol plume with a scene pressure of approximately 200 hPa, comparable to the OMI O<sub>2</sub>-O<sub>2</sub> pressure observed on 15 December (Figure 5.2). Figure 5.6(a) and (b) show that when using the O<sub>2</sub>-O<sub>2</sub> algorithm for determining aerosol plume height, the altitude of the cloud rather than the altitude of the aerosol plume is retrieved. This is attributed to the fact that the brighter cloud outshines the plume. Figure 5.5 suggests that when the plume is dense enough, the cloud no longer outshines the plume, and information on the altitude of the plume is retrieved.

**Table 5.1** *Input parameters used in the radiative transfer calculations of Figure 5.6. The cloud optical thickness  $\tau=40$  was chosen to be consistent with the cloud model (Lambertian reflector, with albedo 0.8) used in the O<sub>2</sub>-O<sub>2</sub> algorithm.*

Aerosol Model	Scattering Type	$\tau$	Altitude (km)	g	Size Parameters		Refractive Index		SSA
					$r_{\text{eff}}$ ( $\mu\text{m}$ )	$v_{\text{eff}}$	Re(m)	Im(m)	
Cloud	Henyey-Greenstein <sup>a</sup>	40	1-10	0.85	–	–	–	–	1.0
BBA*	Log normal Mie <sup>b</sup>	0.5–4	cloudtop – 15	–	0.08 <sup>c</sup>	1.45 <sup>c</sup>	1.55 <sup>c</sup>	0	1.0
BBA	Log normal Mie	0.5–4	cloudtop – 15	–	0.08	1.45	1.55	–0.005	0.97
BBA	Log normal Mie	0.5–4	cloudtop – 15	–	0.08	1.45	1.55	–0.01	0.94
BBA	Log normal Mie	0.5–4	cloudtop – 15	–	0.08	1.45	1.55	–0.02	0.88
BBA	Log normal Mie	0.5–4	cloudtop – 15	–	0.08	1.45	1.55	–0.04	0.79
		Spectral Properties			Trace Gas Columns (molecules/cm <sup>2</sup> )				
Surface Albedo	Atmosphere Type	Range	Resolution	O <sub>3</sub>		NO <sub>2</sub>			
0.05	Mid-lat summer <sup>d</sup>	460–490 nm	0.2 nm	9.0 · 10 <sup>18</sup>		5.9 · 10 <sup>15</sup>			

<sup>a</sup>See *Henyey and Greenstein* [1941]

<sup>b</sup>See *de Rooij and van der Stap* [1987]

<sup>c</sup>Values for biomass burning aerosol were taken from *de Graaf et al.* [2005]

<sup>d</sup>See *Anderson et al.* [1986]

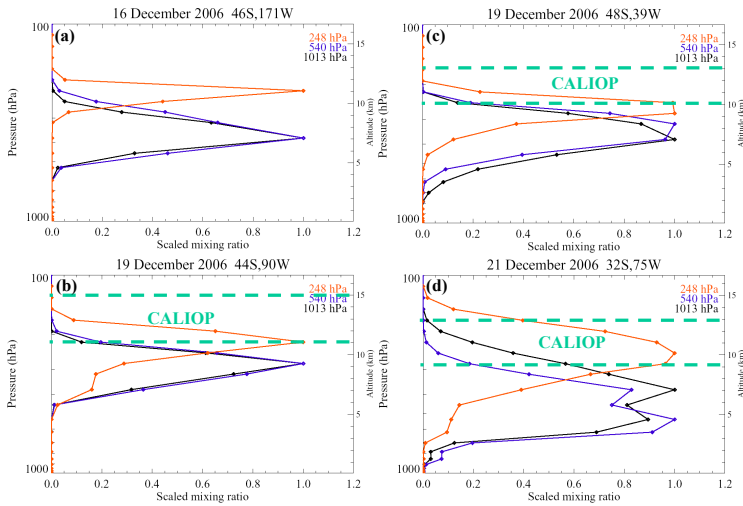
\*BBA = Biomass Burning Aerosol

Figure 5.6(a) and (b) also show that for the plume above a cloud layer, increasing the plume height decreases the retrieved plume altitude. This apparently contradictory finding can be explained by lengthening of the light path by reflections between the cloud top and the aerosol plume. A longer light path will increase the observed O<sub>2</sub>-O<sub>2</sub> column which in turn will result in a decrease of the retrieved altitude, as sketched in Figure 5.6(c).

We conclude that for determining the altitude of the aerosol plume an active sounding instrument like CALIOP gives the best results. In absence of CALIOP data, OMI O<sub>2</sub>-O<sub>2</sub> pressures of adjacent clouds provide constraints on the lower limit of the plume's altitude. Direct application of the O<sub>2</sub>-O<sub>2</sub> algorithm to the aerosol plume gives under specific conditions some indication for the plume altitude, but this depends on the atmospheric conditions, especially the optical thickness of the plume. In general, the O<sub>2</sub>-O<sub>2</sub> pressure of the aerosol plume is most indicative for situations with high AAI ( $\gtrsim 5$ ) and no clouds. The radiative transfer simulations show that the O<sub>2</sub>-O<sub>2</sub> algorithm always underestimates the altitude of the plume. The

## 5.5 Injection Height and Long-Range Transport of the Australian Biomass Burning Event

$O_2-O_2$  algorithm in its current form was designed and optimized for cloud retrieval, as illustrated by the employed scattering model (a Lambertian reflector with albedo 0.8). We hypothesize that by the use of a scattering model which is adjusted to the scattering and absorption properties (optical thickness, single scattering albedo) of a smoke aerosol layer of sufficiently high optical thickness, will produce better  $O_2-O_2$  retrievals of the pressure of smoke aerosol plumes.



**Figure 5.7** Mixing ratio profiles of a passive tracer emitted in TM4 on 14 December 2006. Different injection heights result in different profiles (colors). The profiles have been scaled to unity peak intensity. Each panel shows the profiles for a specific day and location; see Figure 5.9 for the 2-D shape of the tracer field on these dates. In panels (b)-(d) the plume altitude observed by CALIOP is indicated in green.

## 5.5 Injection Height and Long-Range Transport of the Australian Biomass Burning Event

According to the GFED-2 record [van der Werf *et al.*, 2006], resampled to a daily time step using fire counts from four daily overpasses of the MODIS sensors on board the Terra and Aqua satellites ([Giglio *et al.*, 2003]), wildfires blazed on 14 December 2006 between 30-40°S, and 140-154°E. To evaluate the injection height and subsequent transport of the biomass burning plume, we released a passive,

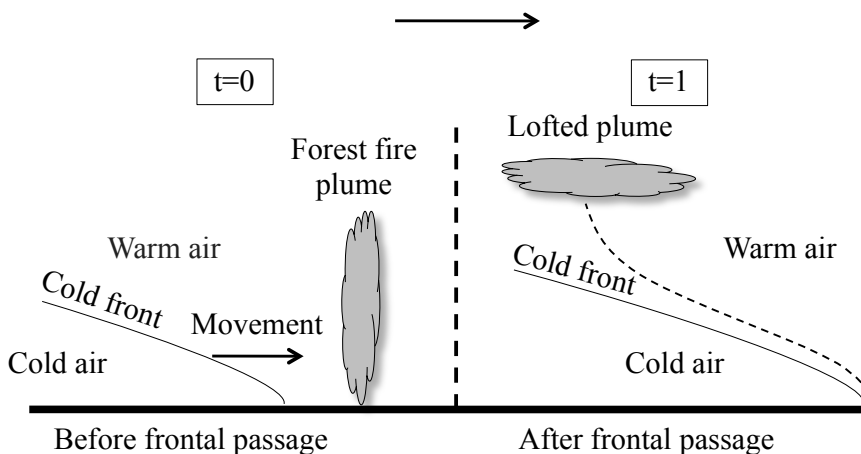


**Figure 5.8** Schematic drawing illustrating the lofting of the biomass burning plume by a passing cold front. The heat of the fire provides the plume with additional buoyancy, allowing it to rise above the top of the cold front.

but water soluble, tracer in TM4 on this date in the grid cells with fires between 30-40°S, and 140-154°E. We conducted simulations with tracer emissions at the surface level (1013 hPa), and at 540 hPa. Figure 5.7 shows that emissions at the surface and at 540 hPa, lead to remarkably similar tracer vertical distributions, with highest tracer concentrations between 300 and 400 hPa. Figure 5.7(b) and 5.7(d) clearly show that after 5-7 days the simulated tracer plumes are too low by 2-3 km relative to CALIOP observations. These results suggest that TM4 has some skill in simulating the lofting of the plume by the cold front, but also that the model fails to push the plume towards altitudes where it is picked up by the jet stream and where it has actually been observed. A schematic picture of the pyro-convective lofting mechanism is sketched in Figure 5.8. This deficiency of the model is likely a result of TM4 not accounting for the enhanced buoyancy of the plume provided by the heat of the extensive fires. To circumvent this shortcoming, and to mimic the effects of pyro-convection, we conducted a simulation where we released the tracer at 248 hPa. Figure 5.7 shows that injection at 248 hPa results in tracer plumes that are higher by 2-5 km, and closer to the observed CALIOP plume altitudes.

That injection at 248 hPa closely approximates the true emission height is confirmed by Figure 5.9 that compares the evolution of the passive tracer with the OMI AAI observations. The tracer fields represent simulated vertical tracer columns between 540 and 130 hPa (5-15 km), sampled at 13h30, close to the OMI overpass time.

A primitive kernel, accounting for the increasing AAI-sensitivity with height

[de Graaf *et al.*, 2005], has been applied to the simulated fields for consistency. We see a good correspondence between the simulated tracer columns and the observed AAI fields between 14 and 19 December. The elongated structure simulated over the southern Pacific on 16 December (Figure 5.9 (c)) coincides with the observed split-up in the AAI field.

The locations of the AAI plumes are captured very well on 18 and 19 December although the modeled feature west of South America has dispersed more and is spatially more extended than the AAI plume marked  $N_1$ . On 20 and 21 December the remaining AAI plumes are all captured by the model, especially the narrow band-like structure over South America on 21 December is reproduced well. We also see that the modeled tracer features appear more extended than the AAI plumes, and that tracer features persist over the east Pacific Ocean which are not seen in the AAI observations, such as the feature marked  $N_2$  on 21 December. However, the AAI observations coincide remarkably well with the maximum values of the tracer simulations for 18-21 December. For 22 and 23 December the discrepancy between model and observations appears larger, but the scattered remains of the AAI plume still coincide with the front moving part of the modeled tracer. On 25 December, when the aerosol plume completes its circumterrestrial tour, AAI and the simulations do not correspond anymore.

In the modeling experiment we tested various injection heights where we focused on the agreement between AAI observations and model for the passage of the plume over South America between 18 and 21 December. The tests showed that for injection heights below 455 hPa the AAI plume marked  $N_1$  on 19 December was not reproduced by the model. For injection heights above 455 hPa this feature was reproduced, with little influence of the injection height. The agreement between model and AAI for the plume bridging South America on 21 December also varies slightly with injection height. The choice for injection at 248 hPa resulted in the best agreement between model simulations and OMI AAI and CALIOP observations on 19 and 21 December. Furthermore, simulations with lower injection heights exhibited discrepancies with the observations that immediately showed up in the first days after their release: a considerable amount of tracer remained in the region between Australia and New Zealand whereas the higher injection heights did not exhibit this stagnant behavior.

Figure 5.9 shows that TM4 reproduces the dilution of the plume similar to the OMI AAI observations, although the observed plume appears to shrink and thin more rapidly than the model tracer. This can be due to too strong diffusivity in the model or due to scavenging processes acting on the plume that are not accounted for by the model. Most likely, it is related to the thinning of the plume which causes the AAI to drop below the detection limit. This would explain why we see chunks of plume in the AAI whereas the model simulates a continuous band of enhanced concentrations. The role of scavenging processes in the model is demonstrated by Figure 5.10 which compares the model results for the water soluble, depositable tracer to a completely inert tracer. The tracer densities for the inert tracer are consistently higher than for



the water soluble tracer, which shows that by incorporating wet deposition the TM4 model is capable of simulating not only the transport of the aerosols in the plume but also their ultimate fate: removal by scavenging.

Extreme lofting by pyro-convection, although rare, is important because of the rapid pathway it offers for biomass combustion products to reach the high troposphere or lower stratosphere [Fromm *et al.*, 2005]. The meteorological conditions of a pyro-convection case described by Fromm *et al.* [2005] that enabled injection of biomass burning aerosol into the lower stratosphere via pyro-cumulonimbus clouds are very similar to what we find here. In both cases a passing cold front transported unstable air to a previously anti-cyclonal situation, which, in combination with the intense heat from the fires caused rapid lofting to high altitudes. Unlike Fromm's study, the aerosols from the December 2006 Australian forest fires did not reach the lower stratosphere but settled near the tropopause. It has been observed before that smoke emissions from large fires in Australia's temperate forests reached high altitudes. Mitchell *et al.* [2006] reported a plume altitude of 14 km following the January 2003 Canberra firestorm. Fromm *et al.* [2006] discussed the abnormally violent pyro-cumulonimbus triggered by this event that injected smoke from these fires into the stratosphere. Apparently in some cases the meteorological conditions that foster ferocious forest fires, strong winds after a prolonged drought, also stipulate the occurrence of pyro-convection (unstable air, frontal passage).

Currently, the TM4 model does not incorporate pyro-convection. Forest fire emissions are released at surface level and convection and advection of the released tracers are governed by meteorology alone, ignoring the buoyancy from the sensible heat of the fire. As pointed out by Hyer *et al.* [2007], most CTMs do not treat lofting of fire plumes properly and the common workaround in transport studies of forest fire events is to impose an injection height for the emission, as we did in this study. Leung *et al.* [2007] reported reasonable agreement between model results and measurements for monthly variations in CO concentrations when emitting half of the CO from fires in the free troposphere. Studies of various fire events have shown that the injection height of emission plumes varies considerably among the fires. The lofting of fire emissions depends on the energy of the fire and the local meteorological conditions [Hyer *et al.*, 2007]. Therefore it is not sufficient to have CTMs release the emissions of forest fires at pre-defined, fixed, injection heights. Especially when dealing with exceptional fire events as in this study, a parameterization of the lofting of the plume is needed. To implement this in TM4 we suggest an approach similar to Freitas *et al.* [2006, 2007], who embedded a sub-grid plume model in a 3-D CTM and obtained good results for CO distributions in regions close to the source. The plume model needs the buoyancy flux [Freitas *et al.*, 2007], which requires an additional database of vegetation type to estimate the heat flux and information on the fire size to calculate the buoyancy flux. Preliminary tests with a 1-D plume-rise model, adapted from Freitas *et al.* [2007], and currently in development to be implemented in GEOS-Chem [Bey *et al.*, 2001], suggest that aerosols emitted from large fires on

14 December reached the upper troposphere ( $\approx 380$  hPa), in agreement with the OMI  $O_2-O_2$  pressure of the aerosol plume retrieved on 14 December as shown in Figure 5.2. Although this is somewhat lower than the injection height used in the TM4 simulations, it demonstrates the importance of pyro-convection for the December 2006 Australian forest fires. The fact that there is a difference between the injection height in TM4 (248 hPa) and the injection height suggested by the plume rise model may indicate that, apart from pyro-convection, another process contributed to the lofting. Absorbing aerosols situated above bright clouds are known to be subject to considerable heating (up to  $80 \text{ W/m}^2$ ; *Stammes et al.* [2009]), which may have led to so-called sunlight-induced upward forcing.

## 5.6 Conclusions and Outlook

We studied an exceptional case of aerosol transport originating from intense forest fires in southeastern Australia on 14 December 2006. On this date, a dense plume was injected into the jet stream by pyro-convection into a highly unstable atmosphere with a passing cold front. Daily observations of OMI Absorbing Aerosol Index reveal that the plume was transported eastward across the Pacific in 5 days, and circumnavigated the globe in 12 days.

In absence of CALIOP data, we explored OMI  $O_2-O_2$  pressures to obtain information on the altitude of the aerosol plume.  $O_2-O_2$  pressures retrieved from OMI pixels with high aerosol loading were consistently lower than  $O_2-O_2$  pressures for cloudy scenes adjacent to the plume, showing that the plume resided well above the clouds. OMI  $O_2-O_2$  pressures indicate that the plume resided close to the tropopause in the first 3 days after emission. Data from the CALIOP spaceborne lidar (available from 19 December 2006 onwards) show that the plume was still situated in the upper troposphere 5-7 days after emission. Detailed radiative transfer calculations suggest that the current OMI  $O_2-O_2$  retrievals contain useful information on the altitude of the aerosol plume under specific conditions (high AAI, no clouds below). Detecting the altitude of aerosols from space with passive remote sensing could be improved by including a scattering model that incorporates the optical properties of aerosol layers rather than those of clouds.

Simulations with emission of a passive, soluble tracer in the TM4 chemistry transport model show that an injection height of 248 hPa ( $\approx 10$  km) gives the best agreement with 2-D OMI AAI observations and with the vertical distribution of the plume observed by CALIOP. Injection at the surface and at 540 hPa ( $\approx 5$  km) yields similar tracer vertical distributions that are too low relative to the vertical distribution observed by CALIOP. The similarity of the surface and 540 hPa injections shows that the lofting of the plume by the cold front is properly simulated by TM4. The reason behind the fact that the plumes are too low relative to CALIOP is because

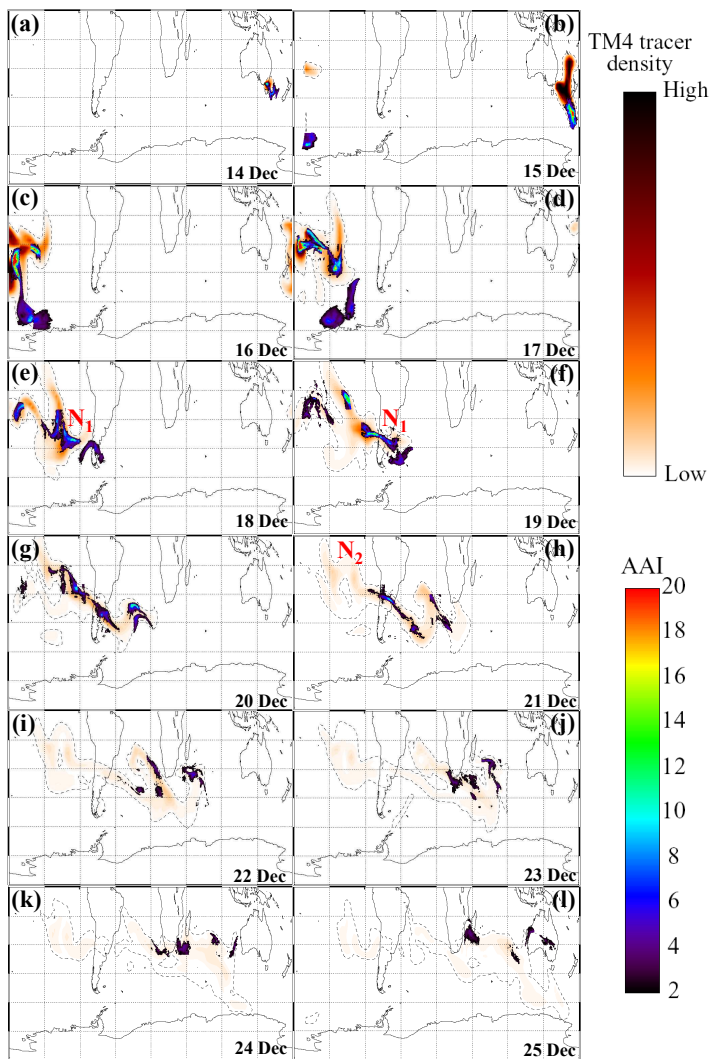


**Figure 5.9** Time series of TM4 simulation of a water soluble passive tracer released on 14 December at 248 hPa. Panels show the integrated tracer column density between 540 and 130 hPa at 24 hour intervals. The dashed contour represents the 1% level. Simultaneous OMI AAI observations with AAI > 2 are co-plotted with the colorscale indicating the AAI value between 2 and 20.

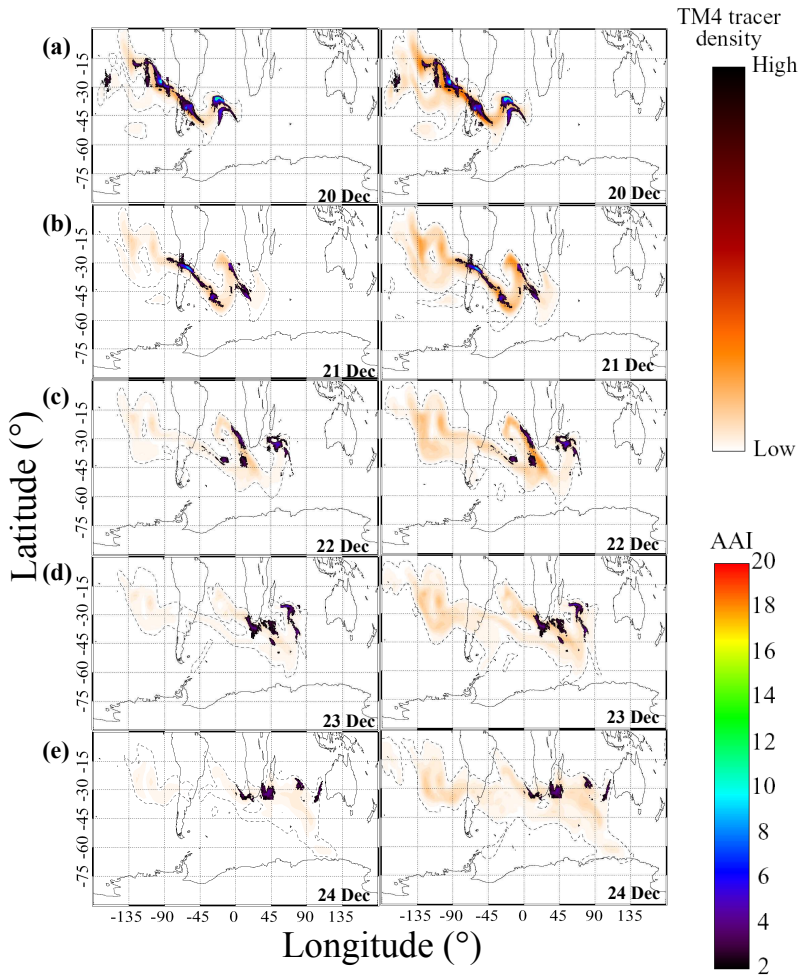


**Figure 5.10** Same as Figure 5.9, but only for 20-24 December. The plots in the left column show the TM4 results for a water soluble tracer subject to deposition, whereas the plots in the right column show the TM4 results for an inert passive tracer.

TM4, like most CTMs, ignores the additional buoyancy resulting from the heat of the fire.

TM4 simulations with a soluble and depositable tracer better reproduce the observed (OMI AAI) dilution of the aerosol plume than simulations with an inert tracer. This suggests that TM4 is successful in describing removal by scavenging of the aerosols.

Our study illustrates that neglecting plume rise due to pyro-convection can be a source of considerable model error. To better understand the effects of biomass burning on the global atmospheric composition, emissions from fires should be released at the appropriate heights. One promising approach [Freitas *et al.*, 2007] is to incorporate injection heights computed with a 1-D cloud model that takes into account the convective energy of the fire in the context of environmental meteorological conditions.

### *Acknowledgments*

OMI is a contribution of the Netherlands Agency for Aerospace Programs (NIVR) in collaboration with the Finnish Meteorological Institute (FMI) to NASA's EOS-Aura satellite. We acknowledge P.K. Bhartia for the use of OMI AAI data included in the OMI TOMS O<sub>3</sub> product. The OMTO3 product is available at <http://daac.gsfc.nasa.gov/Aura/OMI/>. The CALIPSO/CALIOP data used in this study are available at [http://eosweb.larc.nasa.gov/PRODOCS/calipso/table\\_calipso.html](http://eosweb.larc.nasa.gov/PRODOCS/calipso/table_calipso.html). We thank Maarten Krol for stimulating discussions about the modeling of pyro-convection. Mark Kroon incited us to study the December 2006 Australian forest fires and, together with Pieternel Levelt, provided useful comments to this manuscript.

## Summary and outlook

### 6.1 Overview

In this thesis I have covered several aspects of the chain of OMI data processing, starting with uncalibrated instrument data (level 0 –L0–) and ending with an assimilated climatology of stratospheric NO<sub>2</sub> (L4). My work involved instrument calibration, contributing to a consistent DOMINO tropospheric NO<sub>2</sub> data set, validation, and interpretation of OMI measurements in terms of transport and chemistry. In the introduction of this thesis the following four questions were formulated:

1. How to determine the spectral slitfunction of OMI?
2. How to set up, maintain and validate a near real time and offline retrieval of tropospheric NO<sub>2</sub> from OMI?
3. What is the quality of stratospheric NO<sub>2</sub> retrievals from OMI and what can we learn about the photochemical behavior and trends of stratospheric NO<sub>2</sub>?
4. How to use satellite data to monitor and characterize transport phenomena in the atmosphere?

The first question was addressed by using a novel method based on an echelle grating. The spectral slitfunction for each wavelength and viewing angle was sampled by one of approximately 50 diffraction orders that scanned the OMI spectral range with wavelength increments 10 times smaller than the spectral resolution of OMI. The slitfunction parameters that were determined this way are used in the retrieval of NO<sub>2</sub> and of several other OMI products.

The second question resulted in the set up of the operational DOMINO system to retrieve tropospheric and stratospheric NO<sub>2</sub> columns from OMI measurements. The DOMINO system provides a near real time (NRT) data stream that is available within 3-4 hours after measurement and a consistent set of offline processed

and reprocessed data (collection 3, data version 1.0.2) for the entire OMI mission (October 2004 – present). DOMINO data are widely used by the scientific and air quality community, and have resulted in various publications. Conclusions and recommendations formulated in validation studies contribute to further improving the DOMINO product to the benefit of the users.

The answer to the third question is split in three parts. First, an analysis of the performance of the assimilation showed that the assimilation scheme is insensitive to tropospheric contributions, and results in a forecast model state that is generally within  $0.15 \times 10^{15}$  molecules/cm<sup>2</sup> of the analysis over remote areas where stratospheric NO<sub>2</sub> dominates the total column. The second step was the validation, showing that stratospheric NO<sub>2</sub> from DOMINO and from the OMI Standard Product agree within  $0.3 \times 10^{15}$  molecules/cm<sup>2</sup> (13%) with ground-based observations from the NDACC/SAOZ network. However, DOMINO performs superior to the Standard Product by capturing the dynamic variability of NO<sub>2</sub> in the stratosphere, as was shown by DOMINO observations of the daytime increase of stratospheric NO<sub>2</sub> and the day-to-day variations in the NO<sub>2</sub> field associated with the collapse of the Arctic Polar vortex. The third step was the analysis of the 5 year data record of OMI observations of stratospheric NO<sub>2</sub>, showing a profound interhemispheric asymmetry in the QBO signal over the tropics. There is good agreement between the Lauder data record and collocated DOMINO stratospheric NO<sub>2</sub> observations, that both show a small increase of approximately +0.5% per decade for the timespan of the OMI mission (2004-2010).

In response to the fourth question, I investigated the rapid around the world transport of an aerosol plume emitted on 14 December 2006 by intense forest fires in southeastern Australia. OMI Absorbing Aerosol Index observations show that the plume crossed the Pacific in 5 days and circumnavigated the globe in 12 days. This transport event was initiated by pyro-convective lofting of the plume into the tropopause region, triggered by the combination of a passing cold front and the latent heat of the fires. The OMI O<sub>2</sub>-O<sub>2</sub> algorithm is sensitive to the height of the aerosol plume, but it underestimates the plume's altitude obtained from coincident CALIOP observations. Results from radiative transfer simulations help to explain the underestimation of the plume's altitude by showing that photons that are scattered from lower-lying clouds outshine the diluted plume. Nevertheless, for high AAI and cloud-free scenes, the O<sub>2</sub>-O<sub>2</sub> retrievals contain useful information on the altitude of the aerosol plume. TM4 simulations agree best with the observed transport of the aerosol plume when a passive tracer is released at 248 hPa ( $\approx 10$  km). Simulations with lower injection heights underestimate the CALIOP observations because TM4 does not simulate pyro-convection. TM4 simulations with a soluble and depositable tracer better reproduce the dilution of the aerosol plume that is observed in the OMI-AAI than simulations with an inert tracer.

---

## 6.2 Outlook

Based on the work described in this thesis several issues for further research can be identified.

- Accurate estimations of the height of aerosols is of great importance. The OMI O<sub>2</sub>-O<sub>2</sub> cloud retrieval algorithm can provide information on the vertical distribution of aerosols, but underestimates their altitude, partly because the employed scattering model is optimized for the retrieval of clouds. Detection of the altitude of aerosols by the O<sub>2</sub>-O<sub>2</sub> algorithm could be improved by using a scattering model that incorporates the optical properties of aerosol layers. Because of the relatively small optical depth of typical aerosol layers, the concept of a Lambertian reflector should be replaced by an semi-opaque layer that allows photons to pass through it.
- Pyro-convection significantly enhances the impact of forest fires by increasing the lifetime and the range over which the emissions are transported. Most global CTMs do not include pyro-convection, which leads to inaccuracies in model simulations of emissions from (intense) forest fires and biomass burning events. Pyro-convective lofting can be simulated by embedding a sub-grid plume rise model that takes into account the meteorological conditions at the fire location and the fire's latent heat to simulate the vertical transport of the plume. Embedding a 1-D plume rise model into a regional model has shown promising results for simulations of the transport of CO emitted by forest fires in the Amazon basin [Freitas *et al.*, 2007].
- The current 5+ year OMI data record is too short to reliably distinguish long term trends in stratospheric NO<sub>2</sub> from phenomena with multi-annual periodicity, like the QBO. Extending the OMI data record with measurements from GOME (1995-2003) and SCIAMACHY (2002-present) yields a data set that spans more than 15 years of global observations of NO<sub>2</sub> in the stratosphere. This data series can then be used to determine the latitudinal dependence of the trend in stratospheric NO<sub>2</sub>, as well as to determine the influence of phenomena such as the QBO, Solar Index and ENSO on the latitudinal distribution of stratospheric NO<sub>2</sub>. Comparing the satellite-observed climatology of stratospheric NO<sub>2</sub> to simulations with a coupled chemistry-climate model of the stratosphere will improve understanding of the processes that drive the variations in the global stratospheric NO<sub>2</sub> field.





## Bibliography

- Acarreta, J. R., J. F. de Haan, and P. Stammes, Cloud pressure retrieval using the O<sub>2</sub>-O<sub>2</sub> absorption band at 477 nm, *J. Geophys. Res.*, **109**, D05204, doi:10.1029/2003JD003915, 2004.
- Ahn, C., O. Torres, and P. K. Bhartia, Comparison of Ozone Monitoring Instrument UV Aerosol Products with Aqua/Moderate Resolution Imaging Spectroradiometer and Multiangle Imaging Spectroradiometer observations in 2006, *J. Geophys. Res.*, **113**, D16S27, doi:10.1029/2007JD008832, 2008.
- Anderson, G. P., S. A. Clough, F. X. Kneizys, J. H. Chetwynd, and E. P. Shettle, AFGL Atmospheric Constituents Profiles, Technical Report AFGL-TR-86-0110, Air Force Geophysics Laboratory, Hanscom AFB (MA), 1986.
- Beirle, S., S. Köhl, J. Pukite, and T. Wagner, Retrieval of tropospheric column densities of NO<sub>2</sub> from combined SCIAMACHY nadir/limb measurements, *Atmos. Meas. Tech.*, **3**, 283–299, doi:10.5194/amt-3-283-2010, 2010.
- Bey, I., *et al.*, Global modeling of tropospheric chemistry with assimilated meteorology: Model description and evaluation, *J. Geophys. Res.*, **106**, 23,073–23,095, doi:10.1029/2001JD000807, 2001.
- Bhartia, P. K. and C. W. Wellemeyer, *OMI Algorithm Theoretical Basis Document*, volume 2, chapter TOMS-V8 Total O<sub>3</sub> Algorithm, pp. 15–32 (NASA, Greenbelt, MD, 2002).
- Boersma, F., E. Bucsela, E. Brinksma, and J. F. Gleason, *OMI Algorithm Theoretical Basis Document*, volume 4, chapter NO<sub>2</sub>, pp. 13–28 (NASA, Greenbelt, MD, 2002).
- Boersma, K. F., H. J. Eskes, and E. J. Brinksma, Error analysis for tropospheric NO<sub>2</sub> retrieval from space, *J. Geophys. Res.*, **109**, D04311, doi:10.1029/2003JD003962, 2004.
- Boersma, K. F., *et al.*, Near-real time retrieval of tropospheric NO<sub>2</sub> from OMI, *Atmos. Chem. Phys.*, **7**, 2103–2118, doi:10.5194/acp-7-2103-2007, 2007.
- Boersma, K. F., *et al.*, Intercomparison of SCIAMACHY and OMI tropospheric NO<sub>2</sub> columns: Observing the diurnal evolution of chemistry and emissions from space, *J. Geophys. Res.*, **113**, D16S26, doi:10.1029/2007JD008816, 2008.
- Boersma, K. F., *et al.*, Validation of urban NO<sub>2</sub> concentrations and their diurnal and seasonal variations observed from space (SCIAMACHY and OMI sensors) using in situ measurements in Israeli cities, *Atmos. Chem. Phys.*, **9**, 3867–3879,

- doi:10.5194/acp-9-3867-2009, 2009.
- Bovensmann, H., *et al.*, SCIAMACHY: Mission Objectives and Measurement Modes, *J. Atmos. Sci.*, **56**(2), 127–150, doi:10.1175/1520-0469(1999)056<0127:SMOAMM>2.0.CO;2, 1999.
- Brasseur, G., J. Orlando, and G. Tyndall, eds., *Atmospheric chemistry and Global Change* (Oxford University Press, Oxford, UK, 1999), 654 pp.
- Bregman, B., A. Segers, M. Krol, E. Meijer, and P. van Velthoven, On the use of mass-conserving wind fields in chemistry-transport models, *Atmos. Chem. Phys.*, **3**, 447–457, doi:10.5194/acp-3-447-2003, 2003.
- Brinksma, E. J., *et al.*, The 2005 and 2006 DANDELIONS NO<sub>2</sub> and aerosol inter-comparison campaigns, *J. Geophys. Res.*, **113**, D16S46, doi:10.1029/2007JD008808, 2008.
- Brohede, S., *et al.*, A stratospheric NO<sub>2</sub> climatology from odin/OSIRIS limb-scatter measurements, *Can. J. Phys.*, **85**, 1253–1274, doi:10.1139/P07-141, 2007.
- Brook, R. D., *et al.*, Particulate matter air pollution and cardiovascular disease: An update to the scientific statement from the american heart association, *Circulation*, **121**, 2331–2378, doi:10.1161/CIR.0b013e3181dbee1, 2010.
- Bucsela, E. J., *et al.*, Algorithm for NO<sub>2</sub> Vertical Column Retrieval From the Ozone Monitoring Instrument, *IEEE Trans. Geosci. Remote Sens.*, **44**, 1245–1258, 2006.
- Bucsela, E. J., *et al.*, Comparison of tropospheric NO<sub>2</sub> from in-situ aircraft measurements with near-real time and standard product data from OMI, *J. Geophys. Res.*, **113**, D16S31, doi:10.1029/2007JD008838, 2008.
- Burrows, J. P., *et al.*, The Global Ozone Monitoring Experiment (GOME): mission concept and first scientific results, *J. Atmos. Sci.*, **56**, 151–175, doi:10.1175/1520-0469(1999)056<0151:TGOMEG>2.0.CO;2, 1999.
- Camy-Peyret, C., J.-M. Flaud, J. Laurent, and G. M. Stokes, First infrared measurement of atmospheric NO<sub>2</sub> from the ground, *Geophys. Res. Lett.*, **10**(1), 35–38, doi:10.1029/GL010i001p00035, 1983.
- Celarier, E. A., *et al.*, Validation of Ozone Monitoring Instrument nitrogen dioxide columns, *J. Geophys. Res.*, **113**, D15S15, doi:10.1029/2007JD008908, 2008.
- Chipperfield, M., Multiannual simulations with a three-dimensional chemical transport model, *J. Geophys. Res.*, **104**(D1), 1781–1805, doi:10.1029/98JD02597, 1999.
- Chipperfield, M. P., *et al.*, Analysis of UARS data in the southern polar vortex in September 1992 using a chemical transport model, *J. Geophys. Res.*, **101**, 18,861–18,881, doi:10.1029/96JD00936, 1996.
- Chu, W. P. and M. P. McCormick, SAGE observations of stratospheric nitrogen dioxide, *J. Geophys. Res.*, **91**(D5), 5465–5476, doi:10.1029/JD091iD05p05465, 1986.
- Clarke, M. R. B., The reduced major axis of a bivariate sample, *Biometrika*, **67**(2), 441–446, doi:10.1093/biomet/67.2.441, 1980.
- Coheur, P.-F., *et al.*, New water vapor line parameters in the 26000-13000 cm<sup>-1</sup> region, *J. Quant. Spectrosc. Radiat. Transfer*, **74**, 493–510, doi:10.1016/S0022-4073(01)00269-2, 2002.

- Colarco, P. R., *et al.*, Transport of smoke from canadian forest fires to the surface near Washington, D.C.: Injection height, entrainment, and optical properties, *J. Geophys. Res.*, **109**, D06203, doi:10.1029/2003JD004248, 2004.
- Cook, P. A. and H. K. Roscoe, Variability and trends in stratospheric NO<sub>2</sub> in Antarctic summer, and implications for stratospheric NO<sub>y</sub>, *Atmos. Chem. Phys.*, **9**, 3601–3612, doi:10.5194/acp-9-3601-2009, 2009.
- Cooper, O. R., *et al.*, Increasing springtime ozone mixing ratios in the free troposphere over western North America, *Nature*, **463**, 344–348, doi:10.1038/nature08708, 2010.
- Crutzen, P. J., The influence of nitrogen oxide on the atmospheric ozone content, *Quart. J. Roy. Met. Soc.*, **96**, 320–325, doi:10.1002/qj.49709640815, 1970.
- Crutzen, P. J., A discussion of the chemistry of some minor constituents in the stratosphere and troposphere, *Pure Appl. Geophys.*, **106**, 1385–1399, doi:10.1007/BF00881092, 1973.
- Damoah, R., *et al.*, Around the world in 17 days - hemispheric-scale transport of forest fire smoke from Russia in May 2003, *Atmos. Chem. Phys.*, **4**, 1311–1321, doi:10.5194/acp-4-1311-2004, 2004.
- Dave, J. V., Multiple scattering in a non-homogeneous, rayleigh atmosphere, *J. Atmos. Sci.*, **22**(3), 273–279, doi:10.1175/1520-0469(1965)022<0273:MSIANH>2.0.CO;2, 1965.
- de Graaf, M., P. Stammes, O. Torres, and R. B. A. Koelemeijer, Absorbing Aerosol Index - sensitivity analysis, application to GOME and comparison with TOMS, *J. Geophys. Res.*, **110**, D01201, doi:10.1029/2004JD005178, 2005.
- de Haan, J. F., P. B. Bosma, and J. W. Hovenier, The adding method for multiple scattering calculations of polarized light, *Astron. Astrophysics*, **183**, 371–391, 1987.
- de Laat, A. T. J., *et al.*, Scanning Imaging Absorption Spectrometer for Atmospheric Chartography carbon monoxide total columns: Statistical evaluation and comparison with chemistry transport model results, *J. Geophys. Res.*, **112**, D12310, doi:10.1029/2006JD008256, 2007.
- De Mazière, M., *et al.*, Quantitative evaluation of the post-Mount Pinatubo NO<sub>2</sub> reduction and recovery, based on 10 years of Fourier transform infrared and UV-visible spectroscopic measurements at Jungfraujoch, *J. Geophys. Res.*, **103**(D9), 10,849–10,858, doi:10.1029/97JD03362, 1998.
- de Rooij, W. A. and C. C. A. H. van der Stap, Expansion of Mie scattering matrices in generalized spherical functions, *Astron. Astrophysics*, **183**, 371–391, 1987.
- de Vries, J., *et al.*, Ozone Monitoring Instrument, in *Proceedings of SPIE*, volume 4480, doi:10.1117/12.453354, 2002.
- Denis, L., H. K. Roscoe, M. P. Chipperfield, M. Van Roozendael, and F. Goutail, A new software suite for NO<sub>2</sub> vertical profile retrieval from ground-based zenith-sky spectrometers, *J. Quant. Spectrosc. Radiat. Transfer*, **92**(3), 321–333, doi:10.1016/j.jqsrt.2004.07.030, 2005.
- Dentener, F., *et al.*, Interannual variability and trend of CH<sub>4</sub> lifetime as a measure

- for OH changes in the 1979-1993 time period, *J. Geophys. Res.*, **108**(D15), 4442, doi:10.1029/2002JD002916, 2003.
- Dirksen, R., M. Dobber, R. Voors, and P. Levelt, Prelaunch characterization of the Ozone Monitoring Instrument transfer function in the spectral domain, *Appl. Opt.*, **45**(17), 3972–3981, doi:10.1364/AO.45.003972, 2006.
- Dirksen, R., *et al.*, The on-ground calibration of the ozone monitoring instrument from scientific point of view, in *Proceedings of SPIE*, volume 5234, doi:10.1117/12.511484, 2004.
- Dirksen, R., *et al.*, Derivation of Ozone Monitoring Instrument tropospheric NO<sub>2</sub> in near-real time (DOMINO), Technical report, 2008, <http://www.knmi.nl/~eskes/projects/domino.html>.
- Dirksen, R. J., *et al.*, An aerosol boomerang: Rapid around-the-world transport of smoke from the December 2006 Australian forest fires observed from space, *J. Geophys. Res.*, **114**, D21201, doi:10.1029/2009JD012360, 2009.
- Dobber, M., R. Dirksen, R. Voors, G. H. Mount, and P. Levelt, Ground-based zenith sky abundances and in situ gas cross sections for ozone and nitrogen dioxide with the Earth Observing System Aura Ozone Monitoring Instrument, *Appl. Opt.*, **44**(14), 2846–2856, doi:10.1364/AO.44.002846, 2005.
- Dobber, M., *et al.*, Ozone Monitoring Instrument flight-model on-ground and in-flight calibration (European Space Agency (ESA), 2004).
- Dobber, M., *et al.*, Validation of Ozone Monitoring Instrument level 1b data products, *J. Geophys. Res.*, **113**, D15S06, doi:10.1029/2007JD008665, 2008.
- Dobber, M. R., *et al.*, Ozone Monitoring Instrument Calibration, *IEEE Trans. Geosci. Remote Sens.*, **44**(5), 1209–1238, 2006.
- Douglass, A. R., M. R. Schoeberl, R. B. Rood, and S. Pawson, Evaluation of transport in the lower tropical stratosphere in a global chemistry and transport model, *J. Geophys. Res.*, **108**(D9), 4259, doi:10.1029/2002JD002696, 2003.
- Dubovik, O., *et al.*, Variability of Absorption and Optical Properties of Key Aerosol Types Observed in Worldwide Locations, *J. Atmos. Sci.*, **59**, 590–608, doi:10.1175/1520-0469(2002)059<0590:VOAAOP>2.0.CO;2, 2002.
- Dunkerton, T. J., Quasi-Biennial and Subbiennial Variations of Stratospheric Trace Constituents Derived from HALOE Observations, *J. Atmos. Sci.*, **58**(1), 7–25, doi:10.1175/1520-0469(2001)058<0007:QBASVO>2.0.CO;2, 2001.
- Edwards, D. P., *et al.*, Satellite-observed pollution from Southern Hemisphere biomass burning, *J. Geophys. Res.*, **111**, D14312, doi:10.1029/2005JD006655, 2006.
- Eskes, H. J. and K. F. Boersma, Averaging kernels for DOAS total-column satellite retrievals, *Atmos. Chem. Phys.*, **3**, 1285–1291, doi:10.5194/acp-3-1285-2003, 2003.
- Eskes, H. J., P. F. J. van Velthoven, P. Valks, and H. M. Kelder, Assimilation of GOME total ozone satellite observations in a three-dimensional tracer transport model, *Quart. J. Roy. Meteorol. Soc.*, **129**(590), 1663–1681, doi:10.1256/qj.02.14, 2003.
- Fally, S., *et al.*, Water vapor line broadening and shifting by air in the 26,000-13,000 cm<sup>-1</sup> region, *J. Quant. Spectrosc. Radiat. Transfer*, **82**, 119–131, doi:10.1016/S0022-

- 4073(03)00149-3, 2003.
- Fishman, J., V. Ramanathan, P. J. Crutzen, and S. C. Liu, Tropospheric ozone and climate, *Nature*, **282**, 818–820, doi:10.1038/282818a0, 1979.
- Flaud, J.-M., C. Camy-Peyret, D. Cariolle, J. Laurent, and G. M. Stokes, Daytime variation of atmospheric NO<sub>2</sub> from ground based infrared measurements, *Geophys. Res. Lett.*, **10**(11), 1104–1107, doi:10.1029/GL010i011p01104, 1983.
- Forster, C., *et al.*, Transport of boreal forest fire emissions from Canada to Europe, *J. Geophys. Res.*, **106**, 22,887–22,906, doi:10.1029/2001JD900115, 2001.
- Fortuin, J. P. F. and H. M. Kelder, An ozone climatology base on ozonesonde and satellite measurements, *J. Geophys. Res.*, **103**, 31,709–31,734, doi:10.1029/1998JD200008, 1998.
- Freitas, S. R., K. M. Longo, and M. O. Andreae, Impact of including the plume rise of vegetation fires in numerical simulations of associated atmospheric pollutants, *Geophys. Res. Lett.*, **33**, L17808, doi:10.1029/2006GL026608, 2006.
- Freitas, S. R., *et al.*, Including the sub-grid scale plume rise of vegetation fires in low resolution atmospheric transport models, *Atmos. Chem. Phys.*, **7**, 3385–3398, doi:10.5194/acp-7-3385-2007, 2007.
- Fromm, M., A. Tupper, D. Rosenfeld, R. Servranckx, and R. McRae, Violent pyroconvective storm devastates Australia's capital and pollutes the stratosphere, *Geophys. Res. Lett.*, **33**, L05815, doi:10.1029/2005GL025161, 2006.
- Fromm, M., *et al.*, Pyro-cumulunimbus injection of smoke to the stratosphere: Observations and impact of a super blowup in northwestern Canada on 3-4 August 1998, *J. Geophys. Res.*, **110**, D08205, doi:10.1029/2004JD005350, 2005.
- Fromm, M. D. and R. Servranckx, Transport of forest fire smoke above the tropopause by supercell convection, *Geophys. Res. Lett.*, **30**(10), 1542, doi:10.1029/2002GL016820, 2003.
- Funk, J. P. and G. L. Garnham, Australian ozone observations and a suggested 24-month cycle, *Tellus*, **14**, 378–382, 1962.
- Giglio, L., J. Desloîtres, C. Justice, and Y. Kaufman, An enhanced contextual fire detection algorithm for MODIS, *Remote Sens. Environ.*, **87**, 273–282, doi:10.1016/S0034-4257(03)00184-6, 2003.
- Gil, M., *et al.*, NO<sub>2</sub> climatology in the northern subtropical region: diurnal, seasonal and interannual variability, *Atmos. Chem. Phys.*, **8**, 1635–1648, doi:10.5194/acp-8-1635-2008, 2008.
- Gloudemans, A. M. S., *et al.*, Evidence for Long-range Transport of Carbon Monoxide in the Southern Hemisphere from SCIAMACHY observations, *Geophys. Res. Lett.*, **33**, L16807, doi:10.1029/2006GL026804, 2006.
- Gordley, L. L., *et al.*, Validation of nitric oxide and nitrogen dioxide measurements made by the Halogen Occultation Experiment for UARS platform, *J. Geophys. Res.*, **101**(D6), 10,241–10,266, doi:10.1029/95JD02143, 1996.
- Gotz, F. W. P., A. R. Meetham, and G. M. B. Dobson, The Vertical Distribution of Ozone in the Atmosphere, *Proc. R. Soc. London, Ser. A*, **145**, 416–446, 1934.

- Goutail, F., J. P. Pommereau, A. Sarkissian, E. Kyro, and V. Dorokhov, Total nitrogen dioxide at the Arctic polar circle since 1990, *Geophys. Res. Lett.*, **21**(13), 1371–1374, doi:10.1029/93GL01783, 1994.
- Gruzdev, A. N., Latitudinal dependence of variations in stratospheric NO<sub>2</sub> content, *Izvestiya, Atmospheric and Oceanic Physics*, **44**(3), 319–333, doi:10.1134/S0001433808030079, 2008.
- Gruzdev, A. N. and A. S. Elokhov, Validating NO<sub>2</sub> Measurements in the Vertical Atmospheric Column with the OMI Instrument aboard the EOS Aura Satellite against Ground-Based Measurements at the Zvenigorod Scientific Station, *Izvestiya, Atmospheric and Oceanic Physics*, **45**(4), 444–455, 2009.
- Haagen-Smit, A. J. and M. M. Fox, Photochemical ozone formation with hydrocarbons and automobile exhaust, *J. Air Waste Manag. Assoc.*, **4**, 105–109, 1954.
- Hains, J., *et al.*, Testing and improving OMI DOMINO Tropospheric NO<sub>2</sub> Using Observations from the DANDELIONS and INTEX-B Validation Campaigns, *J. Geophys. Res.*, **115**, D05301, doi:10.1029/2009JD012399, 2010.
- Heney, L. G. and J. L. Greenstein, Diffuse radiation in the galaxy, *Astrophys. J.*, **93**, 70–83, 1941.
- Herman, J. R. and E. Celarier, Earth surface reflectivity climatology at 340–380 nm from TOMS data, *J. Geophys. Res.*, **102**(D23), 28,003–28,012, doi:10.1029/97JD02074, 1997.
- Herman, J. R., *et al.*, Global distribution of UV-absorbing aerosols from Nimbus 7/TOMS data, *J. Geophys. Res.*, **102**(D14), 16,911–16,922, doi:10.1029/96JD03680, 1997.
- Herron-Thorpe, F. L., B. K. Lamb, G. H. Mount, and J. K. Vaughan, Evaluation of a regional air quality forecast model for tropospheric NO<sub>2</sub> columns using the OMI/Aura satellite tropospheric NO<sub>2</sub> product, *Atmos. Chem. Phys.*, **10**, 8839–8854, doi:10.5194/acp-10-8839-2010, 2010.
- Hofmann, D., *et al.*, Intercomparison of UV/visible spectrometers for measurements of stratospheric NO<sub>2</sub> for the Network for the Detection of Stratospheric Change, *J. Geophys. Res.*, **100**(D8), 10.1029/95JD00620, 1995.
- Houweling, S., F. Dentener, and J. Lelieveld, The impact of nonmethane hydrocarbon compounds on tropospheric photochemistry, *J. Geophys. Res.*, **103**(D9), 10,673–10,696, doi:10.1029/97JD03582, 1998.
- Huijnen, V., *et al.*, Comparison of OMI NO<sub>2</sub> tropospheric columns with an ensemble of global and European regional air quality models, *Atmos. Chem. Phys.*, **10**, 3273–3296, doi:10.5194/acp-10-3273-2010, 2010.
- Hvidberg, M. and J. Brandt, Using OMI data to improve air quality forecast - does it work?, EGU2009-2943, presented at EGU General Assembly 2009, Vienna, Austria, 2009.
- Hyer, E. J., D. J. Allen, and E. S. Kasischke, Examining injection properties of boreal forest fires using surface and satellite measurements of CO transport, *J. Geophys. Res.*, **112**, D18307, doi:10.1029/2006JD008232, 2007.

- Ionov, D. V., *et al.*, Ground-based validation of EOS-Aura OMI NO<sub>2</sub> vertical column data in the midlatitude mountain ranges of Tien Shan (Kyrgyzstan) and Alps (France), *J. Geophys. Res.*, **113**, D15S08, doi:10.1029/2007JD008659, 2008.
- Intergovernmental Panel on Climate Change (IPCC), *Climate Change 2007: The Physical Science Basis. Contribution of Working Group I to the Fourth Assessment Report of the Intergovernmental Panel on Climate Change* (Cambridge University Press, Cambridge, United Kingdom and New York, NY, USA), 996 pp, 2007.
- Jacob, D. J., J. A. Logan, and P. P. Murti, Effect of rising Asian emissions on surface ozone in the United States, *Geophys. Res. Lett.*, **26**(14), 2175–2178, doi:10.1029/1999GL900450, 1999.
- Kahn, R. A., *et al.*, Aerosol source plume physical characteristics from space-based multiangle imaging, *J. Geophys. Res.*, **112**, D11205, doi:10.1029/2006JD007647, 2007.
- Kahn, R. A., *et al.*, Wildfire smoke injection heights: Two perspectives from space, *Geophys. Res. Lett.*, **35**, L04809, doi:10.1029/2007GL032165, 2008.
- Kalnay, E., *et al.*, The NCEP/NCAR 40-year reanalysis project, *Bull. Amer. Meteor. Soc.*, **77**, 437–471, doi:10.1175/1520-0477(1996)077<0437:TNYRP>2.0.CO;2, 1996.
- Kerzenmacher, T., *et al.*, Validation of NO<sub>2</sub> and NO from the Atmospheric Chemistry Experiment (ACE), *Atmos. Chem. Phys.*, **8**, 5801–5841, doi:10.5194/acp-8-5801-2008, 2008.
- Kim, S.-W., *et al.*, Validation of aerosol and cloud layer structures from the spaceborne lidar CALIOP using a ground-based lidar in Seoul, Korea, *Atmos. Chem. Phys.*, **8**, 3705–3720, doi:10.5194/acp-8-3705-2008, 2008.
- Kleipool, Q. L., M. R. Dobber, J. F. de Haan, and P. F. Levelt, Earth surface reflectance climatology from 3 years of OMI data, *J. Geophys. Res.*, **113**, D18308, doi:10.1029/2008JD010290, 2008.
- Koelemeijer, R. B. A., J. F. de Haan, and P. Stammes, A database of spectral surface reflectivity in the range 335–772 nm derived from 5.5 years of GOME observations, *J. Geophys. Res.*, **108**, doi:10.1029/2002JD002429, 2003.
- Koelemeijer, R. B. A., P. Stammes, J. W. Hovenier, and J. F. de Haan, A fast method for retrieval of cloud parameters using oxygen A band measurements from the Global Ozone Monitoring Instrument, *J. Geophys. Res.*, **106**, 3475–3490, doi:10.1029/2000JD900657, 2001.
- Kroon, M., *et al.*, Ozone Monitoring Instrument geolocation verification, *J. Geophys. Res.*, **113**, D15S12, doi:10.1029/2007JD008821, 2008.
- Krotkov, N. A., S. A. Carn, A. J. Krueger, P. K. Bhartia, and K. Yang, Band residual difference algorithm for retrieval of SO<sub>2</sub> from the AURA Ozone Monitoring Instrument (OMI), *IEEE Trans. Geosci. Remote Sens.*, **44**(5), 1259–1266, doi:10.1109/TGRS.2005.861932, 2006.
- Kurosu, T. P., K. Chance, and C. E. Sioris, Preliminary results for HCHO and BrO from the EOS-Aura Ozone Monitoring Instrument, in *Proceedings of SPIE*, volume



- 5652, pp. 116–123, doi:10.1117/12.578606, 2004.
- Kurosu, T. P., K. Chance, and R. Volkamer, Global measurements of OCIO, BrO, HCHO, and CHO-CHO from the Ozone Monitoring Instrument on EOS Aura (AGU, 2005).
- Kurucz, R., I. Furenlid, J. Brault, and L. Testerman, *Solar flux atlas from 296 to 1300 nm* (1984).
- Kyrölä, E., *et al.*, GOMOS O<sub>3</sub>, NO<sub>2</sub>, and NO<sub>3</sub> observations in 2002–2008, *Atmos. Chem. Phys.*, **10**, 7723–7738, doi:10.5194/acp-10-7723-2010, 2010.
- Laan, E. C., *et al.*, Toward the use of the ozone monitoring instrument (OMI), in *Proceedings of SPIE*, volume 4540, pp. 270–277, doi:10.1117/12.450669, 2001.
- Labonne, M., F.-M. Bréon, and F. Chevallier, Injection height of biomass burning aerosols as seen from a spaceborne lidar, *Geophys. Res. Lett.*, **34**, L11806, doi:10.1029/2007GL029311, 2007.
- Lamsal, L. N., *et al.*, Indirect validation of tropospheric nitrogen dioxide retrieved from the OMI satellite instrument: Insight into the seasonal variation of nitrogen oxides at northern midlatitudes, *J. Geophys. Res.*, **115**, D05302, doi:10.1029/2009JD013351, 2010.
- Lavoué, D., C. Lioussé, H. Cachier, B. J. Stocks, and J. G. Goldammer, Modeling of carbonaceous particles emitted by boreal and temperate wildfires at northern latitudes, *J. Geophys. Res.*, **105**(D22), 26,871–26,890, doi:10.1029/2000JD900180, 2000.
- Leue, C., *et al.*, Quantitative analysis of NO<sub>x</sub> emissions from Global Ozone Monitoring Experiment satellite image sequences, *J. Geophys. Res.*, **106**, 5493–5505, doi:10.1029/2000JD900572, 2001.
- Leung, F.-Y. T., *et al.*, Impacts of enhanced biomass burning in the boreal forests in 1998 on tropospheric chemistry and the sensitivity of model results to the injection height of emissions, *J. Geophys. Res.*, **112**, D10313, doi:10.1029/2006JD008132, 2007.
- Levelt, P. F., *et al.*, The Ozone Monitoring Instrument, *IEEE Trans. Geosci. Remote Sens.*, **44**(5), 1093–1101, doi:10.1109/TGRS.2006.872333, 2006a.
- Levelt, P. F., *et al.*, Science Objectives of the Ozone Monitoring Instrument, *IEEE Trans. Geosci. Remote Sens.*, **44**(5), 1199–1208, doi:10.1109/TGRS.2006.872336, 2006b.
- Liley, J. B., P. V. Johnston, R. L. McKenzie, A. J. Thomas, and I. S. Boyd, Stratospheric NO<sub>2</sub> variations from a long time series at Lauder, New Zealand, *J. Geophys. Res.*, **105**(D9), 11,633–11,640, doi:10.1029/1999JD901157, 2000.
- Manney, G. L., *et al.*, EOS Microwave Limb Sounder observations of “frozen-in” anticyclonic air in Arctic summer, *Geophys. Res. Lett.*, **33**, L06810, doi:10.1029/2005GL025418, 2006.
- Martin, R. V., *et al.*, An improved retrieval of tropospheric nitrogen dioxide from GOME, *J. Geophys. Res.*, **107**, doi:10.1029/JD001027, 2002a.
- Martin, R. V., *et al.*, Interpretation of TOMS observations of tropical tropospheric

- ozone with a global model and in situ observations, *J. Geophys. Res.*, **107**(D18), 4351, doi:10.1029/2001JD001480, 2002b.
- Mateer, C. L. and J. J. Deluisi, A new Umkehr inversion algorithm, *J. Atmos. Terr. Phys.*, **54**, 537–556, doi:10.1016/0021-9169(92)90095-3, 1992.
- Mazzoni, D., *et al.*, A data-mining approach to associating MISR smoke plume heights with MODIS fire measurements, *Remote Sens. Environ.*, **107**, 138–148, doi:10.1016/j.rse.2006.08.014, 2007.
- McGill, M. J., *et al.*, Airborne validation of spatial properties measured by the CALIPSO lidar, *J. Geophys. Res.*, **112**, D20201, doi:10.1029/2007JD008768, 2007.
- McPeters, R., *et al.*, *Earth probe total ozone mapping spectrometer (TOMS) data product user's guide* (National Aeronautics and Space Administration, Goddard Space Flight Center ; National Technical Information Service, distributor, Greenbelt, MD, USA, 1998), 1 v. pp.
- Mijling, B., *et al.*, Reductions of NO<sub>2</sub> detected from space during the 2008 Beijing Olympic Games, *Geophys. Res. Lett.*, **36**, L13801, doi:10.1029/2009GL038943, 2009.
- Mitchell, R. M., D. M. O'Brien, and S. K. Campbell, Characteristics and radiative impact of the aerosol generated by the Canberra firestorm of January 2003, *J. Geophys. Res.*, **111**, D02204, doi:10.1029/2005JD006304, 2006.
- Molina, L. T. and M. J. Molina, Production of Cl<sub>2</sub>O<sub>2</sub> from the self-reaction of the chlorine oxide (ClO) radical, *J. Phys. Chem.*, **91**, 433–436, doi:10.1021/j100286a035, 1987.
- Molina, M. J. and F. S. Rowland, Stratospheric sink for chlorofluoromethanes: Chlorine atom-catalysed destruction of ozone, *Nature*, **249**, 810–812, doi:10.1038/249810a0, 1974.
- Mount, G. H., D. W. Rusch, J. F. Noxon, J. M. Zawodny, and C. A. Barth, Measurements of Stratospheric NO<sub>2</sub> From the Solar Mesosphere Explorer Satellite 1. An Overview of the Results, *J. Geophys. Res.*, **89**(D1), 1327–1340, doi:10.1029/JD089iD01p01327, 1984.
- Mount, G. H., R. Sanders, A. Schmeltekopf, and S. Solomon, Visible Spectroscopy at McMurdo Station, Antarctica 1. Overview and Daily Variations of NO<sub>2</sub> and O<sub>3</sub>, Austral Spring, 1986, *J. Geophys. Res.*, **92**(D7), 8320–8328, doi:10.1029/JD092iD07p08320, 1987.
- Mount, G. H., G. Yamasaki, W. Fowler, and W. G. Fastie, Compact far ultraviolet emission source with rich spectral emission 1150–3100 Å, *Appl. Opt.*, **16**(3), 591–595, doi:10.1364/AO.16.000591, 1977.
- Munro, R., *et al.*, GOME-2 on MetOp, in: Proc. of the 2006 EUMETSAT Meteorological Satellite Conference, Helsinki, Finland, 2006.
- Naudet, J.-P., R. Thomas, D. Rusch, and R. Clancy, Distribution of Stratospheric NO<sub>2</sub> at 10 mbar: SME Global Morphology and Comparison to LIMS Observations, *J. Geophys. Res.*, **92**(D8), 9863–9867, doi:10.1029/JD092iD08p09863, 1987.
- Noxon, J. F., Stratospheric NO<sub>2</sub> 2. Global Behavior, *J. Geophys. Res.*, **84**(C8), 5067–

- 5076, doi:10.1029/JC084iC08p05067, 1979.
- Olivier, J., *et al.*, Present and future surface emissions of atmospheric compounds, POET Report #2, EU project EVK2-1999-00011, 2003.
- Palmer, P. I., *et al.*, Air mass factor formulation for spectroscopic measurements from satellites: Application to formaldehyde retrievals from the Global Ozone Monitoring Experiment, *J. Geophys. Res.*, **106**(D13), 14,539–14,550, doi:10.1029/2000JD900772, 2001.
- Peters, W., *et al.*, Toward regional-scale modeling using the two-way nested global model TM5: Characterization of transport using SF<sub>6</sub>, *J. Geophys. Res.*, **109**, D19314, doi:10.1029/2004JD005020, 2004.
- Pickering, K. E., *et al.*, Convective transport of biomass burning emissions over Brazil during TRACE A, *J. Geophys. Res.*, **101**(D19), 23,993–24,012, doi:10.1029/96JD00346, 1996.
- Pinardi, G., *et al.*, On the use of the MAXDOAS technique for the validation of tropospheric NO<sub>2</sub> column measurements from satellite, in: Proc. of the 2008 EUMETSAT Meteorological Satellite Conference, Darmstadt, Germany, 2008.
- Plane, J. and N. Smith, *Advances in spectroscopy*, volume 24, chapter Atmospheric Monitoring by differential optical absorption spectroscopy in environmental science (John Wiley, Hoboken, N.J., 1994).
- Platt, U., *Air Monitoring by Spectroscopic Techniques*, *Chem. Anal. Ser.*, volume 127, chapter Differential optical absorption spectroscopy (DOAS), pp. 27–84 (John Wiley, Hoboken, N.J., 1994).
- Platt, U. and J. Stutz, *Differential Optical Absorption Spectroscopy, Principles and Applications*, Physics of Earth and Space Environments (Springer Verlag, Heidelberg, Germany, 2008), 597 pp., doi:10.1007/978-3-540-75776-4.
- Pommereau, J. P. and F. Goutail, O<sub>3</sub> and NO<sub>2</sub> ground-based measurements by visible spectrometry during Arctic winter and spring 1988, *Geophys. Res. Lett.*, **15**, 891–894, doi:10.1029/GL015i008p00891, 1988.
- Qin, Y. and R. M. Mitchell, Characterisation of episodic aerosol types over the Australian continent, *Atmos. Chem. Phys.*, **9**, 1943–1956, doi:10.5194/acp-9-1943-2009, 2009.
- Randall, C. E., D. W. Rusch, R. M. Bevilacqua, K. W. Hoppel, and J. D. Lumpe, Polar Ozone and Aerosol Measurement (POAM) II stratospheric NO<sub>2</sub> 1993-1996, *J. Geophys. Res.*, **103**(D21), 28,361–28,371, doi:10.1029/98JD02092, 1998.
- Randel, W. J. and F. Wu, Isolation of the Ozone QBO in SAGE II Data by Singular-Value Decomposition, *J. Atmos. Sci.*, **53**(17), 2546–2559, doi:10.1175/1520-0469(1996)053<2546:IOTOQI>2.0.CO;2, 1996.
- Ravishankara, A. R., J. S. Daniel, and R. W. Portmann, Nitrous Oxide (N<sub>2</sub>O): The Dominant Ozone-Depleting Substance Emitted in the 21st Century, *Science*, **326**(5949), 123–125, doi:10.1126/science.1176985, 2009.
- Reed, R., W. Campbell, L. Rasmussen, and D. Rogers, Evidence of a Downward-Propagating, Annual Wind Reversal in the Equatorial Stratosphere, *J. Geophys.*

- Res.*, **66**, 813–818, doi:10.1029/JZ066i003p00813, 1961.
- Richter, A. and J. P. Burrows, Tropospheric NO<sub>2</sub> from GOME measurements, *Adv. Space Res.*, **29**, 1673–1683, doi:10.1016/S0273-1177(02)00100-X, 2002.
- Richter, A., J. P. Burrows, H. Nüß, C. Granier, and U. Niemeier, Increase in tropospheric nitrogen dioxide over China observed from space, *Nature*, **437**, 129–132, doi:10.1038/nature04092, 2005.
- Rinsland, C. P., *et al.*, Post-Mount Pinatubo eruption ground-based infrared stratospheric column measurements of HNO<sub>3</sub>, NO, and NO<sub>2</sub> and their comparison with model calculations, *J. Geophys. Res.*, **108**(D5), 4437, doi:10.1029/2002JD002965, 2003.
- Roscoe, H. K., *et al.*, Slant Column Measurements of O<sub>3</sub> and NO<sub>2</sub> During the NDSC Intercomparison of Zenith-Sky UV-Visible Spectrometers in June 1996, *J. Atmos. Chem.*, **32**, 281–314, doi:10.1023/A:1006111216966, 1999.
- Rosenlof, K. H., Summer hemisphere differences in temperature and transport in the lower stratosphere, *J. Geophys. Res.*, **101**(D14), 19,129–19,136, doi:10.1029/96JD01542, 1996.
- Ryerson, T., E. Williams, and F. Fehsenfeld, An efficient photolysis system for fast-response NO<sub>2</sub> measurements, *J. Geophys. Res.*, **105**(D21), 26,447–26,461, doi:10.1029/2000JD900389, 2000.
- Sarkissian, A., *et al.*, Ozone and NO<sub>2</sub> air-mass factors for zenith-sky spectrometers: Intercomparison of calculations with different radiative transfer models, *Geophys. Res. Lett.*, **22**(9), 1113–1116, doi:10.1029/95GL01032, 1995.
- Sassi, F. and M. Salby, Diurnal variations in the middle atmosphere observed by UARS, *J. Geophys. Res.*, **104**(D3), 3729–3739, doi:10.1029/1998JD100068, 1999.
- Schaap, M., K. Müller, and H. M. t. Brink, Constructing the european aerosol nitrate concentration field from quality analysed data, *Atmospheric Environment*, **36**(8), 1323–1335, doi:10.1016/S1352-2310(01)00556-8, 2002.
- Segers, A., P. van Velthoven, B. Bregman, and M. Krol, On the computation of mass fluxes for Eulerian transport models from spectral meteorological fields, in P. M. A. Sloot, A. G. Hoekstra, C. J. K. Tan, and J. J. Dongarra, eds., *Proceedings of the 2002 International Conference on Computational Science*, volume 2330, pp. 767–776, Lect. Notes Comput. Sci. (Springer-Verlag, New York, 2002).
- Singh, H. B., W. H. Brune, J. H. Crawford, F. Flocke, and D. J. Jacob, Chemistry and transport of pollution over the Gulf of Mexico and the Pacific: Spring 2006 INTEX-B Campaign overview and first results, *Atmos. Chem. Phys.*, **9**, 2301–2318, doi:10.5194/acp-9-2301-2009, 2009.
- Singleton, C. S., *et al.*, Quantifying Arctic ozone loss during the 2004–2005 winter using satellite observations and a chemical transport model, *J. Geophys. Res.*, **112**, D07304, doi:10.1029/2006JD007463, 2007.
- Sinha, P., L. Jaeglé, P. V. Hobbs, and Q. Liang, Transport of biomass burning emissions from southern Africa, *J. Geophys. Res.*, **109**, D20204, doi:10.1029/2004JD005044, 2004.

- Siskind, D. E., S. D. Eckermann, J. P. McCormack, M. J. Alexander, and J. T. Bacmeister, Hemispheric differences in the temperature of the summertime stratosphere and mesosphere, *J. Geophys. Res.*, **108**(D2), 4051, doi:10.1029/2002JD002095, 2003.
- Smorenburg, K., M. R. Dobber, E. Schenkeveld, R. Vink, and H. Visser, Slit function measurement optical stimulus, in *Proceedings of SPIE*, volume 4881, pp. 511–520, doi:10.1117/12.462482, 2003.
- Sneep, M., *et al.*, Three-way comparison between OMI and PARASOL cloud pressure products, *J. Geophys. Res.*, **113**, D15S23, doi:10.1029/2007JD008694, 2008.
- Solomon, S., Stratospheric ozone depletion: A review of concepts and history, *Rev. Geophys.*, **37**(3), 275–316, doi:10.1029/1999RG900008, 1999.
- Solomon, S. and J. Keys, Seasonal Variations in Antarctic NO<sub>x</sub> Chemistry, *J. Geophys. Res.*, **97**(D8), 7971–7978, doi:10.1029/91JD01707, 1992.
- Solomon, S., G. Mount, and J. Zawodny, Measurements of Stratospheric NO<sub>2</sub> From the Solar Mesosphere Explorer Satellite 2. General Morphology of Observed NO<sub>2</sub> and Derived N<sub>2</sub>O<sub>5</sub>, *J. Geophys. Res.*, **89**(D5), 7317–7321, doi:10.1029/JD089iD05p07317, 1984.
- Spichtinger, N., *et al.*, Satellite Detection of a Continental-Scale Plume of Nitrogen Oxides from Boreal Forest Fires, *Geophys. Res. Lett.*, **28**(24), 4579–4582, doi:10.1029/2001GL013484, 2001.
- Stammes, P., Spectral radiance modeling in the UV-Visible range, in W. Smith and Y. Timofeyev, eds., *IRS 2000: Current problems in atmospheric radiation*, pp. 385–388 (A. Deepak Publishing, Hampton (VA), 2001).
- Stammes, P., J. F. de Haan, and J. W. Hovenier, The polarized internal radiation field of a planetary atmosphere, *Astron. Astrophys.*, **225**, 239–259, 1989.
- Stammes, P., L. G. Tilstra, R. Braak, M. de Graaf, and E. A. A. Aben, Estimate of Solar Radiative Forcing by Polluted Clouds Using OMI and SCIAMACHY Satellite Data, in T. Nakajima and M. A. Yamasoe, eds., *AIP Conference Proceedings*, volume 1100, pp. 577–580 (2009), doi:10.1063/1.3117051.
- Stammes, P., *et al.*, Effective cloud fractions from the Ozone Monitoring Instrument: Theoretical framework and validation,, *J. Geophys. Res.*, **113**, D16S38, doi:10.1029/2007JD008820, 2008.
- Staudt, A. C., *et al.*, Global chemical model analysis of biomass burning and lightning influences over the South Pacific in austral spring, *J. Geophys. Res.*, **107**(D14), 4200, doi:10.1029/2000JD000296, 2002.
- Stein, D. C., *et al.*, Haze layer characterization and associated meteorological controls along the eastern coastal region of southern Africa, *J. Geophys. Res.*, **108**(D13), 8506, doi:10.1029/2002JD003237, 2003.
- Steinbacher, M., *et al.*, Nitrogen oxide measurements at rural sites in Switzerland: Bias of conventional measurement techniques, *J. Geophys. Res.*, **112**, D11307, doi:10.1029/2006JD007971, 2007.
- Stolarski, R. S. and R. J. Cicerone, Stratospheric chlorine: A possible sink for ozone,

- Can. J. Chem.*, **52**, 1610–1615, doi:10.1139/v74-233, 1974.
- Sussmann, R., *et al.*, Stratospheric and tropospheric NO<sub>2</sub> variability on the diurnal and annual scale: a combined retrieval from ENVISAT/SCIAMACHY and solar FTIR at the Permanent Ground-Truthing Facility Zugspitze/Garmisch, *Atmos. Chem. Phys.*, **5**, 2657–2677, doi:10.5194/acp-5-2657-2005, 2005.
- The Royal Society, Ground-level ozone in the 21st century: Future trends, impacts and policy implications, *Royal Society policy document 15/08*, **RS1276**, 2008, ([http://royalsociety.org/Report\\_WF.aspx?pageid=7924&terms=ground-level+ozone](http://royalsociety.org/Report_WF.aspx?pageid=7924&terms=ground-level+ozone)).
- Thornton, J. A., P. J. Wooldridge, and R. C. Cohen, Atmospheric NO<sub>2</sub>: In situ laser-induced fluorescence detection at parts per trillion mixing ratios, *Anal. Chem.*, **72**(3), 528–539, doi:10.1021/ac9908905, 2000.
- Torres, O., *et al.*, Aerosols and surface UV products from Ozone Monitoring Instrument observations: An overview, *J. Geophys. Res.*, **112**, D24S47, doi:10.1029/2007JD008809, 2007.
- Turquety, S., *et al.*, Tracking the emission and transport of pollution from wildfires using the IASI CO retrievals: analysis of the summer 2007 Greek fires, *Atmos. Chem. Phys.*, **9**, 4897–4913, doi:10.5194/acp-9-4897-2009, 2009.
- van den Oord, G. H. J., *et al.*, OMI Level 0 to 1B Processing and Operational Aspects, *IEEE Trans. Geosci. Remote Sens.*, **44**(5), 1380–1397, doi:10.1109/TGRS.2006.872935, 2006.
- van der A, R. J., M. A. F. Allaart, and H. J. Eskes, Multi sensor reanalysis of total ozone, *Atmos. Chem. Phys.*, **10**, 11,277–11,294, doi:10.5194/acp-10-11227-2010, 2010.
- van der Werf, G. R., *et al.*, Interannual variability in global biomass burning emissions from 1997 to 2004, *Atmos. Chem. Phys.*, **6**, 3423–3441, doi:10.5194/acp-6-3423-2006, 2006.
- Van Roozendaal, M., *et al.*, Ground-based stratospheric NO<sub>2</sub> monitoring at Keflavik (Iceland) during EASOE, *Geophys. Res. Lett.*, **21**(13), 1379–1382, doi:10.1029/93GL02433, 1994.
- Vandaele, A. C., *et al.*, Measurements of the NO<sub>2</sub> absorption cross-section from 42 000 cm<sup>-1</sup> to 10 000 cm<sup>-1</sup> (238–1000 nm) at 220 k and 294 k, *Journal of Quantitative Spectroscopy and Radiative Transfer*, **59**(3-5), 171–184, doi:10.1016/S0022-4073(97)00168-4, 1998.
- Vandaele, A. C., *et al.*, An intercomparison campaign of ground-based UV-visible measurements of NO<sub>2</sub>, BrO, and OClO slant columns: Methods of analysis and results for NO<sub>2</sub>, *J. Geophys. Res.*, **110**, D08305, doi:10.1029/2004JD005423, 2005.
- Vaughan, G., *et al.*, An intercomparison of ground-based UV-visible sensors of ozone and NO<sub>2</sub>, *J. Geophys. Res.*, **102**(D1), 1411–1422, doi:10.1029/96JD00515, 1997.
- Vaughan, G., *et al.*, SAOZ measurements of NO<sub>2</sub> at Aberystwyth, *J. Environ. Monit.*, **8**, 353–361, doi:10.1039/b511482a, 2006.
- Veefkind, J. P., J. F. de Haan, E. J. Brinksma, M. Kroon, and P. F. Levelt, Total ozone

- from the Ozone Monitoring Instrument (OMI) using the DOAS technique, *IEEE Trans. Geosci. Remote Sens.*, **44**(5), 1239–1244, doi:10.1109/TGRS.2006.871204, 2006.
- Veihelmann, B., P. F. Levelt, P. Stammes, and J. P. Veefkind, Simulation study of the aerosol information content in OMI spectral reflectance measurements, *Atmos. Chem. Phys.*, **7**, 3115–3127, doi:10.5194/acp-7-3115-2007, 2007.
- Volten, H., *et al.*, NO<sub>2</sub> Lidar Profile Measurements for Satellite Interpretation and Validation, *J. Geophys. Res.*, **114**, D24301, doi:10.1029/2009JD012441, 2009.
- Wagner, T., *et al.*, MAX-DOAS O<sub>4</sub> measurements: A new technique to derive information on atmospheric aerosols-Principles and information content, *J. Geophys. Res.*, **109**, D22205, doi:10.1029/2004JD004904, 2004.
- Wang, Y., M. B. McElroy, K. F. Boersma, H. J. Eskes, and J. P. Veefkind, Traffic restrictions associated with the Sino-African summit: Reductions of NO<sub>x</sub> detected from space, *Geophys. Res. Lett.*, **34**, doi:10.1029/2007GL029326, 2007.
- Waters, J. W., *et al.*, The UARS and EOS Microwave Limb Sounder Experiments, *J. Atmos. Sci.*, **56**, 194–218, doi:10.1175/1520-0469(1999)056<0194:TUAEML>2.0.CO;2, 1999.
- Wayne, R. P., *Chemistry of Atmospheres* (Oxford Univ. Press, Oxford, UK, 2000), 3 edition, 775 pp.
- Wenig, M., *et al.*, Intercontinental transport of nitrogen oxide pollution plumes, *Atmos. Chem. Phys.*, **3**, 387–393, doi:10.5194/acp-3-387-2003, 2003.
- Wenig, M., *et al.*, Retrieval and analysis of stratospheric NO<sub>2</sub> from the Global Ozone Monitoring Experiment, *J. Geophys. Res.*, **109**, D04315, doi:10.1029/2003JD003652, 2004.
- Winker, D. M., J. R. Pelon, and M. P. McCormick, The CALIPSO mission: spaceborne lidar for observation of aerosols and clouds, in *Proceedings of SPIE*, volume 4893, pp. 1–11, doi:10.1117/12.466539, 2003.
- Wittrock, F., *et al.*, MAX-DOAS measurements of atmospheric trace gases in Ny-Ålesund - Radiative transfer studies and their application, *Atmos. Chem. Phys.*, **4**, 955–966, doi:10.5194/acp-4-955-2004, 2004.
- Wittrock, F., *et al.*, Simultaneous global observations of glyoxal and formaldehyde from space, *Geophys. Res. Lett.*, **33**, L16804, doi:10.1029/2006GL026310, 2006.
- WMO: Annual report, Bass and Johnsten, 1975.
- WMO (World Meteorological Organisation), Scientific assessment of ozone depletion: 2006, *Global Ozone Research and Monitoring Project Report No. 50*, Geneva, Switzerland, 2007.
- Yoshida, Y., *et al.*, The impact of the 2005 Gulf hurricanes on pollution emissions as inferred from Ozone Monitoring Instrument (OMI) nitrogen dioxide, *Atmospheric Environment*, **44**(11), 1443–1448, doi:10.1016/j.atmosenv.2010.01.037, 2010.
- Zawodny, J. M. and M. P. McCormick, Stratospheric Aerosol and Gas Experiment II Measurements of the Quasi-Biennial Oscillations in Ozone and Nitrogen Dioxide, *J. Geophys. Res.*, **96**(D5), 9371–9377, doi:10.1029/91JD00517, 1991.

- Zhang, L., *et al.*, Transpacific transport of ozone pollution and the effect of recent Asian emission increases on air quality in North America: an integrated analysis using satellite, aircraft, ozonesonde, and surface observations, *Atmos. Chem. Phys.*, **8**, 6117–6136, doi:10.5194/acp-8-6117-2008, 2008.
- Zhang, Q., D. G. Streets, and K. He, Satellite observations of recent power plant construction in Inner Mongolia, China, *Geophys. Res. Lett.*, **36**, L15809, doi:10.1029/2009GL038984, 2009.
- Zhou, Y., D. Brunner, K. F. Boersma, R. Dirksen, and P. Wang, An improved tropospheric NO<sub>2</sub> retrieval for satellite observations in the vicinity of mountainous terrain, *Atmos. Meas. Tech.*, **2**, 401–416, doi:10.5194/amt-2-401-2009, 2009.
- Zhou, Y., *et al.*, Accounting for surface reflectance anisotropy in satellite retrievals of tropospheric NO<sub>2</sub>, *Atmos. Meas. Tech.*, **3**(5), 1185–1203, doi:10.5194/amt-3-1185-2010, 2010.





## Summary

### **On satellite observations of atmospheric composition and their interpretation**

Since more than 30 years satellites contribute significantly to our understanding of the composition of the atmosphere by performing global observations of atmospheric constituents from space. A recent addition to the series of Earth observing instruments is the Ozone Monitoring Instrument (OMI) that since October 2004 performs daily global measurements at high spatial resolution.

The work presented in this thesis focuses on spaceborne observations of  $\text{NO}_2$  and tropospheric aerosols, and the interpretation of the behavior of these constituents.  $\text{NO}_2$  plays an important role in the chemistry of the atmosphere due to its involvement in the catalytic destruction of ozone in the stratosphere, and by being a precursor of tropospheric ozone, linking  $\text{NO}_2$  to air quality and climate change. Aerosols also play an important role in chemistry and climate.

For the DOAS-based retrieval of  $\text{NO}_2$  from OMI measurement data an accurate characterization of the OMI spectral slitfunction is essential. The spectral slitfunction was characterized with a novel method where the slitfunction for each wavelength and viewing angle was sampled by the spectrally narrow diffraction orders of an echelle grating, with wavelength increments 10 times smaller than the spectral resolution of OMI. The resulting parameterization of the spectral slitfunction is used in the retrieval of  $\text{NO}_2$  and other DOAS-based products from OMI.

Tropospheric  $\text{NO}_2$  columns are retrieved from OMI measurements on an operational basis by the Dutch OMI  $\text{NO}_2$  (DOMINO) system. The DOMINO algorithm assimilates  $\text{NO}_2$  slant column in the TM4 chemistry transport model to estimate the stratospheric  $\text{NO}_2$  column. DOMINO data are available as a near-real time (within 3-4 hours after measurement) and as a consistent reprocessed offline dataset of collection 3, version 1.0.2. Based on the findings of validation studies involving DOMINO data, improvements to the DOMINO algorithm regarding surface albedo and a priori profile shape are identified .

An extensive validation study shows that OMI stratospheric  $\text{NO}_2$  columns are consistent within 13% with ground-based observations from the SAOZ and NDACC network. The DOMINO product performs superior to the parallel existing Standard

Product by capturing the dynamic variability of NO<sub>2</sub> in the stratosphere, such as the daytime increase of stratospheric NO<sub>2</sub> and the day-to-day variations in the NO<sub>2</sub> field associated with the collapse of the Arctic Polar vortex. Analysis of the 5+ year OMI data record shows that OMI observes variations in stratospheric NO<sub>2</sub> on a seasonal and multi-annual scale, e.g., the quasi-biennial oscillation (QBO) and trends. The NO<sub>2</sub> QBO signal exhibits a distinct interhemispheric asymmetry over the tropics, and is stronger over the Southern Hemisphere. There is good agreement between the Lauder data record and collocated OMI stratospheric NO<sub>2</sub> observations, both showing a small increase of approximately +0.5% per decade for the timespan of the OMI mission (2004-2010).

Observations from OMI and the spaceborne lidar CALIOP were used to characterize the around the world transport of an aerosol plume that was released by the intense Australian forest fires of December 2006. The plume crossed the Pacific in 5 days and completed the circumnavigation of the globe in 12 days. Estimates of the plume's altitude from the OMI cloud retrieval algorithm indicate that the plume was injected into the tropopause region by pyro-convection, triggered by the combination of a passing cold front and the latent heat of the fires. The high altitude of the plume was confirmed by CALIOP that detected the plume at 11-15 km altitude as it passed over South America. Radiative transfer calculations indicate that the underestimation of the OMI plume height in comparison with CALIOP in a later stage of the plume's transport is caused by photons scattered from lower-lying clouds that outshine the diluted plume. Simulations with TM4 agree best with OMI and CALIOP observations of the plume's transport when a passive tracer is released at approximately 10 km altitude, to mimic the effect of pyro-convective lofting which is not simulated by the model.

## List of publications

### This thesis is based on the following publications and reports:

- Dirksen, R., M. Dobber, R. Voors, and P. Levelt, Prelaunch characterization of the Ozone Monitoring Instrument transfer function in the spectral domain. *Appl. Opt.*, **45**(17), 3972–3981, doi:10.1364/AO.45.003972, 2006. **(Chapter 2)**
- Dirksen, R., H. Eskes, F. Boersma, P. Levelt, P. Veefkind, and R. van der A, *Derivation of Ozone Monitoring Instrument tropospheric NO<sub>2</sub> in near-real time (DOMINO)*. Final Report, Netherlands Agency for Aerospace Programmes, available at: <http://www.knmi.nl/~eskes/projects/domino.html>, 2008. **(Chapter 3)**
- Dirksen, R. J., K. F. Boersma, H. J. Eskes, D. V. Ionov, E. J. Bucsela, P. F. Levelt, and H. M. Kelder, Evaluation of stratospheric NO<sub>2</sub> retrieved from the Ozone Monitoring Instrument: intercomparison, diurnal cycle and trending. Submitted to *J. Geophys. Res.* **(Chapter 4)**
- Dirksen, R. J., K. F. Boersma, J. de Laat, P. Stammes, G. R. van der Werf, M. Val Martin, and H. M. Kelder, An aerosol boomerang: Rapid around-the-world transport of smoke from the December 2006 Australian forest fires observed from space. *J. Geophys. Res.*, **114**, D21201, doi:10.1029/2009JD012360, 2009. **(Chapter 5)**

### Other relevant publications involving the author:

- Boers, R., A. T. de Laat, D. C. Stein-Zweers, and R. J. Dirksen, Lifting potential of solar-heated aerosol layers. *Geophys. Res. Lett.*, **37**, L24802, doi:10.1029/2010GL045171, 2010.
- Lamsal, L. N., *et al.*, Indirect validation of tropospheric nitrogen dioxide retrieved from the OMI satellite instrument: Insight into the seasonal variation of nitrogen oxides at northern midlatitudes. *J. Geophys. Res.*, **115**, D05302, doi:10.1029/2009JD013351, 2010.

- Zhou, Y., D. Brunner, K. F. Boersma, R. Dirksen, and P. Wang, An improved tropospheric NO<sub>2</sub> retrieval for satellite observations in the vicinity of mountainous terrain. *Atmos. Meas. Tech.*, **2**, 401–416, 2009.
- Hains, J., *et al.*, Testing and improving OMI DOMINO Tropospheric NO<sub>2</sub> Using Observations from the DANDELIONS and INTEX-B Validation Campaigns. *J. Geophys. Res.*, **115**, D05301, doi:10.1029/2009JD012399, 2010.
- Volten, H., *et al.*, NO<sub>2</sub> Lidar Profile Measurements for Satellite Interpretation and Validation. *J. Geophys. Res.*, **114**, D24301, doi:10.1029/2009JD012441, 2009.
- Boersma, K. F., *et al.*, Validation of urban NO<sub>2</sub> concentrations and their diurnal and seasonal variations observed from space (SCIAMACHY and OMI sensors) using in situ measurements in Israeli cities. *Atmos. Chem. Phys.*, **9**, 3867–3879, 2009.
- Bucsela, E. J., *et al.*, Comparison of tropospheric NO<sub>2</sub> from in-situ aircraft measurements with near-real time and standard product data from OMI. *J. Geophys. Res.*, **113**, D16S31, doi:10.1029/2007JD008838, 2008.
- Dobber, M., *et al.*, Validation of Ozone Monitoring Instrument level 1b data products. *J. Geophys. Res.*, **113**, D15S06, doi:10.1029/2007JD008665, 2008.
- Boersma, K. F., *et al.*, Validation of OMI tropospheric NO<sub>2</sub> observations during INTEX-B and application to constrain NO<sub>x</sub> emissions over the eastern United States and Mexico. *Atmos. Environ.*, **42**(19), 4480–4497, doi:10.1016/j.atmosenv.2008.02.004, 2008.
- Brinksma, E. J., *et al.*, The 2005 and 2006 DANDELIONS NO<sub>2</sub> and aerosol intercomparison campaigns. *J. Geophys. Res.*, **113**, D16S46, 10.1029/2007JD008808, 2008.
- Dobber, M., R. Voors, R. Dirksen, Q. Kleipool, and P. Levelt, The high-resolution solar reference spectrum between 250 and 550 nm and its application to measurements with the ozone monitoring instrument. *Solar Phys.*, **249**, 281–291, doi:10.1007/s11207-008-9187-7, 2008.
- Dobber, M. R., *et al.*, Ozone Monitoring Instrument Calibration. *IEEE Trans. Geosci. Remote Sens.*, **44**(5), 1209–1238, 2006.
- Dobber, M., R. Dirksen, R. Voors, G. H. Mount, and P. Levelt, Ground-based zenith sky abundances and in situ gas cross sections for ozone and nitrogen dioxide with the Earth Observing System Aura Ozone Monitoring Instrument. *Appl. Opt.*, **44**(14), 2846–2856, 2005.

## Nawoord

Iets meer dan 10 jaar geleden begon ik als calibration scientist bij het OMI project. Mijn eerste werkdag viel samen met het begin van de performance test metingen aan het OMI development model, waarbij ik in hoog tempo de details van dit nieuwe, en mij nog onbekende instrument te weten kwam. In de ruim twee jaar die we bij TNO-TPD doorbrachten voor de test- en calibratiemetingen heb ik heel veel geleerd tijdens de zeer prettige en intensieve samenwerking met Marcel Dobber en Bert van den Oord. Een hoogtepunt hierbij zijn de zenith sky metingen in augustus 2002, waar we voor dag en dauw opstonden om de eerste échte metingen met OMI te verrichten.

In 2006 bood het DOMINO project de mogelijkheid om te werken met de wetenschappelijke resultaten van OMI; in het volgende wil ik een aantal mensen bedanken die een belangrijke rol hebben gespeeld bij de totstandkoming van het daaruit voortvloeiende proefschrift. Ten eerste mijn promotoren Hennie Kelder en Pieter Levelt: bedankt voor het in mij gestelde vertrouwen en voor de mogelijkheid die jullie hebben geboden om aan een uniek project als OMI te werken. Minstens zo belangrijk is de bijdrage van mijn copromotor en begeleider Folkert Boersma, vanwege zijn goede ideeën over de te volgen koers en vanwege het met veel geduld helpen bij het omzetten van een stapel onderzoeksresultaten in goed leesbare artikelen. Henk Eskes maakte mij wegwijs in de data assimilatie van het DOMINO algoritme. On the US-side I specifically want to thank Glen Jaross and George Mount for the wonderful cooperation during the OMI calibration phase. In two words: juuust great. Mijn collega's van KS/AS, CK en AK wil ik bedanken voor de vermakelijke en (on)zinnige discussies tijdens koffiepauzes, lunches en borrels.

In het leven buiten het KNMI heeft Robert Voors me laten zien dat hardlopen een stuk spannender wordt als je een kompas pakt en de gebaande paden verlaat. Onze deelname aan de legendarische OMM van 2008 zal ik nooit vergeten. Paulien wordt bedankt voor het verzorgen van het culturele programma. Verder zal ik de klimsessies met paranimf Maria en de aansluitende, wijdlopijge evaluatie waarmee het weekend ingeluid werd, missen. Mijn ouders Louis en Ria en broer(tje) Ferry dank ik voor hun hulp in de laatste fase, met name tijdens mijn transfer naar Berlijn. En tot slot natuurlijk Agnes, voor haar liefde, ondersteuning, en soms ook aansporing, om dit proefschrift af te ronden.



## Curriculum vitae

Ruud Dirksen is op 14 juli 1970 geboren in Zaandam. Een enthousiaste leraar natuurkunde van het Zaanlands Lyceum inspireerde na het behalen van het Gymnasium-B diploma in 1988 tot het volgen van de studie natuurkunde aan de Universiteit van Amsterdam. Deze werd in 1994 afgesloten met een onderzoeksstage naar het verstrooiingsgedrag van moleculaire bundels bij het FOM-instituut voor Atoom- en Molecuulfysica. Na te hebben bijgedragen aan onderzoek aan de eigenschappen van halfgeleiders aan de UvA trad Ruud Dirksen in 2000 in dienst van de Stichting Ruimteonderzoek Nederland om op het KNMI te werken aan de kalibratie van het Ozone Monitoring Instrument. Met de overstap naar het KNMI in 2006 voor het DOMINO project, begon het werk aan de wetenschappelijke interpretatie van OMI metingen, wat de basis vormt van dit proefschrift.